Advanced Topics in Science and Technology in China

Shiquan Shan · Zhijun Zhou
Yanwei Zhang

Fundamentals of Thermal Radiation for Energy Utilization in Fuel Combustion

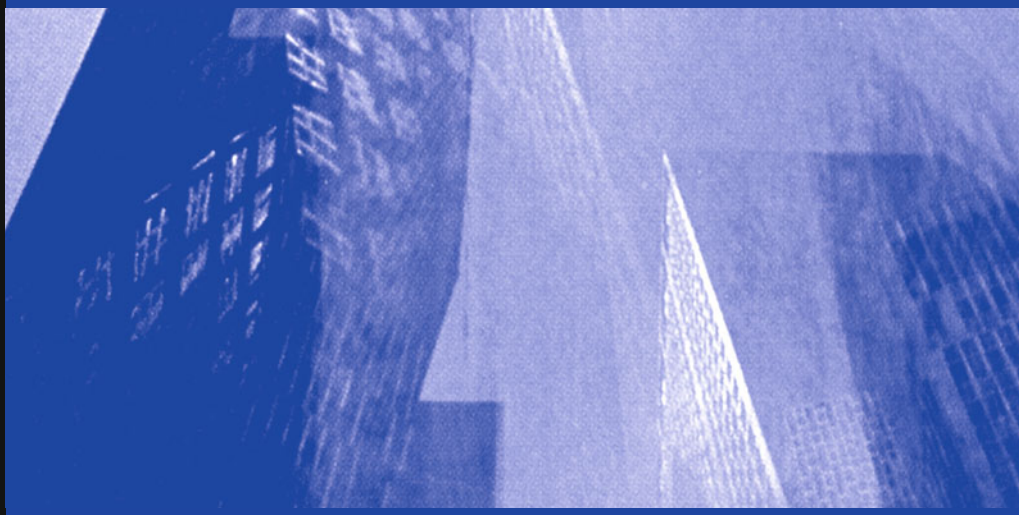

ZHEJIANG UNIVERSITY PRESS
浙江大学出版社
Springer

Advanced Topics in Science and Technology in China

Volume 67

Zhejiang University is one of the leading universities in China. In Advanced Topics in Science and Technology in China, Zhejiang University Press and Springer jointly publish monographs by Chinese scholars and professors, as well as invited authors and editors from abroad who are outstanding experts and scholars in their fields. This series will be of interest to researchers, lecturers, and graduate students alike.

Advanced Topics in Science and Technology in China aims to present the latest and most cutting-edge theories, techniques, and methodologies in various research areas in China. It covers all disciplines in the fields of natural science and technology, including but not limited to, computer science, materials science, the life sciences, engineering, environmental sciences, mathematics, and physics.

This book series is indexed by both the **Scopus** and **Compendex** databases.

If you are interested in publishing your book in the series, please contact Violetta Xu (Email: violetta_xuqian@zju.edu.cn) and Mengchu Huang (Email: mengchu.huang@cn.springer.com).

Shiquan Shan · Zhijun Zhou · Yanwei Zhang

Fundamentals of Thermal Radiation for Energy Utilization in Fuel Combustion

ZHEJIANG UNIVERSITY PRESS
浙江大学出版社

Springer

Shiquan Shan
College of Energy Engineering
Zhejiang University
Hangzhou, Zhejiang, China

Zhijun Zhou
College of Energy Engineering
Zhejiang University
Hangzhou, Zhejiang, China

Yanwei Zhang
College of Energy Engineering
Zhejiang University
Hangzhou, Zhejiang, China

ISSN 1995-6819 ISSN 1995-6827 (electronic)
Advanced Topics in Science and Technology in China
ISBN 978-981-19-8310-8 ISBN 978-981-19-8311-5 (eBook)
https://doi.org/10.1007/978-981-19-8311-5

Jointly published with Zhejiang University Press
The print edition is not for sale in China (Mainland). Customers from China (Mainland) please order the print book from: Zhejiang University Press.

This Springer imprint is published by the registered company Springer Nature Singapore Pte Ltd.
The registered company address is: 152 Beach Road, #21-01/04 Gateway East, Singapore 189721, Singapore

Preface

At present, fuel combustion is still the significant way for energy utilization. A large amount of thermal energy released in combustion is converted to electrical energy through various thermal power cycles. Electrical energy drives related devices to obtain work, heat, light, sound, and other human terminal needs. The process is a mode with direct combustion plus a simple thermal power cycle. However, the single thermal energy conversion neglects the matching of various energy qualities, resulting in low-efficiency power generation. The energy conversion process involves the energy quantity and energy-carrying form conversion. The energy-carrying forms can be photons, electrons, and phonons. For example, the radiation energy, with photons as carriers, is ignored in the traditional energy conversion. The combustion process releases photon and thermal energy simultaneously, but the energy quality differs. In high-temperature combustion, the cascade conversion of photon and thermal energy aligns with the principle of matching energy quality and potential in the energy conversion process. This matching of energy quality and potential can theoretically break through individual thermal energy conversion limitations, effectively improving energy conversion efficiency.

Based on the academic idea of the photo-thermal energy cascade conversion in fuel combustion, it is crucial to discuss the release characteristics of photo-thermal energy in combustion. Among them, photo energy refers to the radiative energy which transfers in the form of electromagnetic waves during combustion process. In heat transfer field, there is a relatively complete system on the research of thermal radiation, and many radiative characteristic models and calculation methods for radiation transfer have been proposed. However, few studies on thermodynamics and thermal radiation exist from the perspective of direct utilization of thermal radiative energy in fuel combustion. This involves the theory of energy quality for spectral radiation, as well as the transfer and prediction theory of radiative energy with different qualities under complex combustion reaction conditions. Therefore, it is an extremely valuable and interesting topic that studying thermal radiation from the perspective of energy utilization.

When I studied for my doctorate, my supervisors, Prof. Zhijun Zhou and Prof. Yanwei Zhang, provided vital inspiration on combustion thermal radiation and highlighted the significance of radiation energy use in combustion, which helped me start my scientific research career and form the academic idea of photo-thermal energy cascade conversion. In recent years, several innovative results obtained in this field have made me fortunate to receive the Outstanding Doctoral Dissertation Award of Zhejiang University and be selected for the National Postdoctoral Innovative Talent Support Program of China. Therefore, I plan to summarize our scientific research results and academic thoughts and write a monograph for academic dissemination. Thus, this book, *Fundamentals of Thermal Radiation for Energy Utilization in Fuel Combustion*, was published. This monograph focuses on the thermal radiation in fuel combustion based on the theoretical ideas of photo-thermal energy cascade conversion. The monograph introduces thermal radiation theories developed by the author's group based on radiative energy use, and a theoretical system is initially formed, providing a basis for subsequent research and inspiration for scholars in related fields.

While drafting this book, Prof. Zhang and Prof. Zhou reviewed the full text and provided valuable suggestions. Moreover, during my Ph.D. study, I was fortunate to be sponsored by the China Scholarship Council to study at the Georgia Institute of Technology with Prof. Zhuomin Zhang, an expert in thermal radiation and heat transfer, and benefited a lot. Moreover, Prof. Kefa Cen, the academician of Chinese Academy of Engineering, gives key guidance and strongly supports to this project. I would like to express my gratitude to them. The National Postdoctoral Innovative Talent Support Program of China (BX2021254) and the China Postdoctoral Science Foundation (2021M702793) primarily funded this monograph. Besides, the Ningxia Provincial Key Research and Development Program (2018BCE01004) partially funded it. Moreover, three graduate students in our group, Ms. Siqi Jia, Ms. Qiaoli Li, and Ms. Jialu Tian, translated and proofread some manuscripts. I express my gratitude to them all.

Hangzhou, China Shiquan Shan

Contents

Chapter 1
Introduction

As energy consumption increases and environmental problems worsen, efficient and clean power generation will be the critical technical foundation for resolving energy and environmental issues and achieving carbon neutrality. The theory and method of efficient energy conversion have captivated the world's attention. Scientists in thermophysics now understand that the energy conversion process includes not only the release of energy but also the change of the energy-carrying form. The energy-carrying forms can be photons, electrons, phonons, and so on. Some of the energy-carrying forms (e.g., photo/radiative energy with photons as the carrier) are ignored in the thermal conversion process based on fuel combustion. For the energy conversion process with multiple energy types, actively designing the corresponding technical route based on the principle of energy quality matching is necessary to realize the cascade and orderly utilization of energy with different qualities, and thus effectively reduce energy quality loss. The critical issue in the energy field is the scientific theory and method of energy orderly conversion considering different energy-carrying forms.

1.1 Photo-Thermal Energy Cascade Conversion for Fuel Combustion

The primary way humans use energy is through the generation of thermal energy through fuel combustion. Through high-temperature fuel combustion, a large amount of thermal energy is released, which is then used to generate electric energy through various thermal power cycles. However, the energy production process based on the thermal power cycle does not consider energy quality matching, and the energy released by fuel combustion is only utilized in the form of thermal energy. However, the highest parameters of the thermal power cycle limit the system's energy conversion efficiency.

S. Shan et al., *Fundamentals of Thermal Radiation for Energy Utilization in Fuel Combustion*, Advanced Topics in Science and Technology in China 67,
https://doi.org/10.1007/978-981-19-8311-5_1

During the combustion process, the chemical energy in the fuel is converted into photo energy and thermal energy. The term *photo energy* refers to both visible and invisible light (e.g., ultraviolet and infrared) [1], i.e., radiative energy. The heat energy mentioned here primarily refers to non-radiative heat energy transferred during the combustion process. From a thermodynamic standpoint, the energy released by combustion is not limited to having both a quantitative and qualitative character. Combustion produces both photo and thermal energy, but their qualities differ. Additionally, photo energy has spectral characteristics, and spectral radiation with different wavelengths has different energy quality. Short-wavelength radiation has high energy quality and can directly excite the photovoltaic conversion device. Thus, carrying out cascade and orderly conversion of photo-thermal energy of various qualities is necessary: the high-grade radiative energy from high-temperature combustion should be converted step-by-step into electrical energy following the frequency, and the low-grade thermal energy should be further utilized through thermal power generation to establish a new photo-thermal energy cascade conversion system (Fig. 1.1), which will greatly improve energy conversion efficiency compared with traditional thermal power cycle [2, 3].

Flame radiation results from high-temperature combustion, and high-temperature energy has higher quality. Thus, the technical route of cascade conversion of photo-thermal energy conforms to thermodynamic principles and is an innovative idea to overcome the limitation of the efficiency of single thermal power conversion. Melino et al. [4, 5] used the radiative energy generated by the high combustion temperature to power photovoltaic conversion, and the remaining thermal energy in flue gas is used to power the Organic Rankine Cycle. Filters can also control and shape the

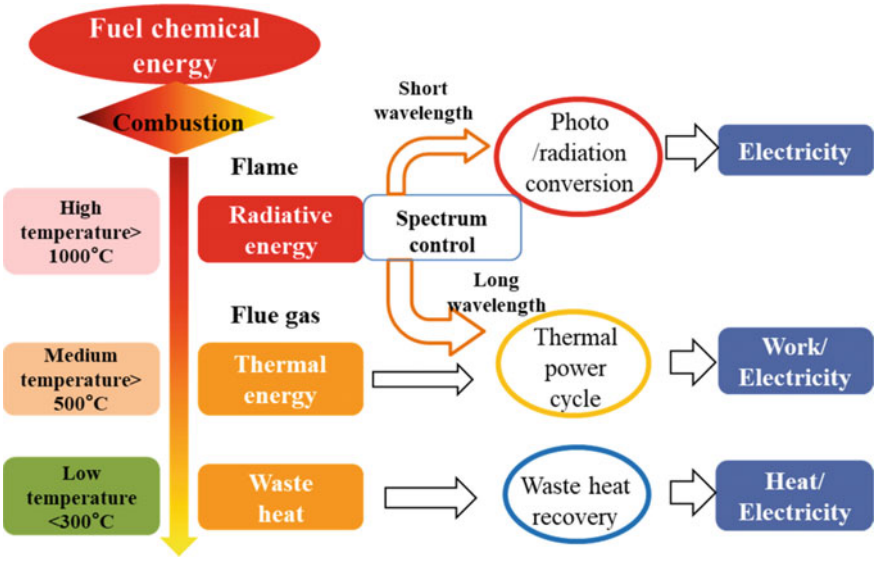

Fig. 1.1 Schematic diagram of photo-thermal cascade conversion of fuel combustion

flame radiation spectrum, and the optimized photo-electric conversion efficiency can reach >50% [6], which is higher than that of the conventional thermal power cycle. Thus, the performance potential of photo-thermal energy cascade conversion system outperforms that of the single thermal power conversion system. Furthermore, the author's group proposed an innovative integrated system concept based on oxy-fuel combustion between a thermophotovoltaic device and a Brayton-Rankine combined cycle [2], claiming that the system can improve efficiency by about 20% compared with the thermal power cycle with similar parameters. Based on this, a photo-thermal cascade conversion system [3] that directly utilizes the spectral radiative energy of fuel combustion is proposed, and the theoretical superiority of the system is demonstrated. This system's schematic diagram is shown in Fig. 1.2.

Pure oxygen is mixed with a certain proportion of recycled flue gas (CO_2-based) and fed into the furnace chamber as a combustion-supporting atmosphere in oxyfuel combustion technology. As a CO_2 control technology in combustion progress, this technology is strategically important for achieving the goal of carbon neutrality [7]. It should be noted that oxyfuel combustion can achieve much higher temperatures

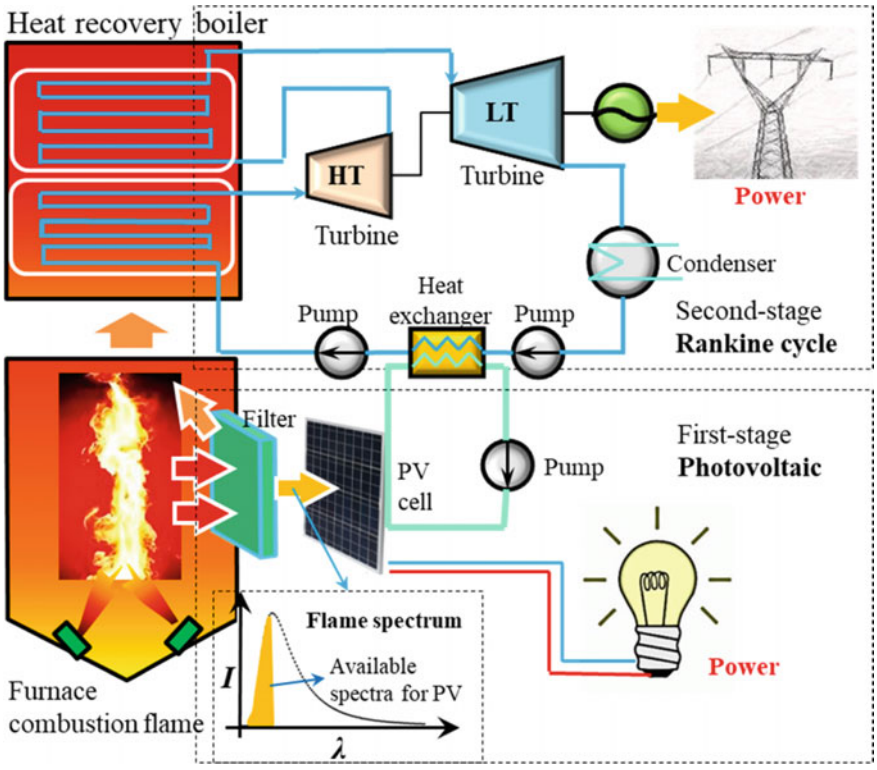

Fig. 1.2 The photo-thermal cascade conversion system that directly utilizes the spectral radiative energy of combustion flame [3]. Reprinted from Shan et al. [3], Copyright (2019), with permission from John Wiley and Sons

than conventional air combustion under the conditions of increased oxygen concentration or even directly using pure oxygen [8]. If the thermal power cycle will be continued to be directly used for electricity generation in high-temperature oxy-fuel combustion, the high energy quality will be wasted due to the thermal power cycle's maximum parameters. Furthermore, the high-temperature of oxy-fuel combustion generates a significant amount of radiative energy. Thus, a photo-thermal energy cascade conversion system based on oxy-fuel combustion can be built by prioritizing radiative energy cascade conversion, followed by thermal power cycle conversion. It not only controls CO_2 emissions in fuel combustion, in line with the strategic goal of carbon neutrality, but it also effectively matches energy quality and potential, theoretically improving energy conversion efficiency.

Given the preceding concept and the prevalence of energy conversion through fuel combustion, the development of combustion thermal radiation theory based on the background of photo-thermal energy cascade utilization is not only important for guiding the combustion-based photo-thermal energy cascade conversion system but can also enrich the theoretical system of thermal radiation. These primarily include the radiative energy quality theory, an efficient radiation calculation model for complex combustion conditions, and the mechanism of radiative energy release and distribution in the combustion process. Section 1.2 will go over these in greater detail.

1.2 Key Issues of Combustion Thermal Radiation for Energy Utilization

1.2.1 Theory of Radiation Energy Quality Theory for Fuel Combustion

Radiative energy in fuel combustion has spectral characteristics, and spectral radiation with different wavelengths have different energy qualities. To use radiative energy more efficiently, analyzing its quality from the standpoint of thermodynamics is necessary, thus quantitatively evaluating the value of radiative energy and guiding the cascade conversion of high-temperature radiative energy. Exergy is used in thermodynamics to describe the quality of energy, which refers to the usable part, also known as available energy. When compared with energy analysis, exergy analysis can describe not only the quantity but also the quality of energy. Consequently, the analysis of thermal radiation processes using the second law of thermodynamics is of unique significance. On the one hand, radiation is the primary heat transfer mode in high-temperature equipment, and second law analysis of radiation aids in investigating the entropy production and exergy loss of high-temperature combustion equipment, allowing the high-temperature energy conversion system to be evaluated and optimized more rationally. The second law, on the other hand, can be used to accurately analyze exergy in radiation transfer process within different wavebands,

which further guides energy management with different energy grades to achieve efficient exergy conversion.

Radiation, as an electromagnetic wave, has wavelength and frequency. Moreover, as a way of heat transfer, it has entropy and exergy properties similar to thermal energy. Radiative energy has its distinct characteristics, which distinguishes it from thermal energy. Wright [9] identified the difference between the entropy of radiation heat transfer and the entropy of heat conduction processes. Liu and Chu [10] investigated the expression of entropy production of the heat transfer process and discovered that the conventional formula of entropy production rate for heat conduction is ineffective for radiative heat transfer.

The blackbody radiation exergy theory proposed by Petela at the University of Silesia in Poland in his early years [11], Spanner's theory based on solar radiation research [12], and the Carnot efficiency theory proposed by Jeter of Georgia Institute of Technology [13] are representative views for the exergy of blackbody radiation. The theoretical core of the three is the coefficient of radiation exergy-to-exergy ratio, which is summarized in Table 1.1. Bejan [14] proposed some thought-provoking discussions on all three, which will be introduced and discussed in depth in Chap. 2 of this book. Currently, scholars generally accept Petela's blackbody radiation exergy formula. Candau [15] also proposed a derivation of the intensity of spectral radiation exergy based on Planck's formula for entropy intensity of monochromatic radiation and the concept of radiation temperature for spectral radiation exergy. Based on the concept of equivalent temperature, Chen et al. [16] proposed a corresponding calculation formula for monochromatic photon exergy. These studies ignored the distinction between radiative and thermal energy.

Lior [17] previously reviewed the exergy calculation in the radiation transfer process, but the radiative exergy problem was rarely considered in early studies. Caldas and Semiao [18] were the first to consider entropy production in radiative transfer calculations and they separately analyzed entropy production by emission, absorption, and scattering processes in the media radiative transfer. Liu and Chu [19] investigated the radiative exergy transfer in the media on this basis. These studies' models are compatible with a standard method for solving radiative transfer equations. Based on these hypotheses, Zhang et al. [20, 21] investigated various entropy generations, including thermal radiation in conditions (e.g., mixed flue gas and hydrocarbon fuel combustion) and discovered that soot has a greater effect on radiative

Table 1.1 Comparison of various blackbody radiation exergy theories

Researcher	Year	Formula of radiation exergy-to-energy ratio	Evaluation
Petela [11]	1964	$\eta = 1 - \frac{4}{3}\frac{T_0}{T} + \frac{1}{3}\left(\frac{T_0}{T}\right)^4$	Output useful work with radiative energy as input
Spanner [12]	1964	$\eta = 1 - \frac{4}{3}\frac{T_0}{T}$	Output absolute work with radiative energy as input
Jeter [13]	1981	$\eta = 1 - \frac{T_0}{T}$	Using Carnot heat engine efficiency

entropy generation. These studies used the radiation temperature concept [22] and expressed the spectral radiative entropy using a formula similar to the Carnot thermal efficiency, which is intended for calculating the entropy generation of the radiation heat transfer. In fact, the exergy of thermal energy in the form of Carnot's law is not suitable for characterizing radiative entropy and exergy, and the radiation temperature is a relatively macroscopic concept that is not used to directly characterize the quality of monochromatic radiation energy. Thus, the monochromatic spectral radiation itself must be considered to better characterize the monochromatic radiation exergy.

1.2.2 Thermal Radiation Model of Non-gray Gas Medium in Combustion

Large amounts of high-temperature triatomic gases were noted in the combustion process, and accurate prediction of their non-gray radiative properties is important for scientific research. The radiation properties and radiative heat transfer of the media are critical scientific issues because of the higher proportion of triatomic gases (e.g., CO_2 and H_2O) in an oxy-fuel combustion atmosphere. Experiments were used to determine radiation parameters (e.g., emissivity and absorptivity of gas media in the early year) and then the emissivity tables of H_2O and CO_2 were summarized based on the experimental data. The heat transfer field introduced the theory of atoms and molecules to study gas radiation after the middle of the twentieth century due to the development of aerospace technology. Simultaneously, the line by line method (LBL) and the spectral band model method appeared, based on the atmospheric radiation research methods. Subsequent developments have resulted in global models as illustrated in Fig. 1.3.

The LBL method uses quantum mechanical principles and formulas to establish the relationship between gas spectral parameters and gas absorption coefficients, emissivity, and so on. The LBL method is the most accurate non-gray radiation model in principle but it requires the use of a gas spectral database. The LBL method has the disadvantage of being too computationally intensive to be used in actual computational fluid dynamics (CFD) simulations, thus it is frequently used as a benchmark to verify the accuracy of other models. The HITRAN [23] and HITEMP databases are the most widely used spectral databases; the most recent HITEMP database contains millions of *hotlines* [24]. Its maximum application temperature is up to 3000 K, making it suitable for thermal radiation calculations in high-temperature engineering.

The waveband model divides the spectrum into a series of wide or narrow band intervals and uses the average absorption coefficient within each band to calculate the overall spectrum absorption coefficient. Waveband models are classified as narrowband and wideband models (the wavenumber interval of the narrowband

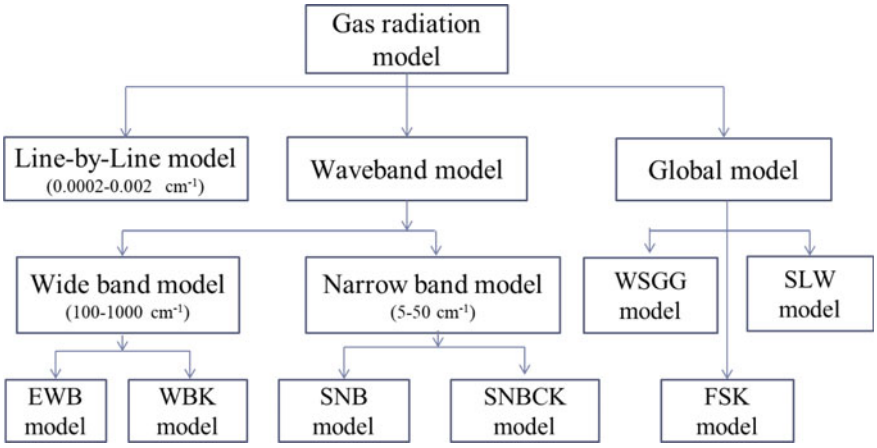

Fig. 1.3 Classification of gas non-gray radiation models

model is typically 5–50 cm^{-1}), with the typical narrow band models being a statistical narrowband model (SNB) [25] and statistical narrowband correlated-*k* model (SNBCK) [26]. Although the SNB model is computationally intensive, results from the SNB model based on the EM2C Lab database are very similar to those of the accurate LBL model based on the HITEMP2010 database, and thus it can be used as a benchmark [27]. In general, the wideband model interval is 100–1000 cm^{-1}. The most common are the exponential wideband (EWB) model [28], the wideband *k*-distribution (WBK) model [29], and so on.

The global model is primarily concerned with radiative heat flux, with less emphasis placed on spectrum characteristics. The global model can significantly reduce calculation time while also meeting the accuracy requirements for engineering calculations, making it suitable for CFD calculations. Typical global models include the full spectrum *k*-distribution (FSK) model [30], the weighted-sum-of-gray-gases (WSGG) model [31], and the spectral line-based WSGG model (SLW) [32]. The basic idea behind the WSGG model is to substitute several gray gases for the actual non-gray gas. This method's principle is simple and its calculation efficiency is very high; it can be combined with various radiation transfer equation solution methods, giving it a wide range of adaptability. After considering calculation time and accuracy, the WSGG model is the best gas radiation model for current combustion calculation and research [33].

Smith et al. [31] developed a set of WSGG model parameters based on the SNB model for air–fuel combustion conditions. However, the flue gases in oxy-fuel combustion contain a high concentration of triatomic gases (e.g., CO_2) which have different radiation properties than air–fuel combustion. Thus, the traditional WSGG model applied to air–fuel combustion is inapplicable to oxy-fuel combustion [34]. In recent years, researchers have developed various WSGG models for oxy-fuel combustion conditions. Based on the EWB model, Khare [35] established

WSGG model parameters for oxy-fuel conditions and discovered that the gas emissivity in oxy-fuel conditions is underestimated when using the traditional WSGG model parameters in [31]. Yin [36] developed a new WSGG model using the EWB model as a benchmark. Additionally, Johansson et al. [37] developed a new WSGG model using the SNB model of the EM2C database as a benchmark. Later, Kangwanpongpan et al. [38], Dorigon et al. [39], and Bordbar et al. [40], presented their respective models based on the more accurate HITEMP2010 database. The models presented above were all designed for oxy-fuel combustion at atmospheric pressures. Future studies should focus on developing WSGG models for gas radiation that covers a wider range of pressures, temperatures, and atmospheres for complex reaction conditions (e.g., pressurized oxy-fuel combustion and combustion in aero engines).

1.2.3 Radiative Energy Characteristics of High-Temperature Oxy-Fuel Combustion

Because of the special temperature and atmospheric conditions in oxy-fuel combustion with high-temperature, the radiation energy contained in the combustion process is greater than that in the air–fuel combustion, making it suitable for the effective utilization of the radiation energy in combustion. Consequently, scholars have conducted extensive studies on the radiation properties of oxy-fuel combustion flames, which is also significant for the effective utilization of radiation energy in oxy-fuel combustion.

To consider the radiation heat transfer characteristics of oxy-fuel combustion [41], a 1.2-MW pilot plant is being built in IHI of Japan to study the oxy-fuel combustion of pulverized coal. The experiment was conducted in O_2/CO_2 and air atmospheres with high-volatile bituminous coal. Heat exchange tubes were installed in the furnace's radiative area to simulate the real heat exchange equipment in the furnace, and the absorption energy of heat exchange tubes was measured as flame radiation heat transfer. According to the findings, oxy-fuel combustion with 27%O_2/CO_2 atmosphere under wet flue gas recycling has similar radiation heat transfer characteristics to air–fuel combustion. Thus, they proposed that the oxygen concentration in the actual oxy-fuel combustion boiler be controlled to ensure similar radiation heat transfer characteristics as conventional combustion. Furthermore, Andersson et al. investigated the flame characteristics of propane combustion in an O_2/CO_2 atmosphere, building a 100-kW oxy-fuel combustion test rig with flue gas recycling at Chalmers University of Technology, Sweden [42, 43]. The results show that the combustion temperature is similar to that of air–fuel combustion under 27% O_2/CO_2, but the flame radiation intensity is increased. The emissivity of flame at 21% and 27% oxygen concentrations differs from that of air–fuel combustion, and the radiation intensity of flame at 27% oxygen concentration increases by ~30%. Ash radiation

is believed to contribute more to the O_2/CO_2 atmosphere than the known contribution of elevated partial pressure of CO_2. The presence of CO_2 not only increases gas radiation but also has a significant impact on the formation of soot and its flame radiation. Following that, Andersson et al. [44] continued to investigate the radiation characteristics of oxy-fuel combustion flame of lignite on this furnace, discovering that the flame temperature and total radiation intensity will increase as the oxygen proportion in the atmosphere increases from 25 to 29%. When oxy-fuel combustion is used instead of air–fuel combustion, the ratio of gas radiation to total radiation increases slightly. Thus, the authors concluded that the majority of the radiation in lignite flames is emitted by flame particles. In recent years, researchers have developed numerical cases to simulate the physical field in a furnace using the radiation transfer equation. Gronarz et al. [45] investigated the coupling relationship between gas radiation and particle radiation in an oxy-fuel combustion boiler for pulverized coal. The findings show that particle emissivity had a significant impact on radiation intensity. Adams et al. [46] established a two-dimensional furnace case for pulverized coal combustion and calculated the influence of pressure on the radiative heat flux of oxy-fuel combustion. The findings indicate that increasing pressure within 10 atm can increase radiative heat flux.

The preceding studies contribute to a better understanding of the radiation characteristics of fuel combustion. The results show that oxy-fuel combustion can effectively improve the proportion of radiation energy in combustion, and the radiative heat flux can be effectively managed by adjusting the combustion parameters, which is conducive to efficient radiation energy utilization. The majority of current studies focus on the effects of fuel type and oxygen concentration on the radiative heat transfer properties of oxy-fuel combustion. The spectral radiation characteristics in combustion processes and their influence mechanism are important issues to investigate in the future in terms of radiation energy utilization.

1.3 Objective and Organization of This Book

The goal of this book is to present, for the first time, academic thoughts on photothermal energy cascade conversion of fuel combustion. Based on this, with a focus on thermal radiation in fuel combustion, this book will primarily introduce a series of thermal radiation theories for radiative energy utilization on recent studies of the authors' group, forming an initial theory system. This serves as the foundation for future studies while also inspiring scholars in related fields with academic thought and scientific theory.

The following key scientific problems on combustion thermal radiation must be solved to achieve the goal of efficient and scientific utilization of high-temperature combustion energy. (1) No reasonable method exists to evaluate radiation energy quality, particularly the energy quality theory of monochromatic radiation for fuel combustion, so expanding the radiation thermodynamics theory is critical. (2) A lack of an efficient model suitable for a wide parameter range was noted in the calculation

of gas radiation characteristics under complex combustion conditions, particularly under pressurized combustion conditions. (3) Currently, few studies were noted on combustion radiation from the standpoint of energy utilization, particularly for oxy-fuel combustion conditions. This book presents the study findings of authors' group on the aforementioned key problems. Figure 1.4 depicts the relationship of the main contents of this book. The fundamentals of thermal radiation for energy utilization in fuel combustion are divided into three sections: Thermodynamic theory of spectral radiation for combustion (Chap. 2), Gas radiation model under complex combustion conditions (Chap. 3), and Radiative energy characteristics of fuel combustion (Chaps. 4 and 5).

Chapter 2 introduces the spectral radiation thermodynamic theory for combustion. Based on summarizing and evaluating existing radiation thermodynamics theories, a radiation engine model is developed to analyze the blackbody radiative exergy based on the belief that radiative energy and thermal energy are different. Furthermore, a novel infinite-staged Carnot heat engine model based on the concept of radiation equivalent temperature is established, and an integral expression of monochromatic radiative exergy is proposed. In addition, the integral expression of monochromatic radiative entropy is provided. It serves as a theoretical foundation for the subsequent analysis of combustion radiation characteristics in terms of energy utilization.

Chapter 3 introduces the gas radiation model under complex combustion conditions. The method for the development of the WSGG model is summarized in detail based on the introduction of non-gray gas radiation models (e.g., SNB and WSGG

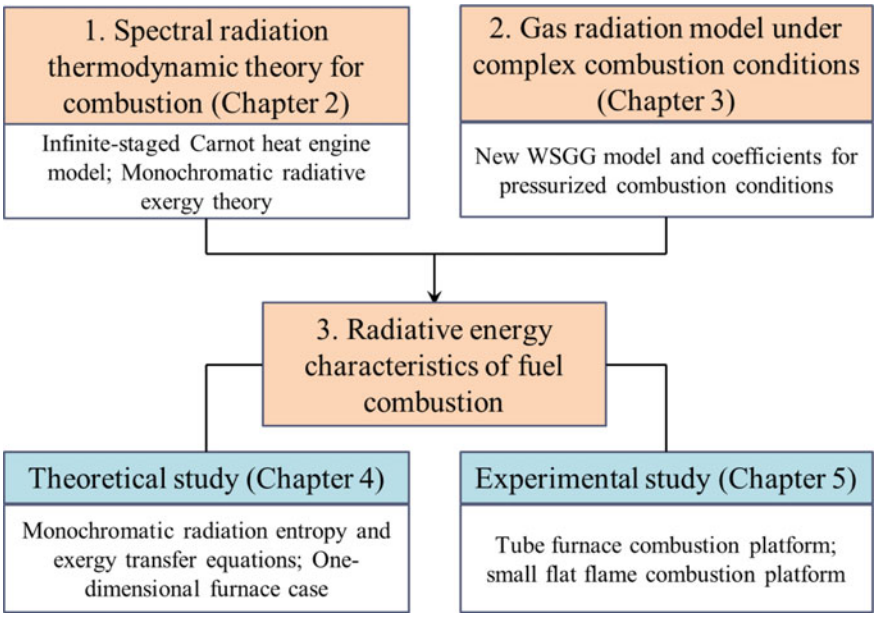

Fig. 1.4 The relationship diagram of the main chapters of this book

models), and the WSGG model structure is improved to make it compatible with parameters in a wider pressure range. Furthermore, based on the benchmark of the SNB model in the EM2C laboratory, a new WSGG model and coefficients for complex combustion conditions are developed. The new WSGG model and coefficients can produce accurate and efficient calculation results.

Chapter 4 discusses the calculation method and characteristics of radiation exergy in participating medium of fuel combustion. Firstly, the theory of monochromatic radiation exergy proposed in Chap. 2 is combined with the radiation transfer equation, establishing the monochromatic radiation entropy and radiation exergy transfer equations and verifying the calculation method based on the second law of thermodynamics. Following that, a one-dimensional furnace case is simulated to calculate the spectral radiation energy characteristics of the participating medium in fuel combustion, providing a foundation for numerical calculation of combustion radiation for energy utilization.

Chapter 5 is the radiation energy characteristics of solid fuel combustion. Based on the experimental platforms of the tubular furnace and the small flat-flame burner, it introduces the radiation energy characteristics of oxy-fuel combustion with various solid fuels, including pulverized coal and semi-coke. The effect of reaction conditions on the radiation energy and spectral properties is investigated. Furthermore, the radiation exergy and its spectral properties are investigated using the radiation thermodynamics theory proposed in Chap. 2. The findings are useful in understanding and controlling radiative energy in fuel combustion.

References

1. Modest MF (2013) Radiative heat transfer. Academic Press
2. Shan S, Zhou Z, Cen K (2019) An innovative integrated system concept between oxy-fuel thermo-photovoltaic device and a Brayton-Rankine combined cycle and its preliminary thermodynamic analysis. Energy Convers Manage 180:1139–1152
3. Shan S, Zhou Z, Wang Z et al (2020) A novel flame energy grading conversion system: preliminary experiment and thermodynamic parametric analysis. Int J Energy Res 44(3):2084–2099
4. De Pascale A, Ferrari C, Melino F et al (2012) Integration between a thermophotovoltaic generator and an organic Rankine cycle. Appl Energy 97:695–703
5. Barbieri E, De Pascale A, Ferrari C et al (2012) Performance evaluation of the integration between a thermo-photo-voltaic generator and an organic Rankine cycle. J Eng Gas Turbines Power 134(10):102301
6. Burger T, Sempere C, Roy-Layinde B et al (2020) Present efficiencies and future opportunities in thermophotovoltaics. Joule 4(8):1660–1680
7. Chen L, Yong SZ, Ghoniem AF (2012) Oxy-fuel combustion of pulverized coal: characterization, fundamentals, stabilization and CFD modeling. Prog Energy Combust Sci 38(2):156–214
8. Fu Z, Zhang S, Li X et al (2015) MSW oxy-enriched incineration technology applied in China: combustion temperature, flue gas loss and economic considerations. Waste Manage 38:149–156
9. Wright S (2007) Comparative analysis of the entropy of radiative heat transfer and heat conduction. Int J Thermodyn 10(1):27–35
10. Liu LH, Chu SX (2006) On the entropy generation formula of radiation heat transfer processes. J Heat Transfer 128(5):504–506

11. Petela R (1964) Exergy of heat radiation. J Heat Transfer 86(2):187–192
12. Spanner DC (1964) Introduction to thermodynamics. Academic Press
13. Jeter SM (1981) Maximum conversion efficiency for the utilization of direct solar radiation. Sol Energy 26(3):231–236
14. Bejan A (1987) Unification of three different theories concerning the ideal conversion of enclosed radiation. J Sol Energy Eng 109(1):46–51
15. Candau Y (2003) On the exergy of radiation. Sol Energy 75(3):241–247
16. Chen Z, Mo S (2007) Effective temperature and exergy of monochromic blackbody radiation. Progr Nat Sci-Mater Int 17(10):1250–1254
17. Lior N, Sarmiento-Darkin W, Al-Sharqawi HS (2006) The exergy fields in transport processes: their calculation and use. Energy 31(5):553–578
18. Caldas M, Semiao V (2005) Entropy generation through radiative transfer in participating media: analysis and numerical computation. J Quant Spectrosc Radiat Transfer 96(3–4):423–437
19. Liu LH, Chu SX (2007) Radiative exergy transfer equation. J Thermophys Heat Transfer 21(4):819–822
20. Zhang Z, Lou C, Li Z et al (2020) Evaluation of radiative entropy generation in a high temperature system including H_2O, CO_2 and soot with non-gray wall. J Quant Spectrosc Radiat Transfer 253:107175
21. Zhang Z, Lou C, Long Y et al (2021) Thermodynamics second-law analysis of hydrocarbon diffusion flames: effects of soot and temperature. Combust Flame 234:111618
22. Bejan A (2016) Advanced engineering thermodynamics. Wiley, Hoboken
23. Rothman LS, Gordon IE, Babikov Y et al (2013) The HITRAN2012 molecular spectroscopic database. J Quant Spectrosc Radiat Transfer 130:4–50
24. Rothman LS, Gordon IE, Barber RJ et al (2010) HITEMP, the high-temperature molecular spectroscopic database. J Quant Spectrosc Radiat Transfer 111(15):2139–2150
25. Malkmus W (1967) Random Lorentz band model with exponential-tailed S^{-1} line-intensity distribution function. JOSA 57(3):323–329
26. Liu F, Smallwood G, Gulder O (1999) Radiation heat transfer calculations using the SNBCK method. In: 33rd Thermophysics Conference, p 3679
27. Chu H, Gu M, Consalvi JL et al (2016) Effects of total pressure on non-gray gas radiation transfer in oxy-fuel combustion using the LBL, SNB, SNBCK, WSGG, and FSCK methods. J Quant Spectrosc Radiat Transfer 172:24–35
28. Edwards DK (1976) Molecular gas band radiation. Adv Heat Transfer 12:115–193
29. Marin O, Buckius RO (1997) Wide band correlated-k approach to thermal radiative transport in nonhomogeneous media. J Heat Transfer 119(4):719–729
30. Modest MF, Zhang H (2002) The full-spectrum correlated-k distribution for thermal radiation from molecular gas-particulate mixtures. J Heat Transfer 124(1):30–38
31. Smith TF, Shen ZF, Friedman JN (1982) Evaluation of coefficients for the weighted sum of gray gases model. J Heat Transfer 104(4):602–608
32. Denison MK, Webb BW (1993) A spectral line-based weighted-sum-of-gray-gases model for arbitrary RTE solvers 115(4):1004–1012
33. Becher V, Goanta A, Spliethoff H (2012) Validation of spectral gas radiation models under oxyfuel conditions–Part C: validation of simplified models. Int J Greenhouse Gas Control 11:34–51
34. Gupta R, Khare S, Wall T et al (2006) Adaptation of gas emissivity models for CFD based radiative transfer in large air-fired and oxy-fired furnaces. In: Proceedings of the 31st International Technical Conference on Coal Utilization & Fuel Systems, pp 21–26
35. Khare S (2008) Heat transfer in air-fired pulverized fuel furnaces retrofitted to oxy-fuel coal. University of Newcastle (Thesis)
36. Yin C, Johansen LCR, Rosendahl LA et al (2010) New weighted sum of gray gases model applicable to computational fluid dynamics (CFD) modeling of oxy-fuel combustion: derivation, validation, and implementation. Energy Fuels 24(12):6275–6282

37. Johansson R, Leckner B, Andersson K et al (2011) Account for variations in the H_2O to CO_2 molar ratio when modeling gaseous radiative heat transfer with the weighted-sum-of-gray-gases model. Combust Flame 158(5):893–901
38. Kangwanpongpan T, França FHR, da Silva RC et al (2012) New correlations for the weighted sum of gray-gases model in oxy-fuel conditions based on HITEMP 2010 database. Int J Heat Mass Transf 55(25–26):7419–7433
39. Dorigon LJ, Duciak G, Brittes R et al (2013) WSGG correlations based on HITEMP2010 for computation of thermal radiation in non-isothermal, non-homogeneous H_2O/CO_2 mixtures. Int J Heat Mass Transf 64:863–873
40. Bordbar MH, Węcel G, Hyppänen T (2014) A line by line based weighted sum of gray gases model for inhomogeneous CO_2–H_2O mixture in oxy-fired combustion. Combust Flame 161(9):2435–2445
41. Nozaki T, Takano S, Kiga T et al (1997) Analysis of the flame formed during oxidation of pulverized coal by an O_2-CO_2 mixture. Energy 22(2–3):199–205
42. Andersson K, Johnsson F (2007) Flame and radiation characteristics of gas-fired O_2/CO_2 combustion. Fuel 86(5–6):656–668
43. Andersson K, Johansson R, Johnsson F et al (2008) Radiation intensity of propane-fired oxy-fuel flames: implications for soot formation. Energy Fuels 22(3):1535–1541
44. Andersson K, Johansson R, Hjärtstam S et al (2008) Radiation intensity of lignite-fired oxy-fuel flames. Exp Thermal Fluid Sci 33(1):67–76
45. Gronarz T, Schulze J, Laemmerhold M et al (2017) Quantification of the influence of parameters determining radiative heat transfer in an oxy-fuel operated boiler. Fuel Process Technol 157:76–89
46. Adams BR, Hosler TR (2019) Pressure and particle property impacts on radiation in oxy-coal combustion. Fuel 239:667–676

Chapter 2
Spectral Radiation Thermodynamic Theory for Combustion

Radiative thermodynamic theory is very important in high-temperature engineering. In this chapter, several expressions of blackbody radiation exergy are first discussed before developing a radiation engine model based on the idea that radiative energy and thermal energy are different. This model is also used to validate Petela's formula. Second, a novel infinite-staged Carnot heat engine model has been developed based on the concept of radiation equivalent temperature as well as a monochromatic photon exergy expression suitable for engineering applications. Finally, monochromatic photon entropy is discussed using the infinite-staged Carnot heat engine model and provides an integral photon entropy expression. The monochromatic radiative entropy and exergy proposed satisfy the thermodynamic relation and can reflect the differences between radiative energy and thermal energy. The thermodynamic theory of monochromatic radiation introduced in this chapter serves as a theoretical foundation for the analysis of the radiative characteristics of fuel combustion in subsequent chapters.

2.1 Exergy of Blackbody Radiation

2.1.1 Several Representative Views

Most researchers concentrate on blackbody radiation because it is the foundation of thermal radiation. However, differing viewpoints were noted on the exergy of blackbody radiation. Thus, some representative viewpoints are presented.

Revised from Zhou et al. Exergy of Blackbody Radiation and Monochromatic Photon, International Journal of Thermophysics, Copyright (2017), with permission from Springer Nature.

S. Shan et al., *Fundamentals of Thermal Radiation for Energy Utilization in Fuel Combustion*, Advanced Topics in Science and Technology in China 67,
https://doi.org/10.1007/978-981-19-8311-5_2

Petela [1] proposed the following formula for blackbody radiation exergy at temperature T in 1964

$$b_{\mathrm{BR}} = \sigma\left(T^4 - \frac{4}{3}T_0T^3 + \frac{1}{3}T_0^4\right)\left[\frac{\mathrm{W}}{\mathrm{m}^2}\right] \tag{2.1}$$

where T_0 is the ambient temperature. Moreover, radiative exergy can be calculated via multiplying energy by the radiative exergy coefficient, which is defined as the ratio of exergy to energy. The blackbody radiation intensity of is σT^4 and the corresponding radiative exergy coefficient can be expressed as

$$\eta_{\mathrm{P}} = 1 - \frac{4}{3}\frac{T_0}{T} + \frac{1}{3}\left(\frac{T_0}{T}\right)^4 \tag{2.2}$$

This is called Petela's formula. According to Jeter [2], the radiative exergy coefficient is equal to the Carnot efficiency as shown in Eq. (2.3). Some researchers have also recognized this [3, 4].

$$\eta_{\mathrm{J}} = 1 - \frac{T_0}{T} \tag{2.3}$$

Spanner proposes a radiation exergy coefficient based on the study of solar radiation [5]

$$\eta_{\mathrm{S}} = 1 - \frac{4}{3}\frac{T_0}{T} \tag{2.4}$$

Petela's study on radiation exergy is earlier and more persistent. Although each formula is supported by some scholars, Eq. (2.1) is the most widely used formula, and many researchers have amended or expanded on it [6–11].

2.1.2 Discussion on the Reversibility

In this section, the differences and relationships among the three radiation exergy formulas are analyzed. At the same radiation temperature T and ambient temperature T_0 ($T > T_0$), $\eta_{\mathrm{S}} < \eta_{\mathrm{P}} < \eta_{\mathrm{J}}$ can be observed. The Carnot efficiency is the highest reversible conversion efficiency for thermal energy. Thus, Jeter's formula appears to be reasonable if radiation is regarded as thermal energy. Furthermore, some scholars believe that the reason why $\eta_{\mathrm{P}} < \eta_{\mathrm{J}}$ is because Petela's model for calculating η_{P} is irreversible. Bejan [12], for example, proposed a special model in 1987 that includes three reversible processes: first, photon gas at temperature T_1 fulfills the space volume V_1; second, it is connected with a reversible Carnot engine and outputs work to the outside at temperature T_2; and third, the photon gas is exhausted and the volume

of space becomes 0. The radiation exergy coefficient is η_S if the first process is irreversible, η_P if both the first and third processes are irreversible, and η_J if all three processes are reversible. Bejan's point of view demonstrates that these three formulas are valid under different conditions and do not contradict one another. This is a very clever discussion. However, it is believed that radiative energy is not, in fact, thermal energy, and Petela's research also shows that the radiation process is irreversible in and of itself. Thus, different perspectives exist on the reversibility of the radiation exergy model.

It is also investigated the reversibility in the deducing of Petela's theory; this problem can be illustrated using Wright's work [13]. A delicate radiation model combined with Carnot engine is constructed to demonstrate that the reversible conversion can be achieved for blackbody radiation (Fig. 2.1). At temperature T, the blackbody cavity maintains thermal equilibrium. Besides, there is an ideal section for heat conduction absorbing blackbody radiation, which is then converted into thermal energy dQ for work production through Carnot engine (ambient temperature is T_0). Consequently, the blackbody temperature decreases to T_0 at last. It is believed that the entropy generation is negligible in the derivation and the thermal equilibrium is kept for the black cavity if dQ is regarded to be infinitesimal. Consequently, it can be regarded as a quasistatic process, and its physical meaning is the maximum work which can be harvested from thermal radiation. The quasi-equilibrium process is regarded as reversible because no entropy growth was noted throughout the process. The maximum useful work that radiation can convert is

$$W = \int_{T}^{T_0} \left(1 - \frac{T_0}{T}\right) dQ \tag{2.5}$$

Through substituting the blackbody radiation energy formula: $U = aT^4V$ [14] into Eq. (2.5), Eq. (2.2) can be deduced. This shows that the derivation process of Petela's formula is theoretically reversible.

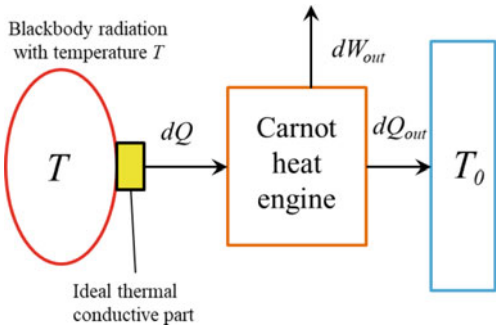

Fig. 2.1 Model to discuss the reversibility of the radiation conversion process

2.1.3 Differences Among the Three Formulas

The differences between the formulas of Petela and Spanner are investigated in [15], pointing out that Spanner the absolute work, instead of useful work, is regarded as exergy in Spanner's formula. According to energy conservation law, after absorbing the energy Q from the outside, the initial internal energy of the medium increases from U_1 to U_2 and performs the absolute work $W_{1\text{–}2}$. Furthermore, the absolute work $W_{1\text{–}2}$ includes two parts, which are useful work W_u, as well as the work W_e spent for the *compression of the environment*, where $W_e = p_0\ (V_1 - V_0)$. Exergy means the useful energy, thus, it makes sense that and using useful work as radiative exergy. Thus, when the exergy is represented by useful work W_u, Petela's theory is deduced. In solar energy engineering, since the radiation temperature is as high as 5800 K, the calculation results from Spanner's theory and Petela's theory are very similar.

Figure 2.2 is plotted to discuss Jeter's formula, which is expressed as Carnot efficiency. Moreover, Fig. 2.2a showed that the radiation from a blackbody at a high temperature of T is directly absorbed by an ideal Carnot engine. This radiation could do the most work with Carnot efficiency. Nevertheless, thermal energy should be the input of Carnot engine rather than radiative energy. Otherwise, the process of radiation will be overlooked and will not be able to obtain the exact radiative exergy. Thus, it is necessary to set a receiver to convert radiative energy into thermal energy, and then, the Carnot engine could convert thermal energy into work as shown in Fig. 2.2b. Here the temperature of thermal energy T' is always less that the temperature of blackbody T; otherwise, there is no radiation heat transfer. The Carnot engine absorbs thermal energy to output work, and its efficiency η_b is $1 - T_0/T'$, with $1 - T_0/T' < 1 - T_0/T$. This implies that the Carnot efficiency should be greater than the radiative exergy coefficient. Furthermore, the radiative exergy should be calculated based on the quasi-equilibrium process as shown in Fig. 2.1, and the result conforms to Petela's theory, which is less than the efficiency deduced by Carnot engine. Consequently, Jeter's theory implies that radiation enters the Carnot engine directly, this is the difference between Petela's theory and Jeter's theory. Thus, it's more rational to represent the exergy of blackbody radiation through Petela's formula.

2.1.4 Radiation Engine Model for Discussing the Exergy of Blackbody Radiation

In this section, a radiation engine model, similar to the Carnot heat engine model, is presented to discuss the exergy formula of blackbody radiation. The nature of the radiation could thus be better explained. The radiation engine, as shown in Fig. 2.3, is an ideal black box converter; the input energy is the blackbody radiative energy flow R_{in}, with temperature T and entropy S_{in}. The output energy is the blackbody radiative energy flow R_{out}, with temperature T_0 and entropy S_{out}; it is balanced with the ambient conditions. The radiation engine's entire process produces work W,

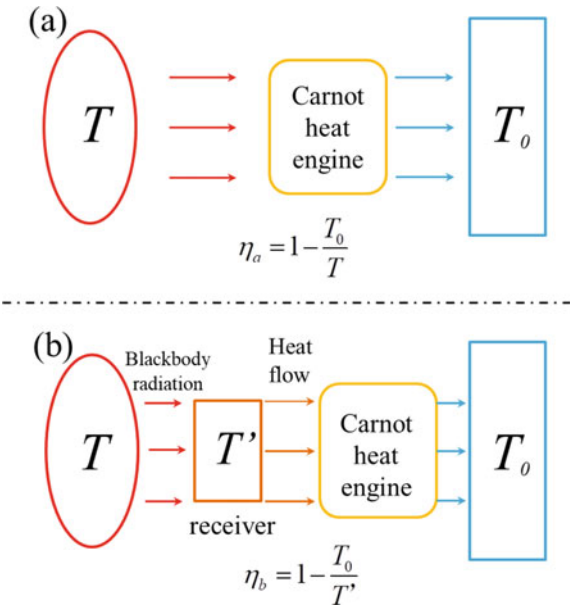

Fig. 2.2 The schematic diagram of radiation producing work by the Carnot heat engine. **a** Radiation directly comes into the heat engine; **b** radiation converts into heat energy and then comes into the heat engine

which is the maximum amount of work. The heat conduction with the environment is Q, and its entropy is S.

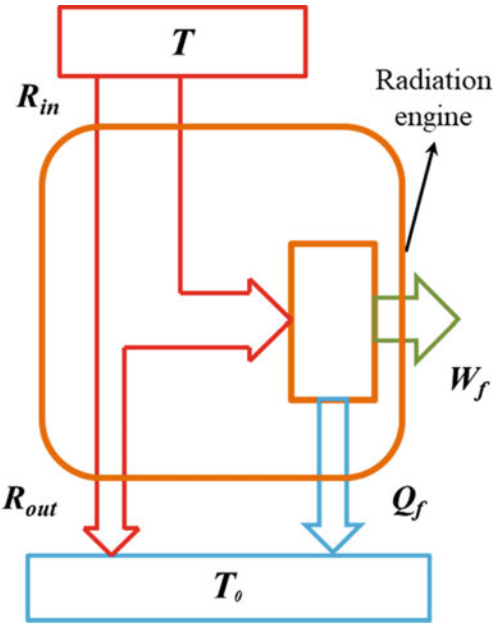

Fig. 2.3 The radiation engine model

The entropy of blackbody radiation is $4/3\sigma T^3$ following the thermodynamics [16]. Furthermore, Wright [17] discussed radiation entropy in detail, stating that radiation entropy should be expressed as nQ/T; for blackbody radiation, $n = 4/3$. Thus, the entropy of blackbody radiation flow can be expressed as $4/3\sigma T^3$.

The energy balance equation can be expressed using the first law of thermodynamics as follows

$$R_{\text{in}} = R_{\text{out}} + Q + W \tag{2.6}$$

The entropy balance equation can be expressed using the second law of thermodynamics as follows

$$S_{\text{in}} = S_{\text{out}} + S + \Delta S. \tag{2.7}$$

where ΔS is the entropy production; for a reversible process with the highest conversion efficiency, $\Delta S = 0$. The input energy flow is expressed as $R_{\text{in}} = \sigma T^4$, the outlet energy flow is expressed as $R_{\text{out}} = \sigma T_0^4$, the inlet entropy flow is expressed as $S_{\text{in}} = 4/3\sigma T^3$, the outlet entropy is expressed as $S_{\text{out}} = 4/3\sigma T_0^3$, and the entropy flow of heat conduction with the environment is expressed as $S = Q/T_0$. The formula below is obtained when the expression for entropy is substituted into Eq. (2.7)

$$Q = (S_{\text{in}} - S_{\text{out}})T_0 = \frac{4}{3}\sigma\left(T^3 - T_0^3\right)T_0 \tag{2.8}$$

The formula below is obtained by substituting Eq. (2.8) and the expressions for energy flow into Eq. (2.6)

$$\begin{aligned} W &= R_{\text{in}} - R_{\text{out}} - (S_{\text{in}} - S_{\text{out}})T_0 \\ &= \sigma\left(T^4 - T_0^4\right) - \frac{4}{3}\sigma\left(T^3 - T_0^3\right)T_0 \\ &= \sigma T^4 - \frac{4}{3}\sigma T^3 T_0 + \frac{1}{3}\sigma T_0^4 \end{aligned} \tag{2.9}$$

Thus, the exergy coefficient is:

$$\eta = \frac{W}{R_{\text{in}}} = \sigma T^4 - \frac{4}{3}\sigma T^3 T_0 + \frac{1}{3}\sigma T_0^4 \Big/ \sigma T^4 = 1 - \frac{4}{3}\frac{T_0}{T} + \frac{1}{3}\left(\frac{T_0}{T}\right)^4 \tag{2.10}$$

This is the coefficient from Petela's exergy formula. When compared to thermal energy, the entropy of radiation can be expressed as Q/T. Furthermore, the inlet and outlet entropy flow is $S_{\text{in}} = \sigma T^3$ and $S_{\text{out}} = \sigma T_0^3$, respectively. Then, it is substituted into (2.9) and obtain

$$W = R_{\text{in}} - R_{\text{out}} - (S_{\text{in}} - S_{\text{out}})T_0$$

$$= \sigma\left(T^4 - T_0^4\right) - \sigma\left(T^3 - T_0^3\right)T_0$$
$$= \sigma T^4 - \sigma T^3 T_0 \tag{2.11}$$

Thus, the coefficient of exergy is

$$\eta = \frac{W}{R_{\text{in}}} = \frac{\sigma T^4 - \sigma T^3 T_0}{\sigma T^4} = 1 - \frac{T_0}{T} \tag{2.12}$$

Equation (2.12) represents exactly the Carnot efficiency proposed by Jeter; thus, the reason why the coefficient of Petela's exergy formula is less than the Carnot efficiency is not the irreversibility of the radiation system but the difference between radiation and heat. The distinction implies that the entropy-to-energy ratios of radiation and heat conduction differ. In the case of reversible conversion of radiation energy conversion, the radiation engine should be left in the form of blackbody radiation at the ambient temperature. This is consistent with Wright's [17] viewpoint.

In addition to using classical thermodynamic theory to analyze the radiation exergy, Badescu [18] demonstrated Petela's formula using the quantum method of statistical thermodynamic theory. Additionally, Markvart and Bauer [19] discussed the exergy of photovoltaics and obtained Petela's formula when they calculated the exergy over the entire wavelength range. All of the preceding discussions and analyses indicate that Petela's formula essentially clarifies the differences between radiative energy and thermal energy. Moreover, it can accurately represent radiative exergy and is widely accepted by scholars.

2.2 Exergy of Monochromatic Radiation

2.2.1 Discussion of the Exergy of Monochromatic Photons

Blackbody radiation is the typical radiation model; therefore, it is very meaningful to study blackbody radiation. However, non-blackbody radiation is more prevalent in the engineering fields of fuel combustion and solar energy, which is still under investigation. Monochromatic radiation must be first investigated to study non-blackbody radiation. Studying the properties of monochromatic photons is the premise of studying non-blackbody radiation because monochromatic radiation is essentially the integration of monochromatic photons.

Much more attention paid to photosynthesis has fueled studies into the exergy of monochromatic photons. According to the second law of thermodynamics, the exergy of organics produced during photosynthesis must come from the exergy of photons absorbed by chlorophyll. Thus, researchers have proposed formulas for calculating the exergy of monochromatic photons [20, 21]

$$u = hv\left(1 - \frac{T_0}{T_\mathrm{r}}\right) \tag{2.13}$$

The corresponding coefficient of exergy to energy is

$$\eta_\mathrm{u} = 1 - \frac{T_0}{T_\mathrm{r}} \tag{2.14}$$

This formula is analogous to the Carnot efficiency. Scholars generally believe that T_0 is the ambient temperature. However, statements about T_r differ, with some believing that it is the surface temperature of radiation, i.e., the surface temperature of the sun for a photosynthesis system [22, 23] and others believing that T_r should be in a specific temperature range [24]. Furthermore, Meszena [25], Chen [26], and other scholars believe that T_r should be an equivalent temperature $T_{(\upsilon)}$, which has the dimension of temperature and can be used to express energy quality. The authors of the current book agree more with this view.

However, as this book emphasizes, radiative energy differs from thermal energy and the Carnot efficiency is not suitable for the exergy calculation of radiation in the macroscopic field. Thus, an exergy-to-energy ratio similar to the Carnot efficiency may not be reasonable for the exergy calculation of monochromatic photons. Scholars studying photon radiation exergy for many years have largely ignored this issue. Furthermore, we propose an infinite-staged Carnot engine model based on the concept of equivalent temperature to investigate the exergy of monochromatic photons in greater depth.

For a bundle of monochromatic light with fixed frequency υ, the energy of each photon is $h\upsilon$ and its equivalent temperature is $T_{(\upsilon)}$. An absorption model is established as shown in Fig. 2.4; it can absorb the energy $h\upsilon$ of radiation photons and the absorption model then emits a radiation photon with frequency υ' and energy $h\upsilon'$; simultaneously, thermal energy hdv is generated. Furthermore, thermal energy hdv performs work via the Carnot heat engine at equivalent temperature $T_{(\upsilon)}$. Moreover, dv is assumed to be infinitely small, and this model will not output work after infinite procedures until the frequency reaches a certain value υ_0 and has an equivalent temperature $T_{(\upsilon 0)}$ corresponding to the ambient temperature T_0. The output work can represent the exergy of monochromatic radiation photons because the entire infinite-staged Carnot engine model is a non-dissipative reversible process.

The exergy of a photon can be expressed through all of the infinite-staged Carnot engine model processes as

$$W_u = \int_{\upsilon_0}^{\upsilon} h\left(1 - \frac{T_0}{T_{(\upsilon)}}\right) dv \tag{2.15}$$

Because photons are essentially electromagnetic radiation rather than ordinary thermal energy, the maximum useful work of a photon should be expressed in integral form rather than simply as $h\upsilon$ multiplied by the Carnot efficiency after the equivalent

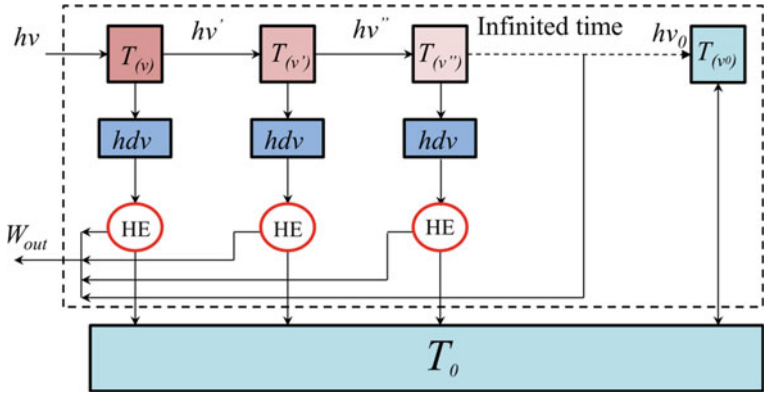

Fig. 2.4 The infinite-staged Carnot engine model

temperature is introduced. Thus, only the quasi-equilibrium process, as discussed above, can reflect changes in energy quality during the energy conversion process.

Concerning the specific expression on Eq. (2.15), the relationship between the equivalent temperature $T_{(\nu)}$ and the frequency ν or wavelength λ must be considered. Because wavelength λ is mostly used as a variable in the spectral study, wavelength λ was chosen to represent their relationship. As is known, only a portion of visible light and ultraviolet radiation with shorter wavelengths can be converted into electrical energy during photoelectric conversion, whereas the majority of infrared radiation cannot. Additionally, frequency attenuation is noted in the radiation transfer process. Clearly, high frequency radiation with a short wavelength has higher energy quality and higher equivalent temperature $T_{(\lambda)}$. Petela [27] investigated the exergy spectrum of blackbody and gray-body surface radiation and discovered that, at similar radiation temperature, the exergy-to-energy coefficient η_{u} will be greater and the equivalent temperature $T_{(\lambda)}$ will also be higher if the wavelength λ of monochromatic radiation is shorter or the frequency ν is higher. Furthermore, Meszena et al. [25] believe that a photon's state is related to radiation temperature; thus, the equivalent temperature is also correlated with radiation temperature. In addition, Petela's study [27] also demonstrated that different exergy-to-energy coefficients of monochromatic radiation exist at different radiation temperatures; the higher the radiation temperature is, the higher the exergy-to-energy coefficient of monochromatic radiation will be. This implies that the equivalent temperature $T_{(\lambda)}$ of monochromatic radiation will be higher as the radiation temperature T increases.

Therefore, we can conclude that the equivalent temperature $T_{(\lambda)}$ of a monochromatic radiation photon is inversely proportional to its wavelength λ and proportional to the radiation temperature T. An approximation is provided for the equivalent temperature $T_{(\lambda)}$

$$T_{(\lambda)}^{k} = \frac{f T^{m}}{\lambda^{n}} \tag{2.16a}$$

If the equivalent temperature is expressed in terms of frequency v, then $T_{(v)}$ can be written as

$$T_{(v)}^{k} = \frac{fT^{m}}{c^{n}} v^{n} \tag{2.16b}$$

where, f is a constant.

2.2.2 *Discussion About the Formula of Equivalent Temperature*

In this section, the accuracy of the equivalent temperature formula Eq. (2.16) is observed and the values of constants m, n, k, and f are discussed. It can be deduced from Eq. (2.16) that

$$T_{(v)} = \frac{f^{1/k} T^{m/k}}{c^{n/k}} v^{n/k} \tag{2.17}$$

$$\frac{T_0}{T_{(v)}} = \frac{T_{(v_0)}}{T_{(v)}} = \left(\frac{v_0}{v}\right)^{\frac{n}{k}} \tag{2.18}$$

Substituting Eq. (2.18) into (2.15) obtains

$$W_u = hv - \frac{k}{k-n} hv^{\frac{k-n}{k}} v_0^{\frac{n}{k}} + \frac{n}{k-n} hv_0. \tag{2.19}$$

The corresponding coefficient of exergy-to-energy η_{u} is W_{u}/hv:

$$\begin{aligned} \eta_{\mathrm{u}} &= 1 - \frac{k}{k-n}\left(\frac{v_0}{v}\right)^{n/k} + \frac{n}{k-n}\frac{v_0}{v} = 1 - \frac{k}{k-n}\left(\frac{\lambda}{\lambda_0}\right)^{n/k} + \frac{n}{k-n}\frac{\lambda}{\lambda_0} \\ &= 1 - \frac{k}{k-n}\frac{T_0}{T_{(\lambda)}} + \frac{n}{k-n}\left(\frac{T_0}{T_{(\lambda)}}\right)^{k} \end{aligned} \tag{2.20}$$

Petela's formula, as mentioned in Sect. 2.1, accurately represents the exergy of the blackbody radiation. Considering the link between the macroscopic and microscopic fields, if the blackbody monochromatic emission intensity is multiplied by the coefficient of exergy-to-energy η_{u} as in Eq. (2.20) and then integrated over the entire wavelength, it should equal to the exergy of blackbody radiation, as represented by Petela's formula.

This is Planck's [28] proposed monochromatic emission intensity of blackbody radiation:

$$i_{b,\lambda} = \frac{c_1 \lambda^{-5}}{e^{(c_2/\lambda T)} - 1} \tag{2.21}$$

where $c_1 = 2\pi h c_0^2 = 3.74 \times 10^{-16}\,\mathrm{W\,m^2}$, $c_2 = hc_0/k = 1.4388 \times 10^{-2}\,\mathrm{m\,K}$, c_1 denotes the first Planck constant, and c_2 denotes the second Planck constant. Thus, the following relationship exists

$$\int_0^\infty i_{b,\lambda}\left[1 - \frac{k}{k-n}\frac{T_0}{T_{(\lambda)}} + \frac{n}{k-n}\left(\frac{T_0}{T_{(\lambda)}}\right)^k\right]d\lambda = \sigma T^4\left[1 - \frac{4}{3}\frac{T_0}{T} + \frac{1}{3}\left(\frac{T_0}{T}\right)^4\right] \tag{2.22}$$

Equation (2.22) can be used to calculate equivalent temperature, and the left side of Eq. (2.22) can be written as

$$\begin{aligned}
&\int_0^\infty i_{b,\lambda}\left[1 - \frac{k}{k-n}\frac{T_0}{T_{(\lambda)}} + \frac{n}{k-n}\left(\frac{T_0}{T_{(\lambda)}}\right)^k\right]d\lambda \\
&= \int_0^\infty \frac{c_1\lambda^{-5}}{e^{c_2/\lambda T} - 1}\left[1 - \frac{k}{k-n}\frac{T_0}{T_{(\lambda)}} + \frac{n}{k-n}\left(\frac{T_0}{T_{(\lambda)}}\right)^k\right]d\lambda \\
&= \sigma T^4 - \frac{k}{k-n}\frac{c_1 T_0}{f^{n/k} T^{m/k}}\int_0^\infty \frac{\lambda^{-5+n/k}}{e^{c_2/\lambda T} - 1}d\lambda + \frac{n}{k-n}\frac{c_1 T_0^k}{f T^m}\int_0^\infty \frac{\lambda^{-5+n}}{e^{c_2/\lambda T} - 1}d\lambda
\end{aligned} \tag{2.23}$$

Set $x = c_2/\lambda T$; then, $dx = -\frac{c_2}{\lambda^2 T}d\lambda$. Thus,

$$\begin{aligned}
&\frac{k}{k-n}\frac{c_1 T_0}{f^{n/k} T^{m/k}}\int_0^\infty \frac{\lambda^{-5+n/k}}{e^{c_2/\lambda T} - 1}d\lambda \\
&= -\frac{k}{k-n}\frac{c_1 T_0 T^{4-n/k-m/k}}{f^{n/k} c_2^{4-n/k}}\int_\infty^0 \frac{x^{3-n/k}}{e^x - 1}dx = \frac{k}{k-n}\frac{c_1 T_0 T^{4-n/k-m/k}}{f^{n/k} c_2^{4-n/k}}\int_0^\infty \frac{x^{3-n/k}}{e^x - 1}dx
\end{aligned} \tag{2.24}$$

and

$$\frac{n}{k-n}\frac{c_1 T_0^k}{f T^m}\int_0^\infty \frac{\lambda^{-5+n}}{e^{c_2/\lambda T} - 1}d\lambda$$

$$= -\frac{n}{k-n}\frac{c_1 T_0^k T^{4-n-m}}{f c_2^{4-n}} \int_{\infty}^{0} \frac{x^{3-n}}{e^x - 1} dx = \frac{n}{k-n}\frac{c_1 T_0^k T^{4-n-m}}{f c_2^{4-n}} \int_{0}^{\infty} \frac{x^{3-n}}{e^x - 1} dx \quad (2.25)$$

Make $a = \int_0^\infty \frac{x^{3-n/k}}{e^x-1} dx$; $b = \int_0^\infty \frac{x^{3-n}}{e^x-1} dx$.
Thus, Eq. (2.22) can be expressed as

$$\sigma T^4 - \frac{k}{k-n}\frac{c_1 a}{f^{n/k} c_2^{4-n/k}} T_0 T^{4-n/k-m/k} + \frac{n}{k-n}\frac{c_1 b}{f c_2^{4-n}} T_0^k T^{4-n-m}$$
$$= \sigma T^4 - \frac{4}{3}\sigma T_0 T^3 + \frac{1}{3}\sigma T_0^4 \quad (2.26)$$

According to the theory of dimensional analysis, $\left[T_0 T^3\right] = \left[T_0 T^{4-n/k-m/k}\right]$ and $\left[T_0^4\right] = \left[T_0^k T^{4-n-m}\right]$ exist. Thus, $k = 4$, $m = 3$, and $n = 1$ can be deduced; Eq. (2.16) can be written as:

$$T_{(\lambda)}^4 = \frac{f T^3}{\lambda} \quad (2.27)$$

From Eq. (2.20), the corresponding coefficient of exergy to energy η_u can be obtained

$$\eta_u = 1 - \frac{4}{3}\frac{T_0}{T_{(\lambda)}} + \frac{1}{3}\left(\frac{T_0}{T_{(\lambda)}}\right)^4 \quad (2.28)$$

Using the relationship in Eq. (2.16), an exergy-to-energy coefficient η_u of monochromatic photons that is similar to Petela's coefficient η_p can be obtained. Furthermore, Eq. (2.26) can be written as

$$\sigma T^4 - \frac{4}{3}\frac{c_1 a}{f^{1/4} c_2^{15/4}} T_0 T^3 + \frac{1}{3}\frac{c_1 b}{f c_2^3} T_0^4 = \sigma T^4 - \frac{4}{3}\sigma T_0 T^3 + \frac{1}{3}\sigma T_0^4 \quad (2.29)$$

where σ is the Stefan–Boltzmann constant and $a = \int_0^\infty \frac{x^{11/4}}{e^x-1} dx$; $b = \int_0^\infty \frac{x^2}{e^x-1} dx$. Using MATLAB software to calculate the integral, $a = 4.8732$ and $b = 2.4041$ can be obtained.

Then, Eq. (2.29) is discussed under various conditions. When $T > T_0$, the third term in Eq. (2.29) accounts for a small proportion, and thus the value of exergy is determined by the second term, i.e., the second term is primarily considered and $c_1 a = f^{1/4} c_2^{15/4} \sigma$; the calculated result is $f = 4.5638 \times 10^{-3}$ m K.

When $T > T_0$, the formula can be expressed as $4.5638 \times 10^{-3} T^3 = \lambda T_{(\lambda)}^4$, and an error ε_1 will be noted after the introduction of Eq. (2.16) for the exergy calculation of blackbody radiation.

$$\varepsilon_1 = \frac{\frac{1}{3}\left(c_1 b / f c_2^3 - \sigma\right) T_0}{\sigma T^4 - \frac{4}{3}\sigma T_0 T^3 + \frac{1}{3}\sigma T_0^4} = \frac{0.16}{3\left(T / T_0\right)^4 - 4\left(T / T_0\right)^3 + 1} \tag{2.30}$$

When $T < T_0$, the second term accounts for a small proportion of the total, and thus, the value of exergy is determined by the third term, i.e., the third term is primarily considered and $c_1 b = f c_2^3 \sigma$; and the calculated result is $f = 5.33 \times 10^{-3}$ m K.

In this case, when $T < T_0$, the formula can be expressed as $5.33 \times 10^{-3} T^3 = \lambda T_{(\lambda)}^4$, and an error ε_2 will be noted after the introduction of Eq. (2.16) for the exergy calculation of blackbody radiation.

$$\varepsilon_2 = \frac{\frac{4}{3}\left(\frac{c_1 a}{f^{1/4} c_2^{15/4}} - \sigma\right) T_0 T^3}{\sigma T^4 - \frac{4}{3}\sigma T_0 T^3 + \frac{1}{3}\sigma T_0^4} = \frac{0.24}{3\left(T / T_0\right) + \left(T_0 / T\right)^3 - 4} \tag{2.31}$$

The ambient temperature T_0 is set at 300 K. The errors ε_1 and ε_2 are calculated at various temperatures. The results show that the error introduced by the formula is very small in the case of high or low temperatures. Furthermore, under common industrial radiation conditions, with a temperature of ~1000 K, the error is <0.1%; for a solar radiation temperature of ~5800 K, the error is $<10^{-8}$ and thus negligible. The equivalent temperature formula applies to both industrial and solar radiation.

The expression form of the equivalent temperature in Eq. (2.16) in this book is approximate. However, the integral form of Eq. (2.15) for radiation photon exergy is still accurate. Furthermore, the preceding analysis shows that the monochromatic photon exergy of blackbody radiation calculated using the equivalent temperature expression is applicable in most situations, particularly in high-temperature engineering. Furthermore, the exergy-to-energy coefficient of monochromatic photons calculated using the equivalent temperature expression is similar to Petela's coefficient. Thus, it is simple, easy to remember, and can be used to calculate non-blackbody radiation in most engineering fields.

Equivalent temperature $T_{(\lambda)}$ can represent the energy quality of monochromatic radiation photons. Additionally, the higher the value of $T_{(\lambda)}$, the better the energy quality. Thus, the exergy of monochromatic photons can be calculated using equivalent temperature. The exergy produced by converting monochromatic radiation into electricity, mechanical energy, or other forms of energy is no greater than the exergy of monochromatic radiation.

2.2.3 *Discussion About Radiation from the Combustion Flame*

Fuel combustion can generate a high temperature of about 2000 K, and for oxy-fuel combustion conditions, it can generate a high temperature of more than 2500 K. Based on the formula of equivalent temperature Eq. (2.27), Fig. 2.5 shows the

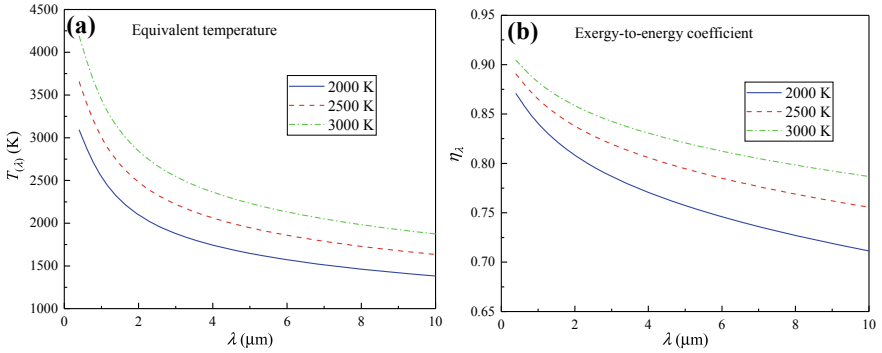

Fig. 2.5 The monochromatic radiation equivalent temperature $T_{(\lambda)}$ and exergy-to-energy coefficient η_u versus the wavelength λ at combustion radiation temperatures

monochromatic radiation equivalent temperature $T_{(\lambda)}$ and exergy-to-energy coefficient η_u versus the wavelength λ at combustion radiation temperatures of 2000 K, 2500 K, and 3000 K respectively. It can be seen that as the wavelength decreases or the frequency increases, there is a significant increase in monochromatic radiation equivalent temperature. The equivalent temperature at 3000 K radiation temperature is significantly higher, indicating that the oxy-fuel combustion conditions can effectively improve the equivalent temperature. The visible light band, which consumes a large proportion of the energy in fuel combustion, not only has a high monochromatic radiation equivalent temperature $T_{(\lambda)}$ but also a high exergy-to-energy coefficient η_u of >85%. Thus, the use of visible light and near-infrared radiation has significant value. Frequency division should be the most logical way to use combustion radiation.

2.3 Entropy of Spectral Radiation

The study of photon entropy in monochromatic radiation has been going on for a long time. Planck [29] gave statistical average photon entropy in an equilibrium state with fixed frequency ν and specific blackbody radiation temperature T. Furthermore, Ito [30] believed that the entropy of a monochromatic photon is $h\nu/T$ for the photon emitted from a radiation source with temperature T and frequency ν. All of this indicates that the entropy of monochromatic radiation is related to radiation temperature T and the frequency of the photon ν. On the other hand, Kirwan [31] investigated the inherent entropy of a single photon using the second law of thermodynamics, Planck's equation, and the Gibbs–Duhem equation and discovered that photon entropy is constant regardless of wavelength. Furthermore, Chen [26] believed that the entropy of a monochromatic photon is $h\nu/T_{(\nu)}$ based on the concept of equivalent temperature $T_{(\nu)}$. Additionally, a conclusion that photon entropy is a

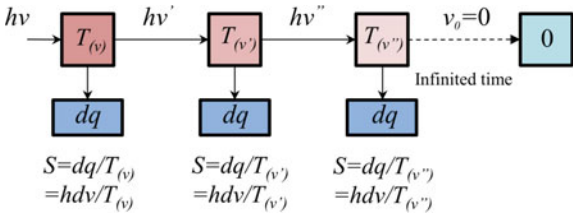

Fig. 2.6 The infinite-staged Carnot heat engine used to analyze the entropy of a photon

constant was obtained based on the relationship between equivalent temperature and photon frequency in this book. Most scholars, however, find it difficult to accept the notion that photon entropy is a constant. It is perhaps doubtful that an independent photon is directly given the macroscopic parameter temperature T, as Kirwan's paper suggests. Due to the difference between radiative energy and thermal energy, it is also questionable whether the entropy expression analogous to the $Q/T_{(v)}$ form is given directly using equivalent temperature $T_{(v)}$. Thus, the infinite-staged Carnot engine model proposed in this chapter is used to analyze the entropy of a photon.

The infinite-staged Carnot heat engine is used to analyze the entropy of a photon as shown in Fig. 2.6. A monochromatic photon has the energy hv and the equivalent temperature $T_{(v)}$. The absorbing model absorbs a photon, converting a small portion of the energy converted into thermal energy dq and emitting the remainder as radiation with a slightly lower frequency v'; thus, its energy is hv'. The entropy of the thermal energy transformed from radiation can be expressed in the form $Q/T_{(v)}$; thus, $dq/T_{(v)} = hdv/T_{(v)}$. All of the photon's radiation energy is converted into thermal energy through infinite processes like this until the frequency reaches zero. Because each step of the process is reversible and generates no entropy, the entropy of a photon with frequency v should be expressed as the sum of thermal energy entropy in each process.

The expression of monochromatic photon entropy should be

$$s_v = \int_0^v \frac{h}{T_{(v)}} dv \tag{2.32}$$

After the introduction of equivalent temperature $T_{(v)}$, the expression of monochromatic photon entropy should be an integral form rather than the simple form $hv/T_{(v)}$. In essence, this photon entropy with integral form denotes differences between radiative energy and thermal energy.

If the relationship proposed in the current paper between the equivalent temperature $T_{(v)}$ and radiation frequency v, i.e., Eq. (2.27), is substituted into Eq. (2.32), the following relation can be obtained

$$s_v = \frac{hc^{1/4}}{f^{1/4}T^{3/4}} v^{\frac{3}{4}} \tag{2.33}$$

where c is the speed of light and f is the coefficient in the equivalent temperature equation. Equation (2.33) should also be approximated because the relationship between radiation equivalent temperature and frequency in Eq. (2.27) is approximated in this chapter. However, nothing is wrong with qualitative analysis. As a result of this analysis, the entropy of a monochromatic photon can be concluded to be proportional to its frequency ν and radiation temperature T.

Moreover, after substituting the Eq. (2.32) into the formula for the relationship between exergy and entropy, the expression for monochromatic photon exergy can be obtained

$$\begin{aligned} W_{\mathrm{u}} &= H - H_0 - T_0(S - S_0) = h\upsilon - h\upsilon_0 - T_0\left(s_\upsilon - s_{\upsilon_0}\right) \\ &= h\int_{\upsilon_0}^{\upsilon} d\upsilon - T_0\left(\int_0^{\upsilon} \frac{h}{T_{(\upsilon)}}d\upsilon - \int_0^{\upsilon_0} \frac{h}{T_{(\upsilon)}}d\upsilon\right) \\ &= h\int_{\upsilon_0}^{\upsilon} d\upsilon - T_0\int_{\upsilon_0}^{\upsilon} \frac{h}{T_{(\upsilon)}}d\upsilon = \int_{\upsilon_0}^{\upsilon} h\left(1 - \frac{T_0}{T_{(\upsilon)}}\right)d\upsilon \end{aligned} \tag{2.34}$$

This is just the exergy expression in Eq. (2.15), and it also indicates that the exergy and entropy of monochromatic radiation photons proposed in this chapter are intrinsically harmonious.

2.4 Summary

Distinctions exist between radiative energy and thermal energy, and the mechanism of radiation heat transfer differs from that of heat conduction or convection. Thus, radiative energy cannot be considered synonymous with thermal energy. In several views of blackbody radiation exergy, Petela's formula is reversible in derivation and distinguishes the differences between radiative energy and thermal energy when compared to the Carnot efficiency formula proposed by Jeter. Therefore, Petela's formula accurately represents radiation exergy.

Based on the concept of monochromatic photon equivalent temperature $T_{(\upsilon)}$, it is believed that the formula with integral form $W_{\mathrm{u}} = \int_{\upsilon_0}^{\upsilon} h\left(1 - T_0 \big/ T_{(\upsilon)}\right)d\upsilon$ should be used to represent the exergy of monochromatic photons, which can reflect the difference between radiative energy and thermal energy.

The equivalent temperature of monochromatic photon $T_{(\lambda)}$ is proportional to radiation temperature T and inversely proportional to wavelength λ. The higher the equivalent temperature $T_{(\lambda)}$, the greater the exergy of monochromatic photons.

An approximate formula exists to calculate monochromatic photon equivalent temperature $T_{(\lambda)}$ from the radiation temperature T and wavelength λ is given. When $T > T_0$ and $T < T_0$, $4.5638 \times 10^{-3} T^3 = \lambda T_{(\lambda)}^4$ and $5.33 \times 10^{-3} T^3 = \lambda T_{(\lambda)}^4$, respectively. Based on this equivalent temperature expression, the formula of exergy-to-energy

ratio η_u for a monochromatic photon can be obtained as $\eta_u = 1 - \frac{4}{3}\frac{T_0}{T_{(\lambda)}} + \frac{1}{3}\left(\frac{T_0}{T_{(\lambda)}}\right)^4$, which is similar to Petela's coefficient formula and is simple and easy to apply. The calculation of the exergy of blackbody radiation shows that the error of this formula is negligible at high temperatures, being no more than 10^{-8}. The exergy-to-energy ratio of monochromatic radiation in blackbody surface radiation agrees with previous studies. Using the emission spectrum of engineering radiation, this formula can be used to conveniently calculate radiative exergy in most engineering fields.

The entropy expression of monochromatic radiation photons should be the integral form $s_v = \int_0^v h \Big/ T_{(\lambda)} dv$ based on the concept of monochromatic photon equivalent temperature. It can reflect the distinctions between radiative energy and thermal energy. The entropy and exergy of monochromatic photons presented in this book satisfy the thermodynamic relation, indicating that they are essentially harmonious.

References

1. Petela R (1964) Exergy of heat radiation. J Heat Transfer 86(2):187–192
2. Jeter SM (1981) Maximum conversion efficiency for the utilization of direct solar radiation. Sol Energy 26(3):231–236
3. Lewins JD (2003) Thermodynamics of radiation. Int J Mech Eng Educ 31(4):283–309
4. De Vos A, Pauwels H (1983) Comment on a thermodynamical paradox presented by P. Wurfel. J Phys C: Solid State Phys 16(36):6897
5. Spanner DC (1964) Introduction to thermodynamics. Academic Press, London
6. Landsberg PT, Tonge G (1979) Thermodynamics of the conversion of diluted radiation. J Phys A: Math Gen 12(4):551–562
7. Landsberg PT, Baruch P (1989) The thermodynamics of the conversion of radiation energy for photovoltaics. J Phys A: Math Gen 22:1911–1926
8. Badescu V (1990) On the thermodynamics of the conversion of diluted radiation. J Phys D Appl Phys 23:289–292
9. Sieniutycz S, Kuran P (2006) Modeling thermal behavior and work flux in finite-rate systems with radiation. Int J Heat Mass Transf 49:3264–3283
10. Laptev VI (2005) Conversion of solar heat into work: a supplement to the actual thermodynamic description. J Appl Phys 98(12):124905
11. Wright SE, Rosen MA (2004) Exergetic efficiencies and the exergy content of terrestrial solar radiation. J SolEnergy Eng 126:673–676
12. Bejan A (1987) Unification of three different theories concerning the ideal conversion of enclosed radiation. J SolEnergy Eng 109(1):46–51
13. Wright SE, Rosen MA, Scott DS et al (2002) The exergy flux of radiative heat transfer for the special case of blackbody radiation. Exergy Int J 2(1):24–33
14. Carter AH (2001) Classical and statistical thermodynamics. Pearson Education India
15. Petela R (2003) Exergy of undiluted thermal radiation. Sol Energy 74(6):469–488
16. Petela R (2010) Engineering thermodynamics of thermal radiation for solar power utilization. McGraw Hill, NewYork
17. Wright S (2007) Comparative analysis of the entropy of radiative heat transfer and heat conduction. Int J Thermodyn 10(1):27–35
18. Badescu V (2008) Exact and approximate statistical approaches for the exergy of blackbody radiation. Cent Eur J Phys 6(2):344–350
19. Markvart T, Bauer GH (2012) What is the useful energy of a photon? Appl Phys Lett 101(19):193901

20. Duysens LNM (1958) The path of light in photosynthesis. Brookhaven Symp Biol 11:18–25
21. Knox RS (1977) Photosynthetic efficiency and exciton transfer and trapping. Primary Process Photosynthesis 2:55–97
22. Lems S, Van Der Kooi HJ, De Swaan AJ (2010) Exergy analyses of the biochemical processes of photosynthesis. Int J Exergy 7(3):333–351
23. Juretić D, Županović P (2003) Photosynthetic models with maximum entropy production in irreversible charge transfer steps. Comput Biol Chem 27(6):541–553
24. Lavergne J, Joliot P (2000) Thermodynamics of the excited states of photosynthesis. Energy transduction in membranes. WA Cramer, Rockville Biophysical Society
25. Meszéna G, Westerhoff HV, Somsen O (2000) Reply to comment on non-equilibrium thermodynamics of light absorption. J Phys A: Math Gen 33(6):1301
26. Chen Z, Mo S (2007) Effective temperature and exergy of monochromic blackbody radiation. Prog Nat Sci 17(10):1250–1254
27. Petela R (2009) Radiation spectra of surface. Int J Exergy 7(1):89–109
28. Modest MF (2003) Radiative heat transfer. Academic Press
29. Planck M (1914) The theory of heat radiation. Philadelphia Blakistons
30. Ito E, Komatsu T, Suzuki H (1998) The entropy generation in visual-pigment system by the absorption of light. Biophys Chem 74(1):59–70
31. Kirwan AD (2004) Intrinsic photon entropy? The darkside of light. Int J Eng Sci 42(7):725–734

Chapter 3
Gas Radiation Model Under Complex Combustion Conditions

The actual combustion chambers (e.g., pressurized boilers, gas turbines, internal combustion engines, and aircraft engines) are all pressurized. Additionally, many triatomic gases exist in the flue gas during oxy-fuel combustion (CO_2). Thus, investigating gas radiation models under complex combustion conditions (e.g., high-pressure environments and oxy-fuel atmospheres) is critical. The first section of this chapter summarizes the steps and methods for developing a new efficient and accurate WSGG model based on the benchmark model. Second, the EM2C laboratory's SNB model is used as a benchmark to improve the WSGG model and establish a new set of correlations for a broader range of parameters for H_2O/CO_2 mixtures, adapting to radiation heat transfer calculations under complex combustion conditions. The new WSGG model and its parameters are suitable for pressure, temperature, path-length, and molar ratio ranges of 1–30 bar, 500–2500 K, 0.001–60 m, and 0.125–4 for H_2O/CO_2, respectively. Thus, the new WSGG model is suitable for a wide range of fuels under pressurized conditions. When compared to the benchmark model, the one-dimensional case results show that the new WSGG model can accurately predict the radiation heat transfer of the gas mixture under pressurized conditions. Furthermore, the new model is used to investigate the effect of pressure on the radiation heat transfer of the gas mixture. The findings show that increasing the pressure within a certain range can improve the radiation heat transfer of a gas mixture, and this effect is also related to temperature, molar ratio, and path-length. In conclusion, the new WSGG model can be used to calculate and study actual combustion conditions as well as provide a theoretical foundation for the study of radiative energy utilization.

Revised from Shan et al., New pressurized WSGG model and the effect of pressure on the radiation heat transfer of H_2O/CO_2 gas mixtures, International Journal of Heat and Mass Transfer, Copyright (2018), with permission from Elsevier.

Revised from Shan et al., New weighted-sum-of-gray-gases model for typical pressurized oxy-fuel conditions, International Journal of Energy Research, Copyright (2017), with permission from John Wiley and Sons.

S. Shan et al., *Fundamentals of Thermal Radiation for Energy Utilization in Fuel Combustion*, Advanced Topics in Science and Technology in China 67,
https://doi.org/10.1007/978-981-19-8311-5_3

3.1 Non-gray Gas Radiation Models

3.1.1 SNB Model

The SNB model is a band model that was proposed by Malkmus in 1967 [1]. It is the model closest to the LBL model among all gas radiation characteristics models and is frequently used as a reference model for comparison. The SNB model divides the spectrum into many small wavenumber intervals $\Delta\nu$; it is assumed that each wavenumber interval $\Delta\nu$ contains N spectral lines with a random distribution of the intensity or location. Thus, the probability of a spectral line appearing in any position of $\Delta\nu$ is the same. For the wavenumber interval $\Delta\nu$, it is assumed that the intensity of blackbody radiation is constant in the wavenumber interval $\Delta\nu$; thus, $\Delta\nu$ should be sufficiently small. However, $\Delta\nu$ cannot be too small to ensure the validity of the statistical spectral distribution. The wavenumber interval $\Delta\nu$ is generally selected to be from 5 to 50 cm^{-1}.

The SNB model parameters developed by EM2C Laboratory (France) in 1997 [2] have been demonstrated in many SNB model databases to be closest to those of the LBL model based on the HITEMP2010 database, and this SNB model has been recommended as a benchmark [3, 4]. Furthermore, the EM2C laboratory developed new SNB parameters in 2012 [5]; the CO_2 and H_2O parameters of this model are based on the CSCD-4000 and HITEMP databases, respectively. However, recent studies showed that when the two EM2C SNB models are used under pressurized oxy-fuel combustion conditions, the early SNB models are much closer to the LBL model based on the HITEMP2010 database [6].

The SNB model of the EM2C divides the spectrum into narrow bands of 25 cm^{-1}, and the transmittance of an isothermal homogeneous gas mixture in a band is expressed as

$$\overline{\tau}_v = \exp\left[-\frac{2\overline{\gamma}}{\delta}\left(\sqrt{1+\frac{XPL\overline{k}\overline{\delta}}{\overline{\gamma}}}-1\right)\right] \tag{3.1}$$

where the EM2C database provides the parameters $\overline{k}$ and $\overline{\delta}$, and the average spectral half-width $\overline{\gamma}$ is calculated by solving the following equations:

$$\overline{\gamma}_{H_2O} = \frac{P}{P_{ref}}\left\{0.462\frac{T_{ref}}{T}X_{H_2O} + \left(\frac{T_{ref}}{T}\right)^{0.5} \times \begin{bmatrix} 0.0792\left(1-X_{CO_2}-X_{O_2}\right) \\ +0.106X_{CO_2}+0.036X_{O_2} \end{bmatrix}\right\} \tag{3.2}$$

$$\overline{\gamma}_{CO_2} = \frac{P}{P_{ref}}\left(\frac{T_{ref}}{T}\right)^{0.7}\left[0.07X_{CO_2} + 0.058\left(1-X_{CO_2}-X_{H_2O}\right) + 0.1X_{H_2O}\right] \tag{3.3}$$

where $P_{\text{ref}} = 1$ bar and $T_{\text{ref}} = 296$ K. An increase in pressure primarily influences the radiation characteristics by affecting the average spectral half-width $\overline{\gamma}$ and the pressure term P in Eqs. (3.2) and (3.3). Thus, the gas transmittance decreases as the pressure increases.

3.1.2 WSGG Model and Improvement

The WSGG model was first proposed by Hotel [7], and the relevant radiation heat transfer calculation was performed using the WSGG model in conjunction with the regional method. Modest [8] pointed out that the WSGG model considers the absorption coefficient and is not limited to calculating total emissivity. This model can also be used to solve the radiation transfer equation and is suitable for the arbitrary solution method of the radiation transfer equation. The core idea of the WSGG model is to use the n gray gases to represent the actual non-gray gas; the total emissivity or the radiative heat flux of each gray gas is multiplied by the weight, and the total value equals their sum [9]. The emissivity on the path-length L through the WSGG model can be expressed as

$$\varepsilon = \sum_{i=1}^{n} a_i \left[1 - \exp(-\kappa_i X P L\right] \tag{3.4}$$

where X is the mole fraction of the gas mixture,, expressed as the sum of the molar fractions of H_2O and CO_2

$$X = X_{H_2O} + X_{CO_2} \tag{3.5}$$

The absorption coefficient κ_i of each gray gas is constant in a specific spectral region, and a_i represents the ratio of blackbody radiation in this spectral region, which is also known as weight. The sum of the weights must be 1, including the weight of the white gas a_0, and the corresponding absorption coefficient is $\kappa_0 = 0$; thus, there is:

$$\sum_{i=0}^{n} a_i = 1 \tag{3.6}$$

The WSGG model is concerned with calculating the absorption coefficient κ_i and the weighting factor a_i of each gray gas.

3.1.3 Solving the Radiation Transfer Equation Coupled Gas Radiation Model

The radiation transfer equation (RTE) describes the process of radiation transfer in a medium; for a medium with absorption, emission, and non-scattering properties, the radiation transfer equation is [9]

$$\frac{dI_\nu}{ds} = \kappa_\nu I_{b\nu} - \kappa_\nu I_\nu \tag{3.7}$$

where I_ν and $I_{b\nu}$ are the spectral and blackbody spectral emission intensity, respectively. The left side of the RTE represents the change of radiation intensity at a point along the path-length in the medium. The first term on the right represents the emission intensity at a point along the path-length in the medium, and the second represents the radiation intensity absorbed at a point along the path-length in the medium.. The RTEs for the entire spectrum as well as all spatial directions must be calculated to obtain the radiation transfer of the entire space.

Numerous approaches were noted to solve the RTE. The discrete coordinate method (DOM) was used in this book because it had broad applicability [10]. Following that, the DOM for the RTE coupled with the WSGG and SNB models is represented in one- and two-dimensional settings.

The RTE of each gray gas in the WSGG model was solved for the radiation transfer problem under the one-dimensional condition and the results of four gray gases were then summed. For each gray gas, the RTE can be written as:

$$\frac{dI_i(x,\hat{\boldsymbol{s}})}{ds} = \kappa_i a_i I_b(x) - \kappa_i I_i(x,\hat{\boldsymbol{s}}) \tag{3.8}$$

where the blackbody emission intensity is expressed as $I_b(x) = \sigma T(x)^4 \big/ \pi$; the items in Eq. (3.8) are determined based on the state at position x. Figure 3.1a depicts the solution diagram of the one-dimensional RTE for the DOM. The one-dimensional transfer directions are divided into positive and negative series during the solution process, the cosine of the angle between each direction and the x-axis is u_l, and the direction weight is w_l. Thus, the RTE in each direction can be expressed as follows:

$$\mu_l \frac{dI_i^+(x,\hat{\boldsymbol{s}})}{dx} = \kappa_i a_i(x) I_b(x) - \kappa_i I_i^+(x,\hat{\boldsymbol{s}}) \tag{3.9a}$$

$$-\mu_l \frac{dI_i^-(x,\hat{\boldsymbol{s}})}{dx} = \kappa_i a_i(x) I_b(x) - \kappa_i I_i^-(x,\hat{\boldsymbol{s}}) \tag{3.9b}$$

Given that the left and right sides are blackbody walls, x_0 and x_s represent the left and right wall positions, respectively. Thus, the boundary conditions can be expressed as:

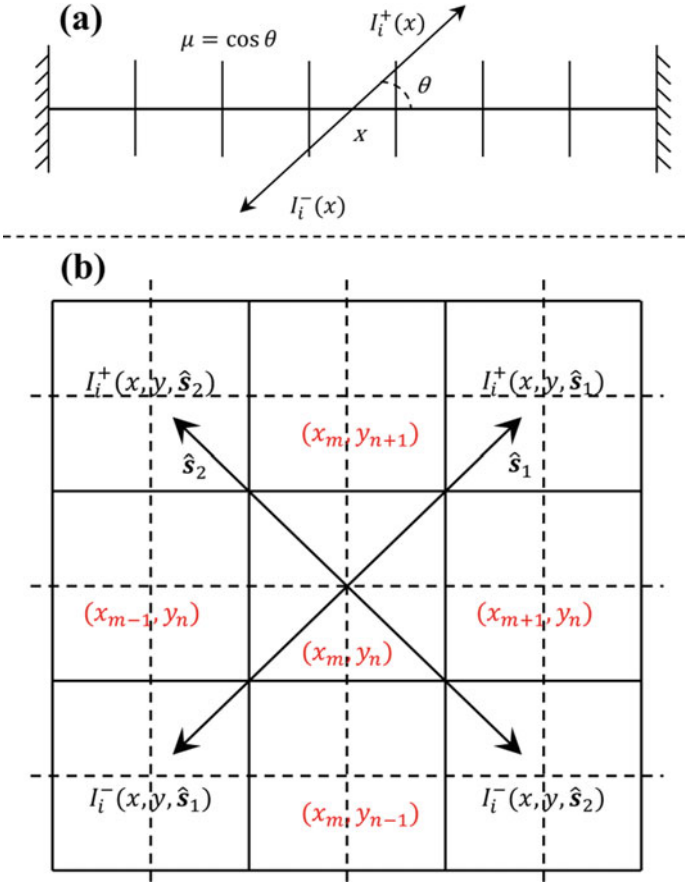

Fig. 3.1 Diagram of DOM calculation process: **a** one-dimensional case and **b** two-dimensional case

$$I_i^+(x_0, l) = I_{\mathrm{b},i}(x_0) \tag{3.10a}$$

$$I_i^-(x_s, l) = I_{\mathrm{b},i}(x_s) \tag{3.10b}$$

The one-dimensional axis was divided into some computing units; therefore, the partial differential equation was written as a difference equation for each unit, and the latter format was selected as the differential way. The discrete form of the difference equation is as follows:

$$I_i^+(x_m, l) = \frac{\mu_l I_i^+(x_{m-1}, l) + \kappa_i I_{\mathrm{b},i}(x_m)\Delta x}{\mu_l + \kappa_i \Delta x} \tag{3.11a}$$

$$I_i^-(x_m, l) = \frac{\mu_l I_i^-(x_{m+1}, l) + \kappa_i I_{\mathrm{b},i}(x_m)\Delta x}{\mu_l + \kappa_i \Delta x} \tag{3.11b}$$

After calculating the intensity of the emission along the path-length, the radiative heat flux q and the radiation source $\dot{q}$ can be written as:

$$q_m = \sum_i \sum_l 2\pi \mu_l w_l [I_i^+(x_m, l) - I_i^-(x_m, l)] \tag{3.12a}$$

$$\dot{q}_m = \sum_i \sum_l \{2\pi \kappa_i w_l [I_i^+(x_m, l) + I_i^-(x_m, l)] - 4\pi \kappa_i w_l I_{\mathrm{b},i}(x_m)\} \tag{3.12b}$$

The radiation heat flux q and the radiation source term $\dot{q}$ in the calculation of radiation transfer were mainly investigated. Additionally, the radiation source term $\dot{q}$ can be added to the energy equation of the CFD as a part of the source term for the numerical simulation of a practical problem.

As demonstrated in Sect. 3.1.1, the SNB model can be used to calculate the transmittance of a given path-length. Additionally, the emissivity can be determined using the relationship between transmittance and emissivity. Thus, the average emissivity is expressed as

$$\overline{\varepsilon}_L = 1 - \exp(-\overline{\kappa} X P L) \tag{3.13}$$

The average absorption coefficient $\overline{\kappa}$ of the path-length L can be calculated using Eq. (3.13). When solving the RTE, the entire spatial region was divided into many small calculation units. Furthermore, the gas mixture medium can be considered a homogeneous gas within a small path-length Δx of each unit. Thus, the spectral absorption coefficient κ_ν can be calculated from the transmittance of the unit path-length Δx by using the SNB model. Thus, the RTE can be written as:

$$\frac{dI_\nu(x, \hat{\boldsymbol{s}})}{ds} = \kappa_\nu a_\nu I_\mathrm{b}(x) - \kappa_\nu I_\nu(x, \hat{\boldsymbol{s}}) \tag{3.14}$$

The DOM was used to solve the RTE for each band of the SNB model, and the results were then summed. The radiation heat flux q and the radiation source term $\dot{q}$ were then calculated, and the detailed processes are similar to those of the WSGG model.

For the radiation transfer problem under the two-dimensional condition, the WSGG model was used to describe the radiation characteristics. The radiation transfer equation for DOM can be written as shown in Eq. (3.15), where μ_l or η_l is the cosine of the angle between the discrete direction and the x- or y-axis. Moreover, Fig. 3.1b depicts the calculation diagram:

$$\mu_l \frac{\partial I_i(x, y, \hat{\boldsymbol{s}})}{\partial x} + \eta_l \frac{\partial I_i(x, y, \hat{\boldsymbol{s}})}{\partial y} = \kappa_i I_{i,\mathrm{b}}(x) - \kappa_i I_i(x, y, \hat{\boldsymbol{s}}) \tag{3.15}$$

The radiation transfer calculation was performed in a two-dimensional plane region along two diagonal directions, as shown in Fig. 3.1b. Thus, there are two major directions $\hat{\boldsymbol{s}}_1$ and $\hat{\boldsymbol{s}}_2$; moreover, each major direction includes both positive and negative directions. Consequently, four groups of directions exist when the discrete ordinate method is used. If the specific direction of each group is represented by the subscript l, the radiation transfer equations of the positive and negative directions of $\hat{\boldsymbol{s}}_1$ can be written as:

$$\mu_l \frac{\partial I_i^+(x, y, \hat{\boldsymbol{s}}_1)}{\partial x} + \eta_l \frac{\partial I_i^+(x, y, \hat{\boldsymbol{s}}_1)}{\partial y} = \kappa_i I_{i,\mathrm{b}}(x) - \kappa_i I_i^+(x, y, \hat{\boldsymbol{s}}_1) \tag{3.16a}$$

$$\mu_l \frac{\partial I_i^-(x, y, \hat{\boldsymbol{s}}_1)}{\partial x} + \eta_l \frac{\partial I_i^-(x, y, \hat{\boldsymbol{s}}_1)}{\partial y} = \kappa_i I_{i,\mathrm{b}}(x) - \kappa_i I_i^-(x, y, \hat{\boldsymbol{s}}_1) \tag{3.16b}$$

The calculation region was divided into a square lattice; thus, $\Delta x = \Delta y$. The difference format is as follows:

$$I_i^+(x_m, y_n, l) = \frac{\mu_l I_i^+(x_{m-1}, y_n, l) + \eta_l I_i^+(x_m, y_{n-1}, l) + \kappa_i I_{\mathrm{b},i}(x_m, y_n)\Delta x}{\mu_l + \eta_l + \kappa_i \Delta x} \tag{3.17a}$$

$$I_i^-(x_m, y_n, l) = \frac{\mu_l I_i^-(x_{m+1}, y_n, l) + \eta_l I_i^-(x_m, y_{n+1}, l) + \kappa_i I_{\mathrm{b},i}(x_m, y_n)\Delta x}{\mu_l + \eta_l + \kappa_i \Delta x} \tag{3.17b}$$

Similarly, the positive and negative radiation transfer equations of $\hat{\boldsymbol{s}}_2$ are analogous.

When the SNB model is used under the two-dimensional condition, the DOM with the SNB model is similar to that with the WSGG model. However, unlike the WSGG model, which needs only the bands of four gray gases for calculations, the SNB model needs the radiation transfer equations of all the narrow bands to be solved and the results to be added together. Thus, the RTE can be written as follows:

$$\mu_l \frac{\partial I_\nu(x, y, \hat{\boldsymbol{s}})}{\partial x} + \eta_l \frac{\partial I_\nu(x, y, \hat{\boldsymbol{s}})}{\partial y} = \kappa_\nu I_{\nu,\mathrm{b}}(x, y) - \kappa_\nu I_\nu(x, y, \hat{\boldsymbol{s}}) \tag{3.18}$$

Similar to the one-dimensional condition, as a result of the radiation transfer calculation, the radiation heat flux and radiation source term can be calculated by solving Eq. (3.12) after the radiation intensity for each unit is calculated and all are summed.

3.2 Development of WSGG Model Under Complex Combustion Conditions

3.2.1 New WSGG Model

In this section, the WSGG model is improved to accommodate pressurized conditions. As shown in Eq. (3.4), the WSGG model emissivity contains the pressure term P, and the pressure is $P = 1$ bar at atmospheric pressure. Thus, the WSGG model correlations for atmospheric pressure can also be used under pressurized conditions by changing the pressure term P; however, this introduces significant errors [6]. Therefore, this book presents a new WSGG model for high-pressure conditions. Here the pressure term P with the absorption coefficient κ_i in the Eq. (3.4) is combined as $\kappa_{p,i}$ to represent the absorption coefficient under different pressures. Thus, the emissivity of new WSGG model is expressed as:

$$\varepsilon = \sum_{i=1}^{n} a_i [1 - \exp(-\kappa_{p,i} XL)] \tag{3.19}$$

There are two types of WSGG models for oxy-fuel combustion: those with three gray gases and those with four gray gases. Johansson's study showed that the WSGG model with four gray gases and one white gas is better than that with three gray gases and one white gas [11]. Currently, the majority of the WSGG models proposed by scholars for oxy-fuel combustion have four gray gases. Thus, the model containing four gray gases and one white gas is chosen to investigate the new WSGG model correlations for pressurized oxy-fuel combustion; thus, $n = 4$. In the WSGG model, the weight value a_i is mainly dependent on temperature; thus, a_i can be expressed as the polynomial of the dimensionless temperature term with m-th power

$$a_i = \sum_{j=0}^{m} c_{i,j} \left(\frac{T}{T_{\text{ref}}} \right)^{m-j} \tag{3.20}$$

In Eq. (3.20), T_{ref} is the reference temperature, which can make the polynomial coefficient $c_{i,j}$ dimensionless, so as to improve the accuracy of the polynomial [11, 12]. The recommended value of T_{ref} is 2000 K in the literature [13] for higher model accuracy, and this value is also used here. As shown in Eq. (3.21), the polynomial coefficient $c_{i,j}$ and the absorption coefficient κ_i with same molar ratio M and different pressures are expressed as the polynomial of pressure:

$$c_{i,j} = C2_{i,j} P^2 + C1_{i,j} P + C0_{i,j} \tag{3.21a}$$

$$\kappa_i = K2_i P^2 + K1_i P + K0_i \tag{3.21b}$$

In this book, the molar ratio of H_2O to CO_2 is represented by M:

$$M = X_{H_2O}/X_{CO_2} \tag{3.22}$$

To improve the accuracy of the polynomial in Eq. (3.22), piecewise fitting within different pressure ranges is used.

3.2.2 *Fitting Process of WSGG Model Correlations*

In this section, the detailed fitting process of WSGG model correlations under pressurized conditions is elaborated.

(1) First, the SNB model of the EM2C database was used to calculate the emissivity of a gas mixture over a pressure range of 1–30 bar; then, the emissivity table was established as a database. Under each pressurized condition, the molar ratio range was 0.125–4, the temperature range was 500–2500 K, and the path-length range was 0.001–60 m.

When calculating emissivity under various conditions with the SNB model, the transmittance $\overline{\tau}_\nu$ in a narrow band was first calculated using Eq. (3.1), and the emissivity in the narrow band of the gas mixture was then calculated using Kirchhoff's law and the relationship between the gas transmittance and the absorptivity:

$$\overline{\varepsilon}_\nu = \overline{\alpha}_\nu = 1 - \overline{\tau}_\nu \tag{3.23}$$

The emission intensity in the narrow band I_ν was then calculated, followed by the sum of all emission intensities to obtain the emission intensity I for the entire spectral range. The emission intensity in the narrow band I_ν is

$$I_\nu = I_{b\nu} \times \overline{\varepsilon}_\nu \tag{3.24}$$

The gas emissivity was calculated as:

$$\varepsilon = I/I_b \tag{3.25}$$

where the blackbody emission intensity was calculated using Stefan-Boltzmann's law:

$$I_b = \sigma T^4/\pi \tag{3.26}$$

The entire calculation process is depicted in Fig. 3.2.

(2) The purpose of this second step was mainly to determine the absorption coefficient κ_i of each gray gas. For a gas mixture with a certain molar ratio under a certain pressure condition, there is a certain absorption coefficient κ_i. Therefore, in the SNB model emissivity table with a certain pressure P and a certain molar ratio M, for each

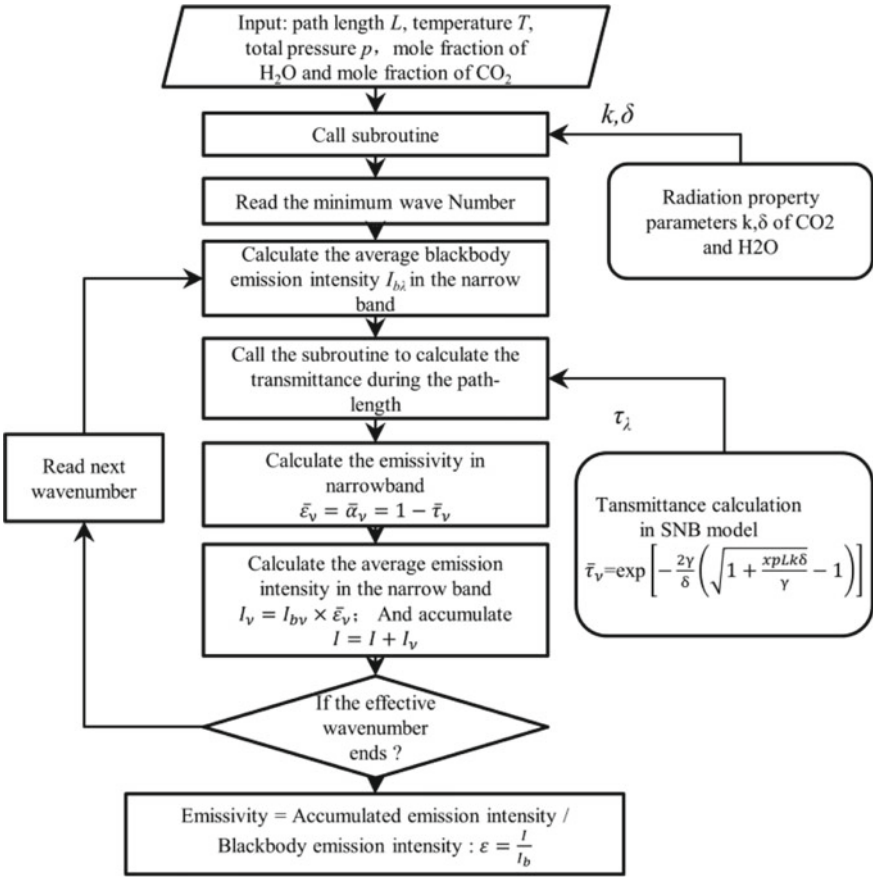

Fig. 3.2 Emissivity calculation process using the SNB model

certain path-length, all emissivity values with different temperatures were added to determine the sum of emissivity ε_L, which is only associated with the path-length L:

$$\varepsilon_L = \sum_t \varepsilon_{t,L} \tag{3.27}$$

where ε_L is expressed in the form of Eq. (3.28) in the WSGG model:

$$\varepsilon_L = \sum_{i=1}^{n} A_i[1 - \exp(-\kappa_i X L)] \tag{3.28}$$

where A_i is the sum of the single gray gas weights a_i at different temperatures:

$$A_i = \sum_t a_{i,t} \tag{3.29}$$

The optimal absorption coefficient κ_i was determined by minimizing the difference between the ε_L calculated by using the SNB model and that calculated by using the WSGG model for different path-lengths. During the optimal process, we used the sequential quadratic programming (SQP) algorithm, which is a constrained optimization algorithm that was achieved using the MATLAB software. After this step, the κ_i of each molar ratio M can be determined.

(3) The third step was to determine the weight $a_{i,t}$ at different temperatures and values of the polynomial coefficient $c_{i,j}$. During this step, first, $a_{i,t}$ was determined for a certain pressure and a certain molar ratio. Considering the absorption coefficient κ_i that was determined in the second step, the weight coefficients $a_{i,t}$ at each specific temperature T can be determined by minimizing the sum of differences between $\varepsilon_{t,L}$ calculated by using the SNB model and that calculated by using the WSGG model for different path-lengths. In this process, the SQP algorithm was again used. After determining the weight coefficient $a_{i,t}$ at different temperatures, the nonlinear polynomial regression analysis was used to determine the polynomial coefficient $c_{i,j}$ in Eq. (3.20).

(4) The final step was to determine the coefficients of the molar ratio polynomial, i.e., $C0_{i,j}$, $C1_{i,j}$ and $C2_{i,j}$, in Eq. (3.21a) and the coefficients $K0_i$, $K1_i$ and $K2_i$ in Eq. (3.21b). The nonlinear polynomial regression analysis method was used to determine the coefficients in this process. To ensure accuracy, the piecewise fitting method was used and the pressure range was divided into six segments (1–2, 2–4, 4–6, 6–10, 10–20, and 20–30, bar) during the actual fitting process.

The following subsection describes the new WSGG model correlation coefficients.

3.2.3 *WSGG Model Coefficients for Complex Combustion Conditions*

In order to make the new model suitable to the pressure range of 1–30 bar, piecewise fit was used to improve polynomial accuracy in different pressure ranges,. Considering most combustion chambers are in the temperature range of 500–2500 K, the new model uses this temperature range [14–17] Additionally, the temperature range of many published WSGG models is included in it [13, 18, 19]. The path-length range is 0.001–60 m, which covers nearly the entire size range of the combustion chambers [20–22]. The model is also suitable for a broad molar ratio range of 0.125–4, which can represent various organic fuels, where M is 0.5 for acetylene and benzene, M is 1 for olefins and many oil fuels [23, 24], and M is 2 for the combustion of methane or methanol. In addition, the molar ratio M less than 1 can represent the dry cycle conditions of oxy-fuel combustion, while the M more than or equal to 1 can represent the wet cycle conditions oxy-fuel combustion [11–13].

Table 3.1 The method for applying a new WSGG model in CFD calculation [12]

If (MR $\leq$ 0.2)	Use parameters for	MR = 0.125
Else if (MR $\leq$ 0.4)	Use parameters for	MR = 0.25
Else if (MR $\leq$ 0.6)	Use parameters for	MR = 0.5
Else if (MR $\leq$ 0.9)	Use parameters for	MR = 0.75
Else if (MR $\leq$ 1.1)	Use parameters for	MR = 1
Else if (MR $\leq$ 2.5)	Use parameters for	MR = 2
Else	Use parameters for	MR = 4

According to the development process of WSGG model described in Sect. 3.2, new model coefficients such as $C0$, $C1$, $C2$ and $K0$, $K1$, $K2$ can be obtained. The new WSGG model parameters are shown in the appendix of this book, which includes seven tables with different M (i.e., 0.125, 0.25, 0.5, 0.75, 1, 2, and 4).

There are two methods to use new WSGG model for a given MR. The first method was presented in literature [12] by Yin et al., and it recommends a specific table for a given M in actual CFD calculation, with the detailed method being shown in Table 3.1. The second method is the linear interpolation method to use two table results for a given M.

To compare these two methods, the emissivity of the gas mixture was investigated for two cases with the M of 0.15 and 1.5; moreover, the temperature of gas mixture is 1500 K and the pressure is 5 bar. The results are shown in Fig. 3.3.

It can be seen from Fig. 3.3 that the results of the two methods were similar when compared with the SNB benchmark solution. In general, the linear interpolation method is slightly more accurate than the specific table method. However, this advantage is not immediately apparent, and the linear interpolation method is relatively more complex. The specific table method is simpler and more convenient. Furthermore, it has been presented by scholars and applied in CFD calculation in previous

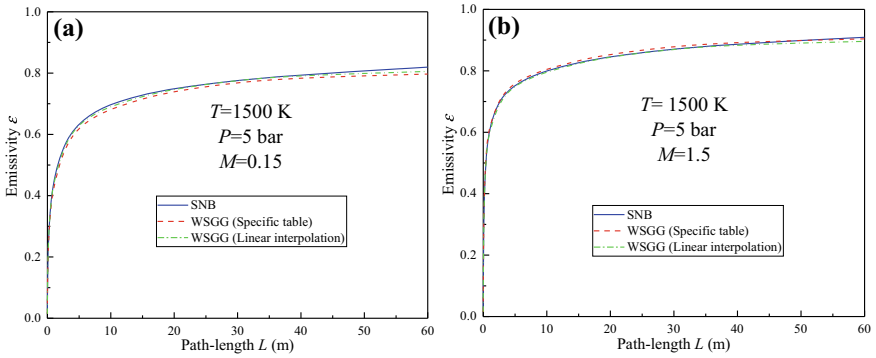

Fig. 3.3 Comparison between two methods for applying new WSGG model for a given MR (1500 K, 5 bar): **a** MR = 0.15 and **b** MR = 1.5

research. Although a minor error exists, it is not visible. Thus, the specific table method in Table 3.1 is recommended first for a given M in actual CFD calculations.

3.3 Model Calculation Results

3.3.1 Design of Investigated Cases

In order to investigate the applicability of the new model under high pressure conditions and the effect of pressure on the radiation heat transfer of the gas mixture, the one-dimensional infinite parallel plates cases are used in this study because one-dimensional calculation is not only simple but also enough to investigate the accuracy of the model and the effect of pressure on the radiation heat transfer. Thus, many studies used one-dimensional cases [11–13, 18, 19]. In the course of investigating model accuracy, non-isothermal homogeneous cases and non-isothermal non-homogeneous cases were chosen for study because non-isothermal conditions are more consistent with real conditions. Furthermore, the two boundary plates are blackbody walls with temperatures of 1000 K, the temperature distribution between the plates can be found in [13, 25, 26], and this temperature distribution is similar to that of a real furnace

$$T = 1400 - 400\cos\left(\frac{2\pi x}{L}\right)\ (\mathrm{K}) \tag{3.30}$$

where x is the position of the one-dimensional length coordinate, and L is the distance between the two plates. For non-isothermal, homogeneous conditions (case 1 series), five cases with different M of 0.25, 0.5, 1, 2, and 4 were selected. The total molar fraction was set to 0.9, which covers both air–fuel and oxy-fuel conditions [27]. Table 3.2 displays the specific information.

For the non-homogeneous conditions, similar to literature [18], the molar fractions of H_2O and CO_2 are varying, while the molar ratio remains constant. In this study, three different cases with the M of 0.5, 1, and 2 were selected; furthermore, the molar

Table 3.2 Non-isothermal and homogeneous case conditions (case 1 series)

Non-isothermal homogeneous					
Case	T (K)	X_{H_2O}	X_{CO_2}	M	X
1.1	Equation (3.30)	0.18	0.72	0.25	0.9
1.2	Equation (3.30)	0.3	0.6	0.5	0.9
1.3	Equation (3.30)	0.45	0.45	1	0.9
1.4	Equation (3.30)	0.6	0.3	2	0.9
1.5	Equation (3.30)	0.72	0.18	4	0.9

Table 3.3 Non-isothermal and non-homogeneous case conditions (case 2 series)

Non-isothermal non-homogeneous				
Case	T (K)	X_{H_2O}	M	X (range)
2.1	Equation (3.30)	Equation (3.31a)	0.5	0.6–0.9
2.2	Equation (3.30)	Equation (3.31b)	1	0.64–0.96
2.3	Equation (3.30)	Equation (3.31c)	2	0.6–0.9

fraction distributions of H_2O in these three cases are expressed as Eq. (3.31), and the specific information of the cases is shown in Table 3.3. Furthermore, when solving RTE with DOM, the S_8 discrete format is used.

$$X_{H_2O} = 0.25 + 0.05\cos\left(\frac{2\pi x}{L}\right) \tag{3.31a}$$

$$X_{H_2O} = 0.4 + 0.08\cos\left(\frac{2\pi x}{L}\right) \tag{3.31b}$$

$$X_{H_2O} = 0.5 + 0.1\cos\left(\frac{2\pi x}{L}\right) \tag{3.31c}$$

3.3.2 Emissivity Results

In this section, the accuracy of new model in the emissivity calculation is investigated under pressurized oxy-fuel conditions, and the influence of the pressure, temperature, and molar ratio on the emissivity of the gas mixture is also investigated.

First, the results of the benchmark in this study were compared with the results published in [27] using the same model (SNB model of EM2C) to verify the accuracy of the benchmark model used in this study. Figure 3.4 shows the comparison of the emissivity from the SNB model with the published emissivity results. The results of the SNB model used in this paper were consistent with previously published benchmark results [27], indicating that the SNB model of EM2C in this paper is accurate and can be used as benchmark.

First, the new WSGG model was used to predict the emissivity of the gas mixture, and the results were compared to the benchmark solution. In addition, Fig. 3.5 depicts the emissivity of a gas mixture calculated using the WSGG model and the benchmark SNB model under various conditions.

Figure 3.5a depicts the emissivity of the gas mixture at different pressures of 1 (atmospheric), 2, 5, 15, and 30 bar with a path-length range of 0.001–60 m with a temperature of 1500 K and molar ratio of 1. It can be seen that the results of the WSGG model are in good agreement with that of the SNB model, indicating that the new WSGG model has suitable accuracy when calculating the emissivity at a

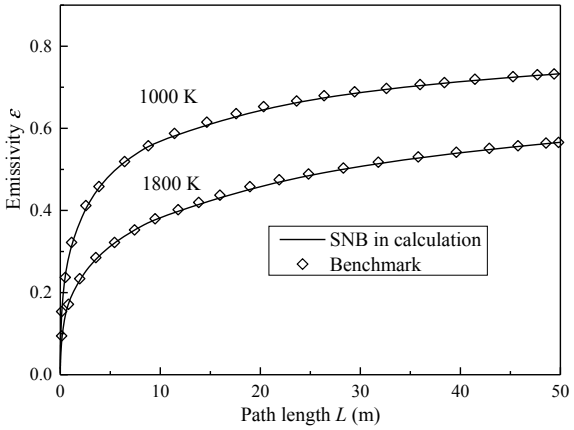

Fig. 3.4 Comparison of the emissivity calculated using the SNB model with the published emissivity results in literature

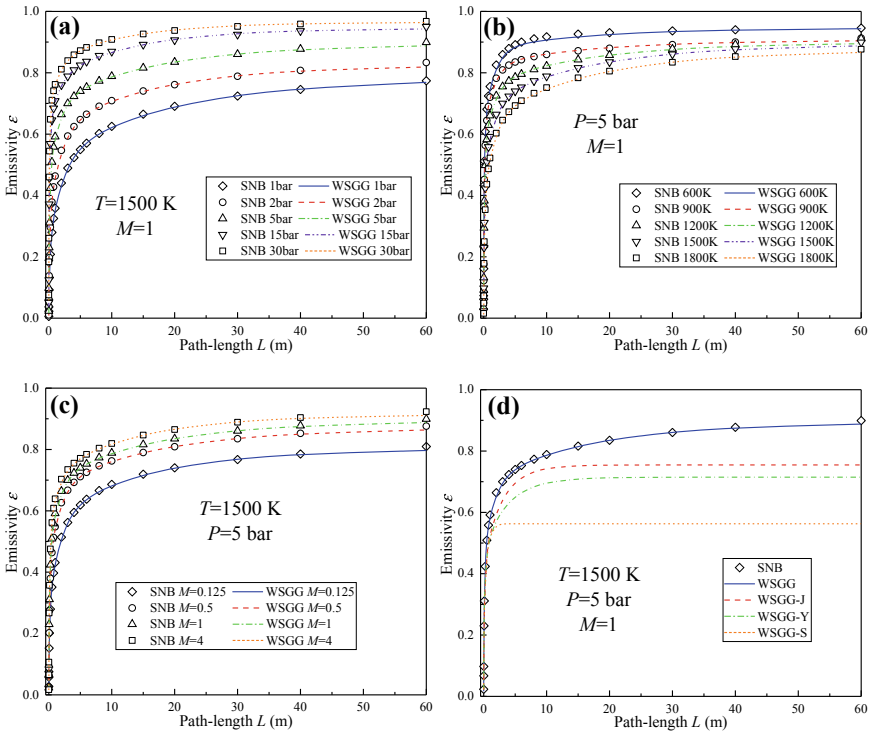

Fig. 3.5 Emissivity of the gas mixture **a** at different pressures (1500 K, $M = 1$), **b** at different temperatures (5 bar, $M = 1$), **c** with different molar ratios (5 bar, 1500 K), and **d** calculated by different WSGG models (5 bar, 1500 K, $M = 1$)

high pressure. In addition, the emissivity of the gas mixture was greater when the pressure was raised; furthermore, the emissivity increased quickly when the pressure was below 5 bar while slowly when the pressure was higher than 5 bar. This result indicates that elevating the pressure can enhance the emissivity of the gas mixture and that the effect of pressure on the emissivity is reduced as the pressure increases. Furthermore, there is a significant effect of pressure on the emissivity when the pressure is below 5 bar.

The emissivity at different temperatures with a molar ratio of 1 at a pressure of 5 bar is shown in Fig. 3.5b, and it can be found that the results of the WSGG model were consistent with that of the SNB model. As shown in Fig. 3.5b, the emissivity of the gas mixture was reduced when the temperature increased from 600 to 1800 K; furthermore, the decrease of emissivity from 600 to 1200 K was more than that from 1200 to 1800 K. This indicates that the emissivity of the gas mixture decreases with the temperature and that the effect of temperature is reduced as the temperature increases under high-pressure conditions; this is consistent with the results in the literature [13].

Figure 3.5c shows the emissivity of the gas mixture with different molar ratios at a temperature of 1500 K and pressure of 5 bar. Through comparing the cases with different molar ratios of 0.125, 0.5, 1, and 4, it can be seen that the increase of molar ratio could enhance the emissivity of the gas mixture, moreover, the increment of emissivity from the M of 0.125 to 0.5 was more than that from the M of 0.5 to 4. This indicates that there is greater emissivity for higher molar ratio under high-pressure conditions and that the effect of M is reduced as the M increases; thus, the higher the ratio of H/C is in the fuel, the greater the emissivity of flue gas. Furthermore, for pressurized oxy-fuel combustion, the flue gas emissivity of the wet cycle condition is higher than that of the dry cycle condition, and the molar ratio has a greater effect on the emissivity of the flue gas in the dry cycle condition than in the wet cycle condition.

Figure 3.5d further shows the emissivity calculated through different WSGG models with a molar ratio of 1 at a temperature of 1500 K and a pressure of 5 bar. The emissivity was calculated through the new pressurized WSGG model (WSGG) proposed in this paper and three WSGG models proposed by Smith (WSGG-S) [28], Yin (WSGG-Y) [12] and Johansson (WSGG-J) [11]. Subsequently, the emissivity results were compared with the benchmark from the SNB model. As shown in Fig. 3.5d, the new WSGG model can accurately predict the emissivity of the gas mixture in the path-length range of 0.001–60 m under high-pressure conditions. Furthermore, the results of the WSGG models proposed by other researchers were quite different from the benchmark, which further indicates that the results are not ideal when the atmospheric WSGG model is applied in high-pressure conditions; thus, it is necessary to develop new pressurized WSGG model [6]. In addition, Johansson's WSGG model is closer to the benchmark than Yin's WSGG model; this is because Yin's model is based on the EWB model, while Johansson's model is based on the SNB model of EM2C, which is the benchmark used in this study. Smith's model was developed in an early year and based on an old database of the wide band model; furthermore, its structure is not optimal, and its path-length range

is limited. Therefore, Smith's model has been completely unsuitable for the radiation characteristic calculation of the gas mixture under high-pressure conditions.

3.3.3 One-Dimensional Case Results

In this section, the results of one-dimensional cases were mainly discussed to verify the adaptability of the new WSGG model under high-pressure conditions. The non-isothermal, homogeneous cases and non-isothermal, non-homogeneous cases described in Sect. 3.3.1 were investigated. Furthermore, each case was evaluated at four different high pressures: 2, 5, and 30 bar; furthermore, three different path-lengths of 1, 5, and 10 m were used in each case for comparison. In the course of numerical calculation, one-dimensional space was divided into 100 grids. The radiation heat transfer results of one-dimensional cases mainly include the radiation heat flux and the radiation source term, which were calculated by the new WSGG model and the SNB model, respectively. Subsequently, the errors were analyzed to determine the accuracy of the new model. In this study, the errors of the radiation heat flux and radiation source term can be defined as [18]:

$$\delta q = \frac{|q_{\mathrm{WSGG}} - q_{\mathrm{SNB}}|}{\max |q_{\mathrm{SNB}}|} \times 100\% \tag{3.32}$$

$$\delta \dot{q} = \frac{|\dot{q}_{\mathrm{WSGG}} - \dot{q}_{\mathrm{SNB}}|}{\max |\dot{q}_{\mathrm{SNB}}|} \times 100\% \tag{3.33}$$

where, symbol 'max' represents the maximum absolute value of the radiation heat flux or the radiation source term calculated by the SNB model. The radiation heat flux error at the wall δq_{wall} and the radiation source error at the midpoint $\delta \dot{q}_{\mathrm{half}}$ were primarily considered in this study because the heat flux error δq_{wall} and source term error $\delta \dot{q}_{\mathrm{half}}$ are typically the largest and are frequently of concern to researchers [13, 18]. Furthermore, in each case, the average heat flux error δq_{avg} and the average source term error $\delta \dot{q}_{\mathrm{avg}}$ were investigated. The errors of the new model in these cases with varying high pressures and path-lengths are listed in Table 3.4.

Table 3.4 was used to investigate the new model errors at various high pressures. In the 5-bar pressurized condition, the maximum wall heat flux error was 14.85% (case 1.5, 10 m), and the average heat flux error was not > 5.9% (case 1.5, 10 m). Additionally, the maximum midpoint source term error was 3.93% (case 1.5, 1 m), and the average source term error was no more than 3.26% (case 1.5, 10 m). For non-homogeneous conditions, the maximum wall heat flux error was 11.28% (case 2.3, 10 m), and the average heat flux error was not > 4.28% (case 2.3, 10 m). Additionally, the maximum midpoint source term error was 3.18% (case 2.1, 5 m), and the average source term error was not > 3.33% (case 2.3, 1 m). Thus, the maximum average error at 5 bar pressure is no more than 6%. Furthermore, the average error was no more than 5% at the pressure of 2 bar, this indicates that the errors change little

Table 3.4 Errors of the new WSGG model in one-dimensional cases

Pressure	2 bar				5 bar				30 bar			
	δq_{wall}	δq_{avg}	$\delta \dot{q}_{\text{half}}$	$\delta \dot{q}_{\text{avg}}$	δq_{wall}	δq_{avg}	$\delta \dot{q}_{\text{half}}$	$\delta \dot{q}_{\text{avg}}$	δq_{wall}	δq_{avg}	$\delta \dot{q}_{\text{half}}$	$\delta \dot{q}_{\text{avg}}$
$L = 1$ m												
Case 1.1	6.70	5.24	4.86	2.38	3.57	1.53	1.05	1.04	2.41	2.26	5.84	2.77
Case 1.2	4.78	3.88	3.63	1.80	4.15	1.14	0.90	1.54	4.18	2.09	5.15	2.51
Case 1.3	4.38	2.65	2.16	1.27	5.05	1.84	2.58	2.48	6.39	2.41	3.16	2.25
Case 1.4	4.29	1.69	1.05	1.23	5.38	2.20	3.41	2.92	7.95	3.18	0.58	1.87
Case 1.5	4.19	1.01	0.04	1.19	5.61	2.47	3.93	3.21	9.68	3.77	4.38	3.23
Case 2.1	4.18	3.28	3.51	1.59	3.18	1.08	0.08	1.87	3.18	1.24	2.27	1.58
Case 2.2	3.88	2.02	1.91	1.18	4.50	2.00	1.87	2.86	5.56	1.67	0.30	1.36
Case 2.3	3.12	0.73	0.83	1.03	4.16	2.46	2.43	3.33	6.60	3.48	3.24	1.85
$L = 5$ m												
Case 1.1	2.73	4.53	6.59	3.14	0.52	1.59	2.60	1.42	9.03	3.08	2.72	2.94
Case 1.2	2.79	3.81	5.43	2.34	2.27	2.13	2.61	1.14	12.49	4.61	2.99	3.39
Case 1.3	2.89	3.82	5.48	2.22	4.37	2.70	2.63	1.14	16.28	6.36	2.03	3.82
Case 1.4	3.30	3.80	5.50	1.99	6.72	3.33	2.50	1.55	20.36	7.88	2.08	4.66
Case 1.5	3.74	3.69	5.14	1.80	8.61	3.96	2.39	1.96	22.62	9.06	4.23	5.62
Case 2.1	2.73	4.32	6.14	2.92	2.07	2.73	3.18	1.63	10.61	4.09	3.46	3.05
Case 2.2	2.90	4.29	6.00	2.68	3.90	3.12	3.04	1.39	15.02	5.99	2.57	3.62
Case 2.3	3.34	4.44	5.97	2.51	5.66	3.67	2.86	1.41	18.19	6.99	2.32	4.20
$L = 10$ m												
Case 1.1	3.73	4.39	5.26	2.40	3.36	1.41	0.46	0.81	15.90	6.38	3.41	4.25
Case 1.2	3.93	3.86	4.34	1.78	6.26	2.30	0.08	1.44	19.69	7.92	2.89	4.74
Case 1.3	4.56	3.44	3.57	1.46	9.94	3.62	0.30	2.26	23.48	9.90	1.37	5.04
Case 1.4	6.11	3.50	3.04	1.48	13.19	5.02	0.35	2.94	27.19	12.50	0.22	5.56
Case 1.5	7.54	3.67	2.56	1.76	14.85	5.90	0.31	3.26	29.43	13.69	0.83	6.07
Case 2.1	3.73	3.85	4.91	1.94	5.04	2.14	1.39	1.19	17.80	6.75	3.16	4.42
Case 2.2	4.25	3.58	4.50	1.76	8.80	3.25	0.99	1.98	22.12	8.91	1.88	4.82
Case 2.3	5.17	3.66	4.54	1.80	11.28	4.28	1.19	2.49	25.37	10.69	1.58	5.37

from 2 to 5 bar. However, on the whole, there are more errors for higher pressure. At a pressure of 30 bar, for homogeneous condition, the maximum of average heat flux error increment was 7.79% (case 1.5, 10 m), and the maximum of average source term error increment was 3.66% (case 1.5, 5 m) when compared with the 5 bar pressure conditions; while for non-homogeneous conditions, the maximum of average heat flux error increment was 6.41% (case 2.3, 10 m), and the maximum of average source term error increment was 3.23% (case 2.1, 10 m). It can be seen that there is not significant increment of the average error, and this indicates that the error

of the new model will increase with the pressure but remains within a certain range; therefore, the new model can ensure the accuracy of calculation.

In addition to the pressure, it can be found in general that the errors would be slightly more for the cases with a higher M; it implies to some extent that the model accuracy is slightly worse when the weighted sum of gray gases method is used to predict the radiation characteristics of the flue gas with a high moisture ratio. In addition, the errors will also increase with the path-length, especially for the heat flux. Table 3.4 also shows that the average errors in the cases with a path-length of 5 m were very low (below 7%), this indicates that the new model has a practical significance since the size of most actual combustion chambers is no more than 5 m [17, 22]. Moreover, it also can be found that the errors of the non-homogeneous conditions were less than that of the homogeneous conditions; therefore, the new model is more suitable for the actual problems with non-homogeneous condition.

Figure 3.6a, b intuitively reflect the new WSGG model results of the homogeneous cases (case 1.2) with $M = 0.5$ under different pressures ($L = 1$ m). Figure 3.6c, d show the new WSGG model results of the homogeneous cases (case 1.2) with $M = 0.5$ for different path-lengths ($P = 5$ bar). Furthermore, the new WSGG model results of the homogeneous cases ($P = 5$ bar, $L = 1$ m) with different molar ratios are shown in Fig. 3.6e, f.

The radiation heat flux curves at different pressures were similar as shown in Fig. 3.6a, b, and increasing pressure can increase the absolute value of the radiation heat flux. When calculating the heat flux and source term in high-pressure conditions, e.g., 2, 5, and 30 bar, the new WSGG model agrees well with the benchmark. Furthermore, the error of the midpoint source term is slightly higher in the 30-bar pressure condition than in the low-pressure conditions. The error results in Table 3.4 show that the new WSGG model has good accuracy under different pressures, and in general, the higher the pressure, the greater the source term errors. Figure 3.6c, d show that the new WSGG model results for different path-lengths of 1, 5, and 10 m are consistent with the benchmark. Furthermore, the wall heat flux error with a path-length of 10 m is slightly greater than that with a path-length of 1 m, indicating that the heat flux error will be greater in general for longer path-lengths. Furthermore, as shown in Table 3.4, the new WSGG model errors for different path-lengths are not large, indicating that the new model is accurate. Figure 3.6e, f show that the new model results agree well with the benchmark for various molar ratios. Furthermore, Table 3.4 shows that the errors will be slightly higher for higher molar ratios. The results shown in Fig. 3.6 and Table 3.4 concluded that the new WSGG model is in good agreement with the reference model for calculating the radiation heat transfer of the flue gas mixture, and that, while different conditions (e.g., pressure, path-length, and molar ratio) will affect model accuracy, the errors are still not very high and within a certain range in general. Thus, the new WSGG model has reasonable accuracy and can be used to calculate the radiation heat transfer of a gas mixture under pressurized conditions.

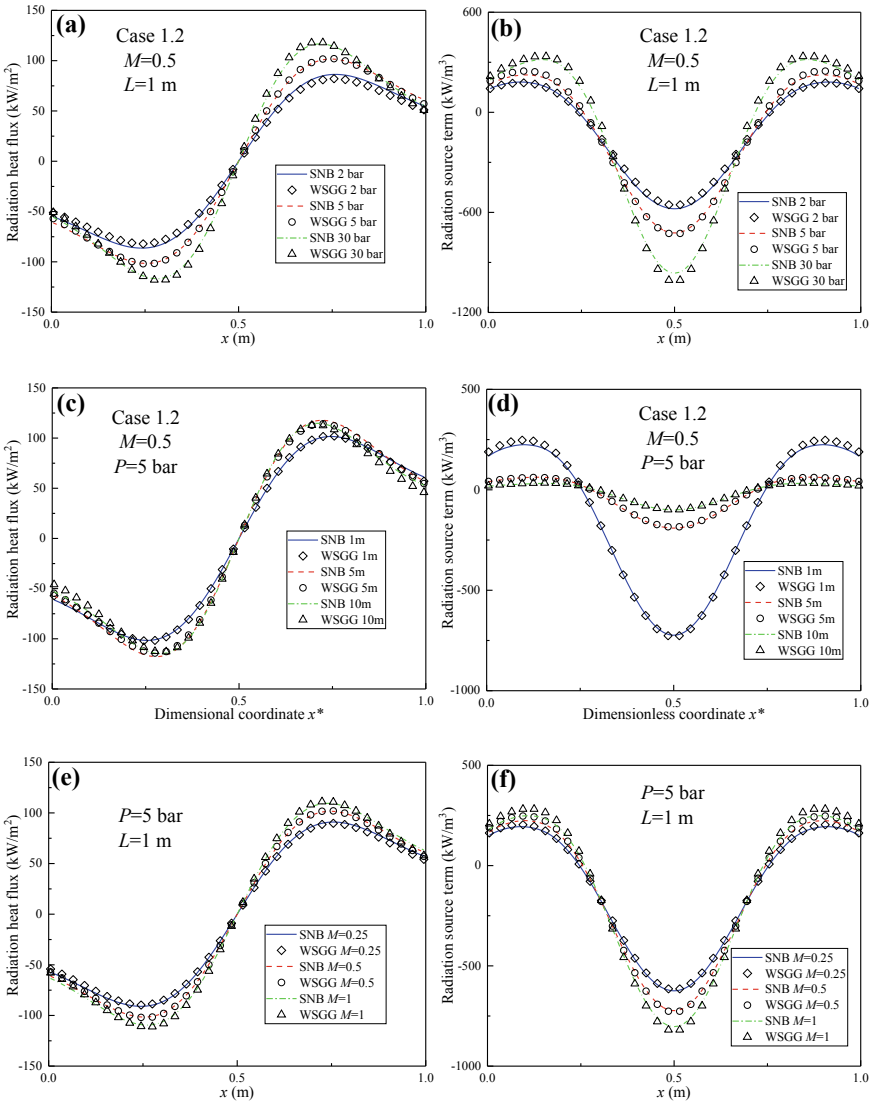

Fig. 3.6 New WSGG model results of homogeneous cases: **a** radiation heat flux and **b** radiation source term under different pressures (case 1.2, $M = 0.5$, $L = 1$ m); **c** radiation heat flux and **d** radiation source term with different path-lengths (case 1.2, MR $= 0.5$, $P = 5$ bar, $x^* = x/L$); **e** radiation heat flux and **f** radiation source term with different molar ratios ($M = 0.25$ for case 1.1, $M = 0.5$ for case 1.2, $M = 1$ for case 1.3, $P = 5$ bar, $L = 1$ m)

3.3.4 *Effect of Pressure on Radiation Heat Transfer*

This section investigates the effect of pressure on the radiation heat transfer of the gas mixture. The isothermal homogeneous cases are discussed in order to investigate the effect of pressure on the radiation heat flux of the gas mixture with various molar ratios, temperatures T, and path-lengths L. The isothermal, homogeneous case is convenient for comparative study since it has explicit characteristic parameters; thus, the isothermal, homogeneous results are of general significance.

The effect of pressure on the average radiation heat flux of a gas mixture with different molar ratios is shown in Fig. 3.7. In this case, the average radiation heat flux is defined as the average value of all the radiation heat fluxes at every grid point along the path-length in a one-dimensional case. In the isothermal, homogeneous cases, five kinds of gas mixtures have different M of 0.25, 0.5, 1, 2 and 4, respectively; the total molar fraction is 0.9; the temperature is 1500 K; and the path-length is 1 m. In the pressure range of 1–30 bar, the effect of pressure on the average radiation heat flux was investigated.

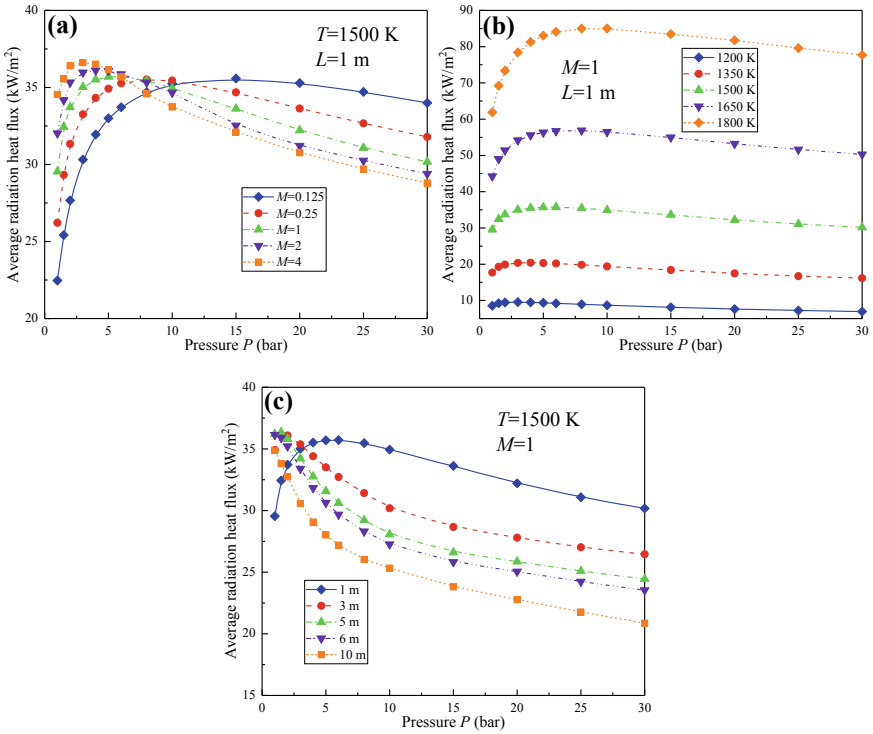

Fig. 3.7 Effect of pressure on the average radiation heat flux of the gas mixtures **a** with different molar ratios, **b** at different temperatures, and **c** with different path-lengths

The average radiation heat flux of the gas mixture increased rapidly at first, then slowly, and finally began to decrease in each case from 1 to 30 bar pressure (Fig. 3.7a). It implies that increasing the pressure in a specific range can improve the radiation heat transfer of the gas mixture. Additionally, the enhancing effect will gradually diminish as the pressure increases. In contrast, the radiation heat transfer is reduced if the pressure exceeds a certain threshold. Thus, an optimal pressure was noted at which the average heat flux of a gas mixture is greatest.

The optimum pressure to improve heat transfer was ~13, ~5, and ~3 bar for the M of 0.25, 1, and 4, respectively (Fig. 3.7a). This means that as the molar ratio of the gas mixture increases, the pressure at which the radiation heat flux begins to decrease is lower. Thus, the optimal pressure for enhancing heat transfer decreases. Increasing the H_2O concentration in the gas mixture results in the best radiation heat transfer enhancement at lower pressure. In practical industrial applications, the optimal pressure will be lower for the fuel with a higher H/C ratio. Thus, the optimal pressure for enhancing the radiation heat transfer of methane combustion will be lower than that of fuel oil combustion. Additionally, the optimal pressure for the radiation heat transfer of wet flue gas cycle oxy-fuel combustion is lower than that of dry flue gas cycle oxy-fuel combustion. Furthermore, Fig. 3.7a shows that if the molar ratio was lower, the variation range of radiation heat flux over the pressure range was larger. This implies that pressure has a greater influence on radiation heat transfer of gas mixtures with a lower M. Thus, pressure has a greater influence on radiation heat transfer of the CO_2 molecule than the H_2O molecule.

All of the curves in Fig. 3.7a roughly intersected at a pressure of about 9 bar, implying that there is a pressure boundary dividing the entire pressure range into two sections. The radiation heat flux of the gas mixture generally increases with the molar ratio when the pressure is below the boundary pressure, and it decreases with the molar ratio when the pressure is greater than the boundary pressure. Thus, increasing the molar ratio of the gas mixture can improve its radiation heat transfer under lower pressure, but decreasing the molar ratio of the gas mixture is required to improve its radiation heat transfer under higher pressure.

The effect of pressure on the average radiation heat flux of the gas mixture at different temperatures is shown in Fig. 3.7b. The five gas mixtures in the isothermal, homogeneous cases have temperatures of 1200, 1350, 1500, 1650, and 1800 K. Additionally, the cases have a molar ratio of 1 and a path-length of 1 m. In the pressure range of 1–30 bar, the effect of pressure on the average radiation heat flux was investigated. The average radiation heat flux of the gas mixture increased first and then decreased with pressure at different temperatures as shown in Fig. 3.7b. Optimal pressure for heat transfer enhancement was noted, as discussed previously in Fig. 3.7a. Moreover, Fig. 3.7b also shows that the optimal pressure was ~2, ~4, and ~8 bar when the temperature was 1200, 1500, and 1800 K, respectively, indicating that the optimal pressure increases with temperature. Furthermore, Fig. 3.7b shows that the higher the temperature is, the more obvious change of the radiation heat flux caused by pressure, which indicates that pressure has a greater effect on the radiation heat transfer of the gas mixture at higher temperatures. Thus, for high-temperature combustion chambers, the pressurization method improves radiation

heat transfer more clearly, and the pressure range to improve radiation heat transfer is wider. Furthermore, Fig. 3.7b shows that the average radiation heat flux is greater at higher temperatures, implying that temperature has a significant influence on the radiation heat transfer of the gas mixture. The radiation intensity is quite high in combustion chambers with high temperatures and pressures, such as those found in rocket engines.

The effect of pressure on the average radiation heat flux of gas mixtures with different path-lengths is shown in Fig. 3.7c. In the isothermal, homogeneous case, the path-lengths of the five gas mixtures are 1, 3, 5, 6, and 10 m. Additionally, the molar ratio of cases is 1 and the temperature is 1500 K. In the pressure range of 1–30 bar, the effect of pressure on the average radiation heat flux was investigated. The variations in average radiation heat flux with pressure for gas mixtures with different path-lengths were different as shown in Fig. 3.7c. For gas mixtures with path-lengths no more than 5 m, the average radiation heat flux increased first and then decreased with pressure. Additionally, when the radiation heat flux began to decrease, the pressure was about 5, 2, and 1.5 bar for the path-lengths of 1, 3, and 5 m, respectively. When the path-length was more than 5 m, the average radiation heat flux of the gas mixture decreased without any initial increase, e.g., the path-lengths of 6 and 10 m, which are shown in Fig. 3.7c. This suggests that the variation of radiation heat transfer of the gas mixture with pressure can be affected by the path-length. In general, for a longer path-length, the optimal pressure for enhancing radiation heat transfer is lower. Nonetheless, the radiation heat flux decreases with pressure and does not undergo any process of first increasing when the path-length exceeds a certain value. Thus, the curves in Fig. 3.7c have no peak, and no *optimum pressure* was noted for the cases with a longer path-length. When evaluating the effect of pressure on radiation heat transfer in practical applications, considering the size of the combustion chambers and the actual path-length in addition to the specific flue gas characteristics is necessary. Furthermore, Fig. 3.7c shows that the variation of radiation heat flux in the pressure range of 1–30 bar is not very different for the gas mixtures with different path-lengths.

The curves in Fig. 3.7c intersected at approximately 3 bar. Thus, a boundary pressure exists that divides the pressure range into two sections, with different trends in the radiation heat flux curves in these two sections. The average radiation heat flux decreased with path-lengths when the pressure was greater than the boundary pressure as shown in Fig. 3.7c. The size of the high-pressure combustion chamber should not be too large to ensure adequate radiation heat transfer intensity.

3.4 Summary

In this chapter, a new WSGG model and its parameters suitable for H_2O/CO_2 mixtures at pressures ranging from 1 to 30 bar were established based on the SNB model. In addition, the new model was used to calculate the emissivity and one-dimensional radiation heat transfer of the gas mixture. The results were also compared with the

benchmark. Finally, the new WSGG model was used to investigate the effect of pressure on the radiation heat transfer of a gas mixture. The following conclusions can be drawn:

(1) The gas mixture emissivity calculated by the new WSGG model is consistent with the benchmark under high-pressure conditions. Additionally, no ideal results were noted for other atmospheric WSGG models. Thus, the development of a new pressurized WSGG model is of great significance.
(2) The results of the new WSGG model in one-dimensional cases are in good agreement with the benchmark. The maximum average heat flux and maximum average source term errors are around 10% and 6%, respectively. According to the most actual pressurized combustion chambers with small size, it can be seen that the average error is no more than 4% for the cases with a path-length of 1 m. Thus, the new WSGG model can provide a reasonably accurate prediction of radiation heat transfer for the gas mixtures under high-pressure conditions and can be used for numerical calculation or design of pressurized combustion chambers.
(3) In a certain pressure range, increasing the pressure can improve H_2O/CO_2 mixture radiation heat transfer. Thus, pressurized oxy-fuel combustion can improve flue gas radiation heat transfer when compared to atmospheric oxy-fuel combustion. Both the emissivity and radiation heat transfer intensity of the oxy-fuel gas mixture increased with pressure. Furthermore, as pressure increases, this effect gradually diminishes; when pressure exceeds this range, the radiation heat flux decreases. Thus, an optimum pressure exists to improve the radiation heat transfer of the gas mixture.
(4) The optimal pressure for radiation heat transfer enhancement can be influenced by the molar ratio of H_2O/CO_2, temperature, and path-length of the gas mixture. The higher the molar ratio is, the lower the optimal pressure will be; nevertheless, the optimum pressure will be higher for a higher temperature; moreover, there is a lower optimum pressure for the longer path-length.
(5) Pressure has a greater effect on the radiation heat transfer of a gas mixture with a lower molar ratio as well as a greater influence on the radiation heat transfer characteristics of CO_2 than H_2O. Thus, an increase in pressure can effectively improve the radiation heat transfer of the dry flue gas recycle condition in oxy-fuel combustion to wet flue gas recycling. Furthermore, pressure has a greater influence on the radiation heat transfer of a gas mixture with a higher temperature. However, the effect of pressure on the radiation heat transfer of gas mixtures with different path-lengths is similar.

References

1. Malkmus W (1967) Random Lorentz band model with exponential-tailed S^{-1} line-intensity distribution function. JOSA 57(3):323–329

2. Soufiani A, Taine J (1997) High temperature gas radiative property parameters of statistical narrow-band model for H_2O, CO_2 and CO, and correlated-K model for H_2O and CO_2. Int J Heat Mass Transf 40(4):987–991
3. Goutiere V, Liu F, Charette A (2000) An assessment of real-gas modelling in 2D enclosures. J Quant Spectrosc Radiat Transfer 64(3):299–326
4. Chu H, Liu F, Zhou H (2011) Calculations of gas thermal radiation transfer in one-dimensional planar enclosure using LBL and SNB models. Int J Heat Mass Transf 54(21–22):4736–4745
5. Rivière P, Soufiani A (2012) Updated band model parameters for H_2O, CO_2, CH_4 and CO radiation at high temperature. Int J Heat Mass Transf 55(13–14):3349–3358
6. Chu H, Gu M, Consalvi J et al (2016) Effects of total pressure on non-grey gas radiation transfer in oxy-fuel combustion using the LBL, SNB, SNBCK, WSGG, and FSCK methods. J Quant Spectrosc Radiat Transfer 172:24–35
7. Hottel H, Sarofim A (1967) Radiative transfer. McGraw-Hill, New York
8. Modest M (1991) The weighted-sum-of-gray-gases model for arbitrary solution methods in radiative transfer
9. Modest M (2013) Radiative heat transfer, 3rd edn. Academic press, Amsterdam
10. Chandrasekhar S (1960) Radiative transfer. Dover Publications, New York
11. Johansson R, Andersson K, Leckner B et al (2010) Models for gaseous radiative heat transfer applied to oxy-fuel conditions in boilers. Int J Heat Mass Transf 53(1–3):220–230
12. Yin C, Johansen L, Rosendahl L et al (2010) New weighted sum of gray gases model applicable to computational fluid dynamics (CFD) modeling of oxy-fuel combustion: derivation, validation, and implementation. Energy Fuels 24(12):6275–6282
13. Kangwanpongpan T, França F, Silva R et al (2012) New correlations for the weighted-sum-of-gray-gases model in oxy-fuel conditions based on HITEMP 2010 database. Int J Heat Mass Transf 55(25–26):7419–7433
14. Rashedul H, Kalam M, Masjuki H et al (2014) Numerical study on convective heat transfer of a spark ignition engine fueled with bioethanol. Int Commun Heat Mass Transfer 58:33–39
15. Arghode V, Gupta A (2010) Effect of flow field for colorless distributed combustion (CDC) for gas turbine combustion. Appl Energy 87(5):1631–1640
16. Zhang J, Dai B, Meng Y et al (2015) Pilot-scale experimental and CFD modeling investigations of oxy-fuel combustion of Victorian brown coal. Fuel 144:111–120
17. Bahramian A, Maleki M, Medi B (2017) CFD modeling of flame structures in a gas turbine combustion reactor: velocity, temperature, and species distribution. Int J Chem Reactor Eng 15(4)
18. Dorigon L, Duciak G, Brittes R et al (2013) WSGG correlations based on HITEMP2010 for computation of thermal radiation in non-isothermal, non-homogeneous H_2O/CO_2 mixtures. Int J Heat Mass Transf 64:863–873
19. Bordbar M, Węcel G, Hyppänen T (2014) A line by line based weighted sum of gray gases model for inhomogeneous CO_2–H_2O mixture in oxy-fired combustion. Combust Flame 161(9):2435–2445
20. Yin C (2016) Effects of moisture release and radiation properties in pulverized fuel combustion: a CFD modelling study. Fuel 165:252–259
21. Gicquel L, Staffelbach G, Poinsot T (2012) Large eddy simulations of gaseous flames in gas turbine combustion chambers. Prog Energy Combust Sci 38(6):782–817
22. Li Y, Han J, Chen X et al (2017) Numerical study of the internal flow field of a dual pulse solid rocket motor including conjugate heat transfer. Proc Inst Mech Eng Part G: J Aerosp Eng 231(8):1535–1549
23. Westbrook C, Pitz W, Herbinet O et al (2009) A comprehensive detailed chemical kinetic reaction mechanism for combustion of n-alkane hydrocarbons from n-octane to n-hexadecane. Combust Flame 156(1):181–199
24. Seshadri K, Frassoldati A, Cuoci A et al (2011) Experimental and kinetic modeling study of combustion of JP-8, its surrogates and components in laminar premixed flows. Combust Theor Model 15(4):569–583

25. Andersson K, Johansson R, Johnsson F et al (2008) Radiation intensity of propane-fired oxy-fuel flames: implications for soot formation. Energy Fuels 22(3):1535–1541
26. Kangwanpongpan T, Silva R, Krautz H (2012) Prediction of oxy-coal combustion through an optimized weighted sum of gray gases model. Energy 41(1):244–251
27. Johansson R, Leckner B, Andersson K et al (2011) Account for variations in the H_2O to CO_2 molar ratio when modelling gaseous radiative heat transfer with the weighted-sum-of-grey-gases model. Combust Flame 158(5):893–901
28. Smith T, Shen Z, Friedman J (1982) Evaluation of coefficients for the weighted sum of gray gases model. J Heat Transfer 104(4):602–608

Chapter 4
Thermodynamic Calculation of Radiative Energy in Combustion Medium

This chapter combines the radiation transfer process with the thermodynamic second law to obtain more accurate results for energy quality and its variability in the spectral radiation transfer process. First, the fundamental concepts of the monochromatic radiative exergy theory are reviewed and discussed. This theory is then combined with the radiation transfer equation, and the spectral radiative entropy and the radiative exergy transfer equations are established and verified using the second law of thermodynamics. Finally, one-dimensional furnace case calculations are performed to determine the spectral distribution and variation of radiative energy and radiative exergy in the combustion medium. Furthermore, the effects of the temperature field, gas molar ratio, and particle number density on spectral radiation characteristics are investigated. This is useful for studies into flame energy spectrum-splitting conversion systems.

4.1 Thermodynamic Theory of Spectral Radiation Transfer in Combustion Medium

4.1.1 Comments on Monochromatic Radiative Exergy Theory

In Chap. 2, a monochromatic spectral radiative exergy theory is developed to characterize the ability of monochromatic radiation to do work; this is a very delicate model. A spectral radiative exergy transfer equation is established in this chapter based on this important idea. The concept of equivalent temperature, which should have the dimension of temperature and is defined to express the quality of energy, is required to describe the available energy of monochromatic radiation. Consequently, an infinite-staged Carnot heat engine model could be established based on

S. Shan et al., *Fundamentals of Thermal Radiation for Energy Utilization in Fuel Combustion*, Advanced Topics in Science and Technology in China 67,
https://doi.org/10.1007/978-981-19-8311-5_4

the concept of equivalent temperature and the differences between the radiative and thermal energy to derive the monochromatic photon exergy as shown in Chap. 2.

The monochromatic photon exergy derived from the infinite-staged Carnot heat engine can be expressed as an integral form:

$$E_\nu = \int_{\nu_0}^{\nu} h\left(1 - \frac{T_0}{T_\nu}\right) d\nu \tag{4.1}$$

T_ν in Eq. (4.1) is considered to be related to the emission temperature and the frequency or the wavelength following the relevant theory. If the equivalent temperature is expressed in terms of wavelength and Eq. (4.1) is integrated to correspond to the macroscopic blackbody radiation exergy as described in Petela's theory, the following equation is obtained:

$$T_\lambda^4 = \frac{fT^3}{\lambda} \tag{4.2}$$

In addition, the corresponding spectral radiative exergy–energy coefficient can be calculated by comparing it with the photon energy:

$$\eta_\lambda = 1 - \frac{4}{3}\frac{T_0}{T_\lambda} + \frac{1}{3}\left(\frac{T_0}{T_\lambda}\right)^4 \tag{4.3}$$

when $T > T_0$: $4.5638 \times 10^{-3} T^3 = \lambda T_\lambda^4$; when $T < T_0$: $5.33 \times 10^{-3} T^3 = \lambda T_\lambda^4$.

Furthermore, the entropy of a monochromatic photon was studied using the infinite-staged Carnot heat engine model, and the entropy of the photon with frequency ν is:

$$S_\nu = \int_0^{\nu} \frac{h d\nu}{T_\nu} \tag{4.4}$$

After substituting Eq. (4.2) into Eq. (4.4), the coefficient of the spectral radiative entropy to the energy can be obtained using a comparison with the photon energy:

$$\xi_\nu = \frac{S_\nu}{h_\nu} = \frac{4}{3T_\lambda} \tag{4.5}$$

Following that, some remarks on the radiative exergy theory are made. First, the Gouy–Stodola theorem was used to demonstrate that the relationship between monochromatic photon exergy and entropy represented by Eqs. (4.1) and (4.4) was proved to be in agreement with:

$$E = H - H_0 - T_0(S - S_0) \tag{4.6}$$

Thus, the proposed entropy and exergy theories are intrinsically harmonious. Furthermore, the new spectral radiative exergy theory focuses on monochromatic radiation's ability to do work, which is greater for shorter wavelength radiation. The radiative exergy in the entire blackbody spectrum corresponds to the blackbody radiative exergy expression proposed by Petela [1].

Second, it is evident that the equivalent temperature [2, 3] is explicitly defined to characterize the spectral radiative energy quality; this is different from the concept of radiation temperature, which is only related to the spectral radiation intensity. Furthermore, the spectral radiative exergy coefficient derived from the infinite-staged Carnot heat engine model differs from the Carnot efficiency, reflecting the differences between the radiation and thermal energy. Thus, the method proposed in Eq. (4.3) appears to be more appropriate for the theoretical characterization of the spectral radiative exergy.

Finally, a special relationship between the monochromatic photons and spectral radiation is investigated from the perspective of radiative exergy. According to the infinite-staged Carnot engine model, for a photon of $h\nu$, $h\nu_0$ is the reference state for calculating its radiative exergy. Furthermore, for blackbody spectral radiation $I_{\mathrm{b},\lambda}$, $I_{\mathrm{b},\lambda}(T_0)$ is the reference state for calculating its radiation exergy [2, 3]. The macro- and microscales should have a corresponding relationship. Consequently, Eqs. (4.1) and (4.2) indicates the following relationship between photons and spectral radiation:

$$\frac{I_{b,\lambda}(T_0)}{I_{b,\lambda}} = \frac{h\nu_0}{h\nu} = \frac{T_0^4}{T_\lambda^4} \tag{4.7}$$

4.1.2 *Spectral Radiative Exergy Transfer*

The following is a spectral radiation transfer equation with emission, absorption, and scattering [4]:

$$\frac{dI_\lambda(\mathbf{s})}{ds} = -\left(\kappa_{a,\lambda} + \kappa_{s,\lambda}\right) I_\lambda(\mathbf{s}) + \kappa_{a,\lambda} I_{b,\lambda} + \frac{\kappa_{s,\lambda}}{4\pi} \int_{4\pi} I_\lambda\left(\mathbf{s}'\right) \Phi\left(\mathbf{s}', \mathbf{s}\right) d\Omega' \tag{4.8}$$

where $\kappa_{a,\lambda}$ is the spectral absorption coefficient, $\kappa_{s,\lambda}$ is the scattering coefficient, and $\Phi(\mathbf{s}', \mathbf{s})$ is the scattering phase function.

The spectral radiative exergy transfer equation can be directly obtained using the spectral radiative exergy theory:

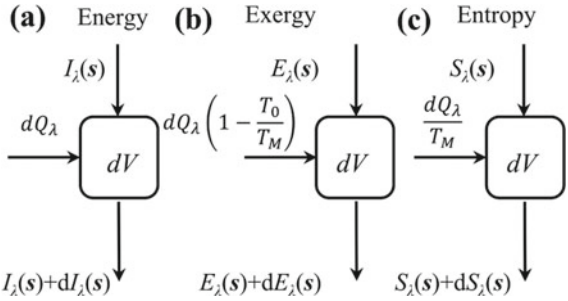

Fig. 4.1 Radiation energy, exergy, and entropy transfer processes

$$\frac{dE_\lambda(\mathbf{s})}{ds} = -(\kappa_{a,\lambda}+\kappa_{s,\lambda})E_\lambda(\mathbf{s}) + \kappa_{a,\lambda}I_{b,\lambda}\left(1-\frac{4}{3}\frac{T_0}{T_\lambda}+\frac{T_0^4}{3T_\lambda^4}\right) + \frac{\kappa_{s,\lambda}}{4\pi}\int_{4\pi}E_\lambda(\mathbf{s}')\Phi(\mathbf{s}',\mathbf{s})d\Omega' \tag{4.9}$$

The first term on the right side of the equation represents the exergy intensity reduction caused by absorption and scattering, the second term is the exergy of the emission, and the third term is the exergy enhancement caused by spatial scattering in the direction of radiation transfer. The spatial propagation of spectral radiative exergy is described in Eq. (4.9). The transfer process for the radiative exergy is very similar to the transfer process for radiative energy shown in Fig. 4.1. The exergy is generated for radiation transfer in a participating medium, and it varies primarily in the radiation field, as well as in the media [3]. Thus, the exergy loss in the participating media radiation transfer consists primarily of the exergy loss in the radiation field and the exergy loss in the media as a result of radiation.

To determine the variation of the radiative exergy in the radiation field, Eq. (4.9) is integrated over the entire solid angle of the space to obtain the local net exergy loss of the radiation with a spectrum interval $d\lambda$ after passing through the differential unit dV.

$$dE_{R,\lambda}^V = -\kappa_{a,\lambda}dVd\lambda\int_{4\pi}\left[E_\lambda(\mathbf{s})-I_{b,\lambda}\left(1-\frac{4}{3}\frac{T_0}{T_\lambda}+\frac{T_0^4}{3T_\lambda^4}\right)\right]d\Omega - \kappa_{s,\lambda}dVd\lambda\int_{4\pi}\left[E_\lambda(\mathbf{s})-\frac{1}{4\pi}\int_{4\pi}E_\lambda(\mathbf{s}')\Phi(\mathbf{s}',\mathbf{s})d\Omega'\right]d\Omega \tag{4.10}$$

Due to the radiation transfer in the participating media, the media also obtain or lose energy through radiation absorption or emission; thus, the exergy of the media varies [3]. As shown in Fig. 5.1b, the local net exergy increment of the media due to the radiation heat flux can be calculated according to the definition of thermal exergy [3]:

$$dE^V_{M,\lambda} = dQ_\lambda\left(1-\frac{T_0}{T_M}\right) = \kappa_{a,\lambda}dVd\lambda\left(1-\frac{T_0}{T_M}\right)\int_{4\pi}\left[I_\lambda(\mathbf{s})-I_{b,\lambda}\right]d\Omega \tag{4.11}$$

Thus, Eqs. (4.10) and (4.11) are combined. After the radiation of wavelength λ passes through a differential unit dV within the spectral interval $d\lambda$, the radiation exergy loss in the entire system is:

$$\begin{aligned} dE^V_{RM,\lambda} &= -dE^V_{R,\lambda} - dE^V_{M,\lambda} \\ &= \kappa_{a,\lambda}dVd\lambda\int_{4\pi}\left[\begin{array}{l} E_\lambda(\mathbf{s}) - I_\lambda(\mathbf{s})\left(1-\dfrac{T_0}{T_M}\right) \\ -I_{b,\lambda}\left(\dfrac{T_0}{T_M}-\dfrac{4}{3}\dfrac{T_0}{T_\lambda}+\dfrac{T_0^4}{3T_\lambda^4}\right)\end{array}\right]d\Omega \\ &\quad + \kappa_{s,\lambda}dVd\lambda\int_{4\pi}\left[E_\lambda(\mathbf{s})-\frac{1}{4\pi}\int_{4\pi}E_\lambda(\mathbf{s}')\Phi(\mathbf{s}',\mathbf{s})d\Omega'\right]d\Omega \end{aligned} \tag{4.12}$$

Because $I_{b,\lambda}\frac{T_0^4}{3T_\lambda^4} = \frac{1}{3}I_{b,\lambda}(T_0)$ according to Eq. (4.7), which is constant for a radiation with wavelength λ in a spectrum of $d\lambda$. That is, its value does not change after passing through a differential unit dV; therefore:

$$dVd\lambda\int_{4\pi}I_{b,\lambda}\frac{T_0^4}{3T_\lambda^4}d\Omega = dVd\lambda\int_{4\pi}\frac{1}{3}I_{b,\lambda}(T_0)d\Omega = 0 \tag{4.13}$$

Therefore, Eq. (4.12) is rewritten as:

$$\begin{aligned} dE^V_{RM,\lambda} &= -dE^V_{R,\lambda} - dE^V_{M,\lambda} \\ &= \kappa_{a,\lambda}dVd\lambda\int_{4\pi}\left[E_\lambda(\mathbf{s}) - I_\lambda(\mathbf{s})\left(1-\frac{T_0}{T_M}\right) - I_{b,\lambda}\left(\frac{T_0}{T_M}-\frac{4}{3}\frac{T_0}{T_\lambda}\right)\right]d\Omega \\ &\quad + \kappa_{s,\lambda}dVd\lambda\int_{4\pi}\left[E_\lambda(\mathbf{s})-\frac{1}{4\pi}\int_{4\pi}E_\lambda(\mathbf{s}')\Phi(\mathbf{s}',\mathbf{s})d\Omega'\right]d\Omega \end{aligned} \tag{4.14}$$

The first term on the right side of the equation is the radiative exergy loss caused by the absorption and emission process and the second term is the exergy loss caused by the scattering process.

4.1.3 Spectral Radiative Entropy Transfer

According to the monochromatic photon entropy expression described in Chap. 2, a spectral radiative entropy transfer equation can be derived by analogy with the spectral radiative exergy transfer Eq. (4.9):

$$\frac{dS_\lambda(\mathbf{s})}{ds} = -\left(\kappa_{a,\lambda}+\kappa_{s,\lambda}\right)S_\lambda(\mathbf{s}) + \kappa_{a,\lambda}\frac{4I_{b,\lambda}}{3T_\lambda} + \frac{\kappa_{s,\lambda}}{4\pi}\int_{4\pi} S_\lambda(\mathbf{s}')\Phi(\mathbf{s}',\mathbf{s})d\Omega' \tag{4.15}$$

The first term on the right side of the equation represents the entropy intensity reduction due to absorption and scattering, the second term is the entropy of the emission, and the third term is the entropy enhancement in the direction of radiation transfer from the spatial scattering. Equation (4.15) reflects the spatial transfer process of radiative entropy. It can be seen in Fig. 4.1 that the transfer process for the radiative entropy is very similar to the radiative energy and exergy transfer processes. Therefore, the entropy generation in the participating media radiation transfer also includes the entropy generation in the radiation field and the entropy generation in the medium caused by the radiation [5, 6].

For the radiative entropy generation in the radiation field, the local net entropy increment of the radiation with the spectrum interval $d\lambda$ after passing through the differential unit dV can be obtained by integrating Eq. (4.15) over the entire solid angle of the space:

$$\begin{aligned} dS^V_{R,\lambda} = &-\kappa_{a,\lambda}dVd\lambda\int_{4\pi}\left[S_\lambda(\mathbf{s}) - \frac{4I_{b,\lambda}}{3T_\lambda}\right]d\Omega \\ &-\kappa_{s,\lambda}dVd\lambda\int_{4\pi}\left[S_\lambda(\mathbf{s}) - \frac{1}{4\pi}\int_{4\pi} S_\lambda(\mathbf{s}')\Phi(\mathbf{s}',\mathbf{s})d\Omega'\right]d\Omega \end{aligned} \tag{4.16}$$

Due to the radiation transfer in the participating media, the media also obtain or lose energy through radiation absorption or emission; thus, the entropy of the media varies [5, 7]. As shown in Fig. 4.1c, the local net entropy increment of the media due to the radiation heat flux can be calculated according to the definition of thermal entropy [5, 7]:

$$dS^V_{M,\lambda} = \frac{dQ_\lambda}{T_M} = \kappa_{a,\lambda}dVd\lambda\int_{4\pi}\frac{I_\lambda(\mathbf{s}) - I_{b,\lambda}}{T_M}d\Omega \tag{4.17}$$

As a result, Eqs. (4.16) and (4.17) are combined. After the radiation of wavelength λ passes through a differential unit dV within the spectral interval $d\lambda$, the radiative entropy generation in the entire system is:

$$dS^V_{RM,\lambda} = dS^V_{R,\lambda} + dS^V_{M,\lambda}$$

$$= -\kappa_{a,\lambda} dV d\lambda \int_{4\pi} \left[S_\lambda(\mathbf{s}) - \frac{4I_{b,\lambda}}{3T_\lambda} - \frac{I_\lambda(\mathbf{s})}{T_M} + \frac{I_{b,\lambda}}{T_M} \right] d\Omega$$
$$- \kappa_{s,\lambda} dV d\lambda \int_{4\pi} \left[S_\lambda(\mathbf{s}) - \frac{1}{4\pi} \int_{4\pi} S_\lambda(\mathbf{s}') \Phi(\mathbf{s}', \mathbf{s}) d\Omega' \right] d\Omega \tag{4.18}$$

The first term on the right side of the equation is the radiative entropy generation caused by the absorption and emission processes and the second term is the entropy generation caused by the scattering process.

The spectral radiative exergy transfer equation (Eq. 4.9), the entropy transfer equation (Eq. 4.15), and the exergy loss or entropy generation in the radiation transfer process can be combined with various radiation transfer numerical calculation methods, such as the discrete ordinate method (DOM), finite volume method (FVM), discrete transfer method, and spherical harmonics method [4]. In this study, some examples are analyzed using the widely applicable DOM.

4.1.4 Thermodynamic Relationship Verification

According to the Gouy–Stodola theorem in Eq. (4.6), the relationship between the radiative entropy and exergy could be verified.

First, for the spectral radiative entropy transfer equation and exergy transfer equation, according to Gouy–Stodola theorem, there is:

$$E_\lambda = I_\lambda - I_{b,\lambda}(T_0) - T_0 \left[S_\lambda - S_{b,\lambda}(T_0) \right] \tag{4.19}$$

and:

$$\frac{dE_\lambda}{ds} = \frac{d\left[I_\lambda - I_{b,\lambda}(T_0) \right]}{ds} - T_0 \frac{d\left[S_\lambda - S_{b,\lambda}(T_0) \right]}{ds} \tag{4.20}$$

After substituting the radiation transfer equation (Eq. 4.8) and the spectral radiative entropy transfer equation (Eq. 4.15) into the right side of the Eq. (4.20), the following is obtained:

$$\begin{aligned}
&\frac{d\left[I_\lambda - I_{b,\lambda}(T_0) \right]}{ds} - T_0 \frac{d\left[S_\lambda - S_{b,\lambda}(T_0) \right]}{ds} \\
&= -\left(\kappa_{a,\lambda} + \kappa_{s,\lambda} \right) \left\{ I_\lambda(\mathbf{s}) - I_{b,\lambda}(T_0) - T_0 \left[S_\lambda(\mathbf{s}) - S_{b,\lambda}(T_0) \right] \right\} \\
&\quad + \kappa_{a,\lambda} \left\{ I_{b,\lambda} - I_{b,\lambda}(T_0) - T_0 \left[\frac{4I_{b,\lambda}}{3T_\lambda} - \frac{4I_{b,\lambda}(T_0)}{3T_0} \right] \right\} \\
&\quad + \frac{\kappa_{s,\lambda}}{4\pi} \int_{4\pi} \left\{ I_\lambda(\mathbf{s}') - I_{b,\lambda}(T_0) - T_0 \left[S_\lambda(\mathbf{s}') - S_{b,\lambda}(T_0) \right] \right\} \Phi(\mathbf{s}', \mathbf{s}) d\Omega'
\end{aligned} \tag{4.21}$$

Consider the second item on the right side of Eq. (4.21):

$$I_{b,\lambda} - I_{b,\lambda}(T_0) - T_0\left[\frac{4I_{b,\lambda}}{3T_\lambda} - \frac{4I_{b,\lambda}(T_0)}{3T_0}\right] = I_{b,\lambda}\left[1 - \frac{4T_0}{3T_\lambda} + \frac{I_{b,\lambda}(T_0)}{3I_{b,\lambda}}\right] \tag{4.22}$$

According to Eq. (4.7), there is:

$$I_{b,\lambda}\left[1 - \frac{4T_0}{3T_\lambda} + \frac{I_{b,\lambda}(T_0)}{3I_{b,\lambda}}\right] = I_{b,\lambda}\left(1 - \frac{4T_0}{3T_\lambda} + \frac{T_0^4}{3T_\lambda^4}\right) \tag{4.23}$$

Therefore, Eq. (4.21) is written as:

$$\begin{aligned}
&\frac{d\left[I_\lambda - I_{b,\lambda}(T_0)\right]}{ds} - T_0\frac{d\left[S_\lambda - S_{b,\lambda}(T_0)\right]}{ds} \\
&= -\left(\kappa_{a,\lambda} + \kappa_{s,\lambda}\right)E_\lambda(\mathbf{s}) + \kappa_{a,\lambda}I_{b,\lambda}\left(1 - \frac{4T_0}{3T_\lambda} + \frac{T_0^4}{3T_\lambda^4}\right) \\
&\quad + \frac{\kappa_{s,\lambda}}{4\pi}\int_{4\pi} E_\lambda\left(\mathbf{s}'\right)\Phi\left(\mathbf{s}', \mathbf{s}\right)d\Omega' \\
&= \frac{dE(\mathbf{s})}{ds}
\end{aligned} \tag{4.24}$$

This corresponds to the Gouy–Stodola theorem defined in Eq. (4.19).

The relationship between the spectral radiative entropy generation and exergy loss according to the Gouy–Stodola theorem is:

$$dE_{RM,\lambda}^V = dI_{R,\lambda}^V + dQ_{M,\lambda}^V - T_0 dS_{RM,\lambda}^V \tag{4.25}$$

Using Eq. (4.8) for the radiative intensity and Eq. (4.18) for entropy and considering Eq. (4.7), the following is obtained:

$$\begin{aligned}
&dI_{R,\lambda}^V + dQ_{M,\lambda}^V - T_0 dS_{RM,\lambda}^V \\
&= -\kappa_{a,\lambda}dVd\lambda\int_{4\pi}\left[I_\lambda(\mathbf{s}) - I_{b,\lambda} - I_\lambda(\mathbf{s}) + I_{b,\lambda}\right]d\Omega \\
&\quad - \kappa_{s,\lambda}dVd\lambda\int_{4\pi}\left[I_\lambda(\mathbf{s}) - \frac{1}{4\pi}\int_{4\pi} I_\lambda\left(\mathbf{s}'\right)\Phi\left(\mathbf{s}', \mathbf{s}\right)d\Omega'\right]d\Omega \\
&\quad - \kappa_{a,\lambda}dVd\lambda\int_{4\pi}\left[T_0 S_\lambda(\mathbf{s}) - I_{b,\lambda}\frac{4T_0}{3T_\lambda} - I_\lambda(\mathbf{s})\frac{T_0}{T_M} + I_{b,\lambda}\frac{T_0}{T_M}\right]d\Omega \\
&\quad - \kappa_{s,\lambda}dVd\lambda\int_{4\pi}\left[T_0 S_\lambda(\mathbf{s}) - \frac{1}{4\pi}\int_{4\pi} T_0 S_\lambda\left(\mathbf{s}'\right)\Phi\left(\mathbf{s}', \mathbf{s}\right)d\Omega'\right]d\Omega
\end{aligned}$$

$$= \kappa_{a,\lambda} dV d\lambda \int_{4\pi} \left[E_\lambda(\mathbf{s}) - I_\lambda(\mathbf{s}) \left(1 - \frac{T_0}{T_M}\right) - I_{b,\lambda} \left(\frac{T_0}{T_M} - \frac{4}{3} \frac{T_0}{T_\lambda} \right) \right] d\Omega$$

$$+ \kappa_{s,\lambda} dV d\lambda \int_{4\pi} \left[E_\lambda(\mathbf{s}) - \frac{1}{4\pi} \int_{4\pi} E_\lambda(\mathbf{s}') \Phi(\mathbf{s}', \mathbf{s}) d\Omega' \right] d\Omega = dE^V_{RM,\lambda} \quad (4.26)$$

It can be seen that the entropy generation and exergy loss in the radiation process agree with the laws of thermodynamics, demonstrating that the entropy generation and the exergy loss are uniform and in internal harmony in the radiation transfer process.

4.1.5 Numerical Verification

The numerical verification method proposed by Liu and Chu [7] was used to validate the new radiative entropy transfer equation. A one-dimensional case is used with equally high temperatures of the two boundary walls; the wall temperatures are set to 3500 K, 2500 K, and 1750 K, respectively. The temperature of the absorbing and emission media is constant at 350 K, the absorption coefficient is set to 0.5, and the length is 1 m. The DOM is used for the calculation and the discrete format is S_8. This method has been applied in the calculation of the one-dimensional radiative heat flux.

By integrating Eq. (4.18) on a one-dimensional space and the whole spectrum, we can obtain the entropy generation of the radiation transfer in a one-dimensional space [7]:

$$\Gamma_G = \int_V \int_\lambda dS^V_{RM,\lambda} d\lambda dV \quad (4.27)$$

In one-dimensional space, the dimensionless entropy generation is defined as [7]:

$$\Pi_G = \frac{\Gamma_G T_L}{Q} \quad (4.28)$$

The numerical results of dimensionless entropy generation in one-dimensional space are depicted in Fig. 4.2. The dimensionless entropy production at different coordinates in the one-dimensional space was stable at 0.9, 0.86, and 0.8 (Fig. 4.2).

However, as demonstrated in [7], the entire system does not output work; thus, the theoretical method can predict entropy generation:

$$\Pi_G = \left(\frac{Q}{T_L} - \frac{Q}{T_H} \right) \frac{T_L}{Q} = 1 - \frac{T_L}{T_H} \quad (4.29)$$

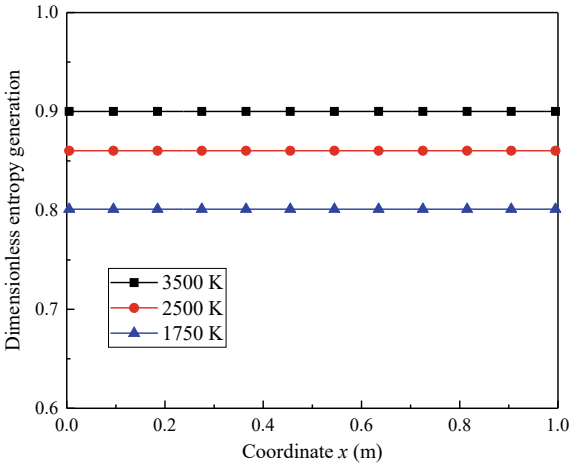

Fig. 4.2 Numerical verification results of dimensionless radiative entropy generation in the one-dimensional case

The results of the theoretical calculation (Eq. 4.29) indicate that the dimensionless entropy generation in the one-dimensional space is 0.9, 0.86, and 0.8 for the wall temperatures of 3500 K, 2500 K, and 1750 K, respectively. A comparison between theoretical results and numerical results in Fig. 4.2 shows that the numerical entropy production in the whole space is very similar to the theoretical results. According to Ref. [7], this approach verifies the new spectral radiative exergy theory and numerical calculation method of the second law calculation for the spectral radiation transfer.

4.2 Radiation Energy Characteristics in Combustion Medium of 1-D Furnace Case

4.2.1 One-Dimensional Cases

Here, the one-dimensional infinite parallel plate cases are used for calculation, which represents the pulverized-coal furnace. Therefore, the one-dimensional radiation media, consists of gas and particle mixture, has the absorption, emission, and scattering properties. The characteristics of radiative energy and radiative exergy are investigated under the conditions with different flue gas temperature, molar ratio, and particle characteristics. Three furnace temperature distribution characteristics are shown in Eq. (4.30), and the corresponding curves are shown in Fig. 4.3.

$$T = 1400 - 400\cos\left(\frac{2\pi x}{L}\right)\ (\mathrm{K}) \tag{4.30a}$$

$$T = 1200 - 300\cos\left(\frac{2\pi x}{L}\right)\ (\mathrm{K}) \tag{4.30b}$$

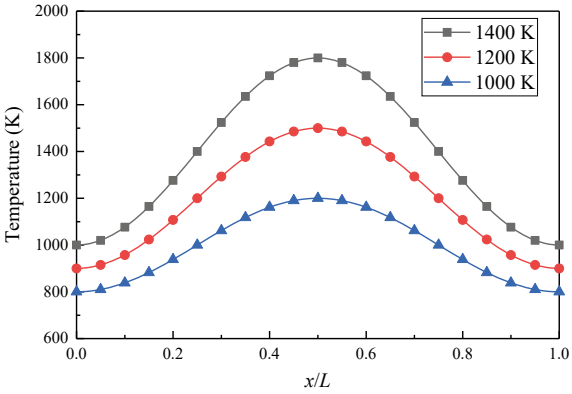

Fig. 4.3 Temperature profiles of the one-dimensional cases

Table 4.1 Molar ratio of different **oxy-fuel** atmospheres

Non-isothermal and homogeneous					
Case	T (K)	X_{H_2O}	X_{CO_2}	M	X
1.1	Equation (4.30a)	0.18	0.72	0.25	0.9
1.2	Equation (4.30a)	0.3	0.6	0.5	0.9
1.3	Equation (4.30a)	0.45	0.45	1	0.9
1.4	Equation (4.30a)	0.6	0.3	2	0.9

$$T = 1000 - 200\cos\left(\frac{2\pi x}{L}\right)\ (\mathrm{K}) \tag{4.30c}$$

Four oxy-fuel atmospheres with different molar ratio are investigated; they are all non-isothermal and homogeneous medium and the molar ratio is shown in Table 4.1.

The absorption and scattering factors for particles need to be calculated from the Mie theory according to the fuel properties. Generally, the average absorption and scattering factors are used, that is, the spectral distribution curve is drawn according to the Mie theory, and then the Planck average is taken. In this book, we do not discuss and perform the specific calculation of Mie theory. Based on the research published results, appropriate radiation characteristic parameters are selected for sensitivity analysis. The particle absorption factor $Q_{\mathrm{abs,coal}}$ of coal is taken as 0.9, the scattering factor $Q_{\mathrm{sca.coal}}$ is taken as 1.1, the absorption factor $Q_{\mathrm{abs,ash}}$ of ash is taken as 1, and the scattering factor $Q_{\mathrm{sca,ash}}$ is taken as 1.5 [8]. The projected area per unit volume of coal, $A_{\mathrm{p,coal}}$, is 0.75 m^{-1}, and the projected area per unit volume of ash, $A_{\mathrm{p,ash}}$, is 0.125 m^{-1} [9]. The calculation methods of the absorption coefficient and the projected area per unit volume are:

$$\kappa = Q_{abs} A_p \tag{4.31a}$$

$$\sigma = Q_{sca} A_p \tag{4.31b}$$

$$A_p = (\pi/4) n d^2 \tag{4.32}$$

where n denotes the particle number density, which remains constant throughout the reaction process:

$$n = \frac{m_{part}}{\rho_{part} V_{part}} / \frac{m_{gas}}{\rho_{gas}} \tag{4.33}$$

Here, V_{part} is the volume of a single particle $4/3\pi(d/2)^3$.

Thus, in this calculation, $\kappa_{\text{coal}} = 0.675$, $\sigma_{\text{coal}} = 0.825$, $\kappa_{\text{ash}} = 0.125$, and $\sigma_{\text{ash}} = 0.1875$. The scattering phase function selects the Henyey-Greenstein distribution:

$$\Phi_{HG}(\phi) = \left(1 - g^2\right) / \left(1 + g^2 - 2g\cos\phi\right)^{3/2} \tag{4.34}$$

According to [9], g is selected as 0.86.

The DOM is used for the radiative exergy transfer calculation. The S_8 discrete format is used for the one-dimensional case, the detail of this method is introduced in Chap. 3. The radiative exergy represented by the transfer Eq. (4.9) is discretely solved at each grid point. The specific process is same as the solution of the one-dimensional RTE. The radiation exergy flux in the radiation field is calculated according to the radiative exergy transfer equation:

$$e = \int_{4\pi} \int_{0}^{\infty} \left(E_\lambda^+(\mathbf{s}) - E_\lambda^-(\mathbf{s})\right) d\lambda d\Omega \tag{4.35}$$

The positive (+) and negative (−) symbols indicate the two directions of transmission, i.e., right and left, respectively; this is similar to the calculation of the radiative heat flux.

According to the blackbody radiation distribution, the majority of the radiation in the high-temperature furnace occurs in the near-infrared region, and the radiation intensity is weak for the wavelength above 50 μm. Thus, the radiation intensity in the 0–50 μm wavelength range is used to represent the total radiation intensity in the calculation. The wavelength interval is 25 nm. The spectral radiative exergy distribution in the 0–50 μm wavelength range is investigated according to the distribution of the spectral radiation intensity of fuel combustion [10, 11].

4.2.2 *Comparison of Different Gas Radiation Models' Applications*

Absorption, emission, and particle scattering states exist simultaneously in gas and particle mixed media. The WSGG model, developed in Chap. 3, and the SNB model are used to calculate the gas radiation properties to obtain the properties of one-dimensional spectral radiation heat flux. The H_2O/CO_2 gas molar ratio M is 0.25 in the calculation, and the total proportion of radiation gas is 0.9; the temperature curve is Eq. (4.30a) with an average temperature of 1400 K, the pressure is 1 bar; additionally, the two sets of absorption coefficient and scattering coefficient of the particles are 0.63 and 0.77 and 1.35 and 1.65, respectively. The SNB model is a spectral band model, which is more accurate in calculating spectral radiative energy, whereas the WSGG model is a global model, which was developed in principle to calculate total heat flux. However, Fig. 4.4 shows that the spectral characteristics of heat flux calculated by the WSGG model are very similar to those calculated by the SNB model. This is because particles with absorption and scattering properties play a significant role in radiation [12]. The radiation properties of the particles are similar to the gray-body radiation, and the calculation uses spectrally averaged absorption and emission coefficients. Thus, under such conditions, the non-gray radiation characteristics of the gas are weakened, and the calculation results of the WSGG model are very similar to those of the SNB model. It also shows that the WSGG model can be used for gas radiation calculation when calculating the spectral radiative properties of combustion media containing particles. Given the computational efficiency of the WSGG model, the results in Sect. 4.2 are all computed using the WSGG model introduced in Chap. 3.

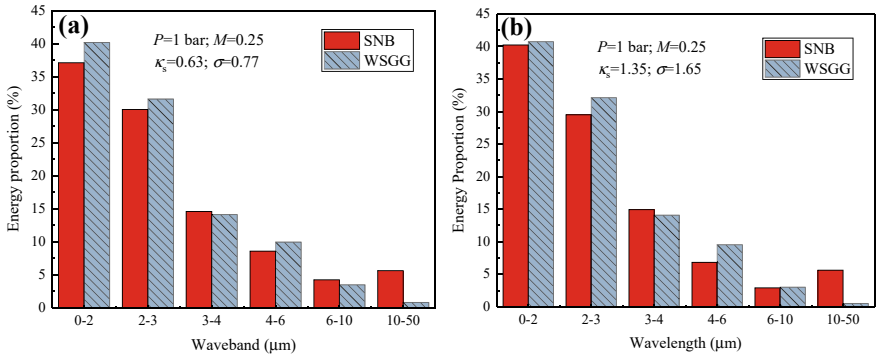

Fig. 4.4 Comparison of spectral radiative energy calculated by WSGG model and SNB model

4.2.3 *Effect of Temperature*

First, the effect of temperature on the medium's radiation characteristics is discussed. The H_2O/CO_2 molar ratio M of the one-dimensional radiation medium is 0.25; the gas pressure is 1 bar; the length of the one-dimensional case is 1 m; the particle radiation characteristics are set according to the parameters in Sect. 4.2.1, and the three different medium temperature distributions are chosen, with average temperatures of 1400, 1200, and 1000 K, respectively as shown in Eq. (4.30). The spectral proportions of radiative and radiative exergy (available energy) of the participating media under different temperature conditions are shown in Fig. 4.5. Consequently, the average radiative heat flux along the path-length is chosen. spectral proportions of radiative energy and radiative exergy are similar. This is because the numerical solution of the entire one-dimensional radiative energy transfer equation is consistent with that of radiative exergy transfer equation, and radiative exergy is derived from the radiative energy. Thus, their spectral proportion characteristics are similar. In computational studies, the proportion characteristics of spectral energy should be mainly investigated. It can also be seen from Fig. 4.5 that as the average temperature increases from 1000 to 1400 K, the spectral proportion of the waveband of 0–2 μm increases significantly, while the energy proportion in the waveband of 1–2 μm increases by 20% points. Overall, the spectral proportion in the waveband above 2 μm decreases with the temperature, where it changes little in the waveband of 2–3 μm, decreases by about 7% in the waveband of 3–4 μm, decreases by about 10% points in the waveband of 4–6 μm, decreases by about 5% points in the waveband of 6–10 μm, and is reduced by about 2% points in the waveband above 10 μm. These findings show that temperature has a significant impact on the proportional properties of radiative energy. High temperature increases the proportion of waveband below 2 μm, that above 2 μm decreases, which is in line with the results of Wayne's displacement law. The peak wavelength shifts to shorter wavelengths. It should be noted that for radiation with wavelengths less than 2 μm, it matches well with semiconductor cells represented by GaSb and can be directly used for photovoltaic conversion. Therefore, increasing the proportion of spectral radiation in the waveband below 2 μm has practical application significance.

The exergy-to-energy ratio of the radiation source term along the path length is shown in Fig. 4.6 for various temperature conditions. The radiation source term was chosen for analyzing the exergy-to-energy ratio because it represents the sum of the energy entering and leaving a specific point along the path-length, which is more comprehensive than the radiative heat flux in a single direction, and thus the exergy-to-energy ratio reflected by radiative source term is more accurate. Figure 4.6 shows that as the average temperature increases from 1000 to 1400 K, the exergy-to-energy ratio increases gradually. At the central location ($x = 0.5$ m), it is 67.5% at an average temperature of 1000 K, and increases to about 79% at 1400 K. These findings indicate that temperature has a significant impact on the radiation exergy-to-energy ratio. The higher temperature means a greater exergy-to-energy ratio, which is

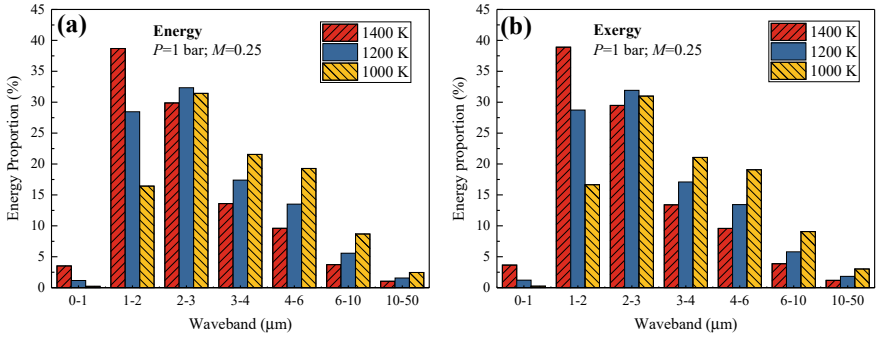

Fig. 4.5 Characteristics of spectral proportion of participating media under different temperature conditions: **a** average radiative energy flux and **b** average radiative exergy flux

consistent with Petela's black-body radiation exergy efficiency Eq. (2.2), so the radiation energy is more valuable. This is mainly related to the increase in the proportion of high-frequency radiation energy. Thus, increasing the temperature of the combustion media is an important technical measure in terms of photovoltaic conversion and radiation energy utilization.

Figure 4.7 further depicts the one-dimensional total radiative energy flux and radiative exergy flux along the path-length. The radiative energy flux and the radiative exergy have a similar trend, which is similar to the previous analysis; i.e., the calculation method of the radiative exergy in the media is similar to that of radiative energy, and the radiative exergy at each point is calculated by the radiative energy. Furthermore, Fig. 4.7 still directly indicates that the radiative energy and radiation exergy increase significantly as the average temperature rises, with the maximum energy flux increasing from 25 kW/m^2 at 1000 K to 150 kW/m^2 at 1400 K, and the maximum exergy flux increasing from about 20 kW/m^2 to about 120 kW/m^2.

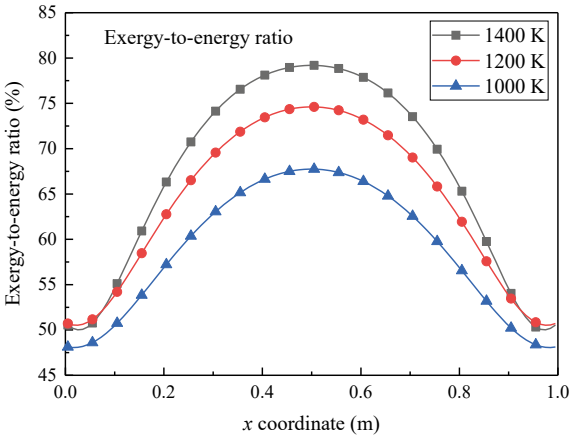

Fig. 4.6 Exergy-to energy ratio of radiation source term along the path-length under different temperature conditions

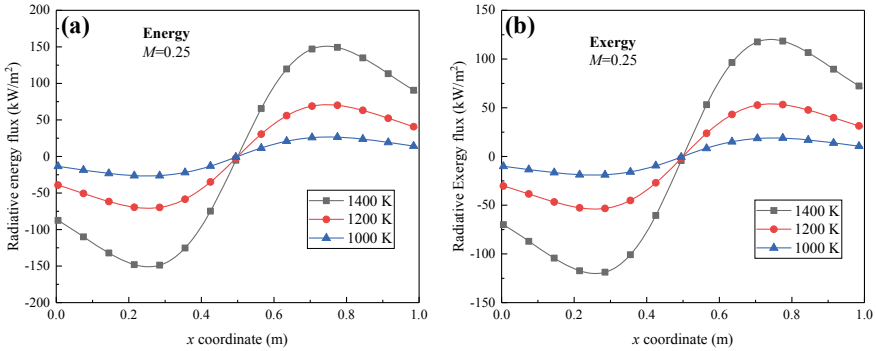

Fig. 4.7 **a** Radiative energy flux and **b** radiation exergy flux along the path length under different temperature conditions

4.2.4 Effect of Gas Molar Ratio

The effect of the gas molar ratio on the radiation properties of participating media is discussed. The average temperature of the one-dimensional radiation media is 1400 K, and the temperature distribution follows Eq. (4.30a), the gas pressure is 1 bar, and the length of the one-dimensional case is 1 m. The particle radiation characteristics are the same as those discussed above, and the H_2O/CO_2 molar ratio M of the media is chosen from the four cases in Table 4.1. Since the spectral characteristics of radiation energy and radiation exergy are almost the same, Fig. 4.8a shows the spectral energy proportion of the radiative media under different molar ratios. The spectral energy proportion is very similar in all four cases. As the molar ratio increases from 0.25 to 2, the proportion of radiation in the waveband below 3 μm decreases slightly, while that in the waveband above 3 μm increases slightly, but the variation does not exceed 1% point, that is, the molar ratio has little effect on the radiation spectral characteristics. In fact, this is because, the proportion of H_2O increases as the molar ratio, and the radiation of H_2O has its special spectrum in the waveband of 5.6–7.6 μm, so the spectral proportion increases in the waveband above 3 μm. However, in the presence of particle media with considerable absorption and scattering coefficients, the particle radiation plays a decisive role in the overall radiation characteristics, and the effect of individual gas radiation is less. Thus, gas molar ratio variation has little effect on the radiation spectrum characteristics.

Figure 4.8b depicts the effect of the molar ratio on the average radiative energy flux and radiative exergy flux. When it increases from 0.25 to 2, the average radiative energy flux increases from 112 to 118.7 kW/m^2. This is because the increase in the proportion of H_2O helps to improve the radiative heat transfer. Thus, the corresponding average radiative exergy also increases from 89.2 to 94.4 kW/m^2. In addition, the total exergy-to-energy ratio shows a downward trend in the range of 79.7–79.5%, which can be regarded as almost no variation. The effect of molar ratio on exergy-to-energy ratio can be ignored in the presence of particle radiation.

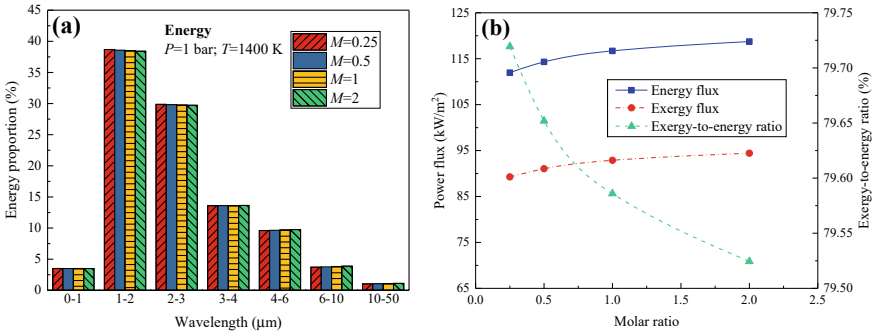

Fig. 4.8 **a** Spectral proportion characteristics of media radiation under different molar ratios; **b** the influence of molar ratio on average radiative energy flux and radiative exergy flux

4.2.5 Effect of Particle Number Density

In order to consider the influence of particle characteristics, the coal particle diameter is selected as 100 μm and the ash particle diameter is 30 μm. In the previous calculation, $A_{p,\mathrm{coal}} = 0.75$ and $A_{p,\mathrm{ash}} = 0.125$ were selected following Eq. (4.33); the ratio of particle number density of coal and ash is $n_{\mathrm{coal}}/n_{\mathrm{ash}} = 0.54$, and the proportion of coal particles number is 35%. Assuming that the total number of coal and ash particles remains constant, the radiation characteristics of participating media are investigated when the coal particle number ratio r varies from 20 to 60%. The burnout area in the combustion chamber is represented by a smaller proportion of coal particles, while the combustion area is represented by a larger proportion, and the larger the proportion, the closer it is to the combustion center.

Figure 4.9a depicts the spectral radiation characteristics of participating media as the coal particle concentrations vary. The spectral radiation characteristics are still consistent. When the proportion of coal particle increases from 20 to 60%, the proportion of spectral radiation in each waveband changes less. This is because although there are variations in the absorption and scattering coefficients of coal and ash particles after the number density of coal particles changes, the average absorption and scattering coefficients are used in the calculation, while the spectral coefficients are not used. The radiation characteristics are less affected by the average radiation parameters. However, it can still conclude that when the spectral radiation parameters of the particles are relatively stable, the particle number density has little effect on the spectral radiation characteristics of the participating media.

The effect of coal particle concentration on the average radiative energy flux and radiative exergy flux is further reflected in Fig. 4.9b. The average radiative energy flux decreases from 99.6 to 121.2 kW/m^2 as the coal particle concentration increases from 20 to 60%, indicating that the radiative heat transfer is greater when the coal particle concentration is high, i.e., the closer to the combustion flame center, the greater the radiative heat transfer. The corresponding average radiative exergy also increases from 79.5 to 96.6 kW/m^2. Furthermore, the radiative energy-to-energy ratio

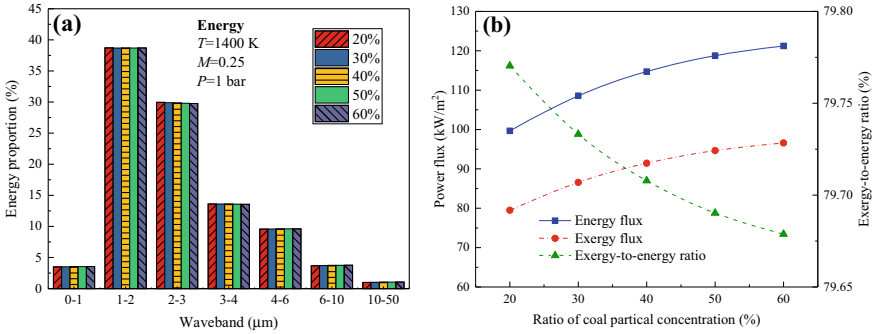

Fig. 4.9 **a** Spectral proportion characteristics of media radiation under different coal particle concentrations; **b** influence of coal particle concentration on average radiative energy flux and radiative exergy flux

flow is almost stable at about 79.7%. These results indicate that under the combustion conditions of solid fuels such as pulverized coal, the radiation heat transfer is greater if the participating media is closer to the center of the combustion area, while the proportion of ash particles is greater if the media is farther from the combustion center, and the radiation intensity is smaller. If the combustion temperature is similar, the change of various parameters has little effect on the radiative exergy-to-energy ratio of the participating media. Elevating the temperature is the preferred solution to the radiative exergy in combustion media.

4.3 Summary

This chapter combines the radiation transfer equation with the theory of the monochromatic photon exergy developed in Chap. 2 by considering the second law of thermodynamics. Based on the second law, the spectral radiative entropy transfer equation and radiative exergy transfer equation are established; this process can be used to numerically analyze the variability of the energy quality during the spectral radiation transfer process more appropriately and accurately. The radiative entropy and the radiative exergy are found to be consistent with the thermodynamic Gouy–Stodola law.

Numerical calculations of the spectral radiative exergy transfer equation can be used to determine the distribution and variation of the radiation spectral exergy flux during the radiation transfer process. Calculating the spectral radiative exergy distribution, which is very important for the analysis of the flame energy spectrum-splitting conversion system in high-temperature engineering, is also possible. The results of the one-dimensional cases simulating the furnace temperature field show that the proportion characteristics of spectral radiative energy and spectral radiative exergy are consistent, implying that the proportion characteristics of spectral energy can be

used to predict those of spectral radiative exergy. Temperature is the primary factor influencing spectral radiative energy. A higher temperature indicates that the proportion of radiative energy in the waveband of < 2 μm is greater, and more available radiative energy exists. At the same temperature, the combustion atmosphere and coal particle concentrations have little effect on the proportional characteristics of spectral radiative energy. These parameters will influence the radiative energy characteristics in the actual combustion process by influencing the combustion temperature. Thus, additional experiments are required to investigate the characteristics of spectral radiative energy.

References

1. Petela R (1964) Exergy of heat radiation. J Heat Transfer 86(2):187–192
2. Candau Y (2003) On the exergy of radiation. Sol Energy 75(3):241–247
3. Liu L, Chu S (2007) Radiative exergy transfer equation. J Thermophys Heat Transfer 21(4):819–822
4. Modest M (2013) Radiative heat transfer, 3rd edn. Academic Press, Amsterdam
5. Caldas M, Semiao V (2005) Entropy generation through radiative transfer in participating media: analysis and numerical computation. J Quant Spectrosc Radiat Transfer 96(3–4):423–437
6. Caldas M, Semião V (2007) The effect of turbulence–radiation interaction on radiative entropy generation and heat transfer. J Quant Spectrosc Radiat Transfer 104(1):12–23
7. Liu LH, Chu SX (2007) Verification of numerical simulation method for entropy generation of radiation heat transfer in semitransparent medium. J Quantit Spectrosc Radiat Trans 103(1):43–56
8. Gronarz T, Schulze J, Laemmerhold M et al (2017) Quantification of the influence of parameters determining radiative heat transfer in an oxy-fuel operated boiler. Fuel Process Technol 157:76–89
9. Kez V, Consalvi J, Liu F et al (2019) Investigation of gas and particle radiation modelling in wet oxy-coal combustion atmospheres. Int J Heat Mass Transf 133:1026–1040
10. Becher V, Goanta A, Spliethoff H (2012) Validation of spectral gas radiation models under oxyfuel conditions–part C: validation of simplified models. Int J Greenhouse Gas Control 11:34–51
11. Kirdyashkin A, Orlovskii V, Sosnin E et al (2010) Energy and spectral characteristics of radiation during filtration combustion of natural gas. Combust Explosion Shock Waves 46(5):523–527
12. Johansson R, Leckner B, Andersson K et al (2013) Influence of particle and gas radiation in oxy-fuel combustion. Int J Heat Mass Transf 65:143–152

Chapter 5
Radiative Energy Characteristics of Solid Fuel Combustion

In order to understand the radiative energy characteristics of solid fuel combustion, further experimental results are introduced in this chapter. A few studies currently exist on the radiative characteristics of fuel combustion for energy utilization. Thus, this chapter introduces the spectral radiative characteristics of solid fuel combustion to provide a foundation for radiative energy utilization. The radiative energy characteristics of oxy-fuel combustion of various solid fuels, including pulverized coal and semi-coke, are experimentally investigated using a modified tube furnace test platform and a self-built Hencken flat-flame burner. It focused on the effects of various fuels, temperature, atmosphere, and oxygen concentration on radiation energy and its spectral distribution. The characteristics of radiation exergy and its spectral distribution are also investigated based on the radiation thermodynamics theory proposed in Chap. 2. Through experiments and analysis, the preliminary results obtained in this chapter are helpful to understand the characteristics of combustion radiative energy and master its control methods, which can provide a reference for future studies and design of cascade conversion of photo-thermal energy in fuel combustion.

Revised from Shan et al., Spectral energy characteristics of radiation in oxy-coal combustion for energy utilization, Fuel, Copyright (2021), with permission from Elsevier.

Revised from Shan et al., Spectral radiation characteristics in semi-coke jet flame for energy utilization, Fuel, Copyright (2021), with permission from Elsevier.

S. Shan et al., *Fundamentals of Thermal Radiation for Energy Utilization in Fuel Combustion*, Advanced Topics in Science and Technology in China 67,
https://doi.org/10.1007/978-981-19-8311-5_5

5.1 Multi-scale experiments

5.1.1 Tube Furnace Experiments

5.1.1.1 Experimental System

A tube furnace platform is constructed for the solid fuel combustion experiment. Figure 5.1 shows the experimental system, which is similar to that used in a previous study [1]. The tube furnace was 60 cm long. A high-temperature-resistant quartz tube (140 cm long and 6.5 cm in diameter) was used, with one side of the tube opened for measurement. Furthermore, the sample was placed at the center of the quartz tube, and a radiation sensor was placed 97 cm from the sample. In the experiment, a CT-20 high-temperature radiation sensor (Captec Co., France) was used to measure the radiative heat flux at the outlet of the quartz tube. The sensor can measure the total radiation power in the 0.3–50 μm spectrum band and has a response time of 0.25 s. The experimental data were recorded using a Daq-5300 eight-channel data logger (Fourier System Co., Israel), with an acquisition interval of 1 s. An infrared filter (Spectrogon Co., Sweden), a standard shortwave pass filter that allows for the passage of short-wavelength radiation, was placed in front of the radiation sensor to separate the radiation spectrum. The specific cutoff band λ_c and transmittance τ of the different filters are $\lambda_c = 1125 \pm 25$ nm, $\tau = 94.98\%$ (filter no. 1); $\lambda_c = 4100 \pm 100$ nm, $\tau = 89.29\%$ (filter no. 2); and $\lambda_c = 10500 \pm 200$ nm, $\tau = 76.6\%$ (filter no. 3). Although the separation method using a filter is relatively unrefined, it could still provide a preliminary reference based on the experimental conditions [2].

5.1.1.2 Experimental Method and Data Analysis

The experiment used two Chinese coals with different coal ranks: Ximeng lignite (XM) and Shenhua bituminous coal (SH). The particle size of the coal samples ranged from 75 to 150 μm and were dried in a 105 °C oven for 2 h. Table 5.1 presents the proximate and ultimate analyses.

In the experiment, the furnace was heated to the desired temperature, and the reaction atmosphere was then passed through the tube at 1.5 ± 0.01 L/min for 30 min to ensure the experimental atmosphere in the tube. An empty crucible was then quickly pushed into the center of the reaction zone, and the data were subsequently recorded as a calibration set. After calibration, a similar process was performed for the crucible with a coal sample weighing 0.8 ± 0.005 g and evenly placed on the bottom of the crucible. The crucible was specially designed to conduct better radiation measurements (Fig. 5.1). Similar experiments were conducted for each filter. The radiative heat flux was represented by the difference between the experimental and calibration results. The experiment was conducted in a dark laboratory to minimize the effect of the environment as much as possible.

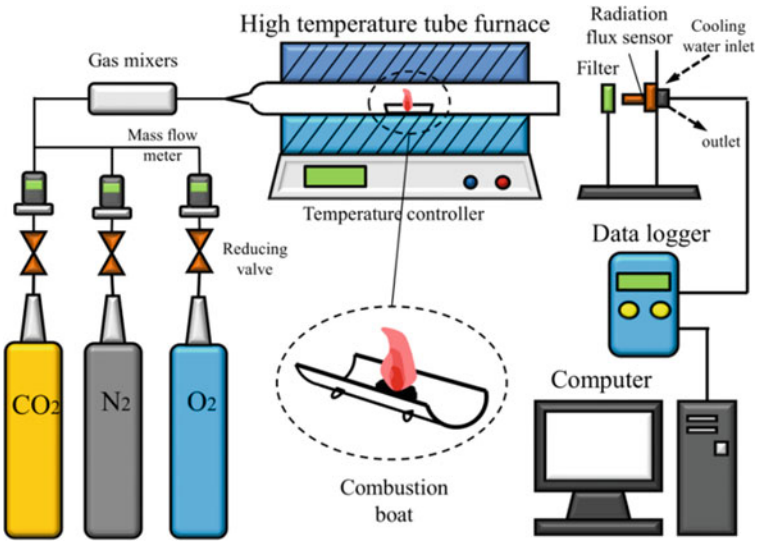

Fig. 5.1 Schematic diagram of the experimental setup

In the experiment, oxygen ratios of 21–60% for the O_2/CO_2 atmosphere at 800 °C and a temperature range of 600–1000 °C in a 30% O_2/CO_2 atmosphere were investigated. These conditions are chosen because a 30% O_2/CO_2 atmosphere is often used as an alternative air-combustion condition [3]. Moreover, the selection of temperature range mainly considers the temperature of the furnace flue gas for oxy-fuel boiler is mainly around 1000 °C [4]. Therefore, this is still meaningful to the study of oxy-fuel combustion characterized by flue gas radiation. In this study, the control variable method is used to achieve the general significance of the comparison between different conditions, and it has been discovered that the radiation flux changes in a tube furnace [1]. To provide a reference for an actual combustion furnace, the average value of the estimated radiation flux during the period from 80 to 140 s was used, as the radiation flux variation was relatively stable in this stage.

The instrument uncertainty (3%) of the radiation sensor is considered when evaluating the uncertainty factors; thus, the measured value is multiplied by 3% as the instrument error δ_1. In addition, the standard deviation δ_2 is used to represent the degree of fluctuation in the experimental data because the data is investigated over a 1-min period. Furthermore, the instrument uncertainty δ_1 and statistical uncertainty δ_2 are used to calculate the synthetic uncertainty $\delta = \sqrt{\left(\delta_1^2 + \delta_2^2\right)}$ [2], which is shown in the figures displaying the radiative heat flux results.

To characterize the available energy of radiation, the concept of radiative exergy must be introduced. Therefore, the experimental data are analyzed using radiation thermodynamics to obtain radiative exergy data in oxy-fuel combustion, serving as a reference for combustion energy cascade conversion systems. The spectral radiative exergy is calculated using the radiative exergy-to-energy ratio equation proposed in

Table 5.1 Proximate and ultimate analysis of experimental coals

	Proximate analysis				Ultimate analysis					$Q_{net,ad}$ (kJ/kg)
	M_{ad} %	A_{ad} %	V_{ad} %	FC_{ad} %	C_{ad} %	H_{ad} %	N_{ad} %	S_{ad} %	O_{ad} %	
Bituminous	8.59	4.54	29.21	57.66	69.85	3.50	0.71	0.43	12.38	27,168
Lignite	20.20	14.01	31.20	34.59	45.69	2.84	0.63	0.75	15.88	17,754

Note ad air dry basis. Q_{net} net calorific value

Chap. 2:

$$\eta_\lambda = 1 - \frac{4}{3}\frac{T_0}{T_\lambda} + \frac{1}{3}\left(\frac{T_0}{T_\lambda}\right)^4 \tag{5.1}$$

where T_λ denotes the equivalent temperature and can be used to characterize radiation exergy. Spectral radiation energies with different frequencies have different exergies, so T_λ is related to the wavelength and the radiation temperature. It is expressed as

$$T_\lambda^4 = \frac{fT^3}{\lambda} \tag{5.2}$$

Here, when $T > T_0$, $4.5638 \times 10^{-3} T^3 = \lambda T_\lambda^4$; when $T < T_0$, $5.33 \times 10^{-3} T^3 = \lambda T_\lambda^4$.

In the experiment, radiative energy is divided into four different wavebands through the three filters. When Eq. (5.1) is used to calculate the radiative exergy for each waveband, a black-body equivalent wavelength λ_m is designed, and its equivalent temperature is $T_{\lambda m}$ at a certain temperature (Eq. 5.2). The exergy efficiency expressed by $T_{\lambda m}$ (Eq. 5.1) can be used to calculate the blackbody radiative exergy $E_{\lambda 1-\lambda 2}(T)$ in the wavelength range of $\lambda_1 - \lambda_2$:

$$E_{\lambda_1-\lambda_2}(T) = L_{\lambda_1-\lambda_2}(T) \times \left[1 - \frac{4}{3}\frac{T_0}{T_{\lambda m}} + \frac{1}{3}\left(\frac{T_0}{T_{\lambda m}}\right)^4\right] \tag{5.3}$$

where $L_{\lambda 1-\lambda 2}(T)$ denotes the blackbody radiation flux in this spectral waveband and λ_m ranges between λ_1 and λ_2. After obtaining the values of λ_m for the four wavebands of 0.3–1.125, 1.125–4.1, 4.1–10.5, and 10.5–50 μm, Eq. (5.3) is used to calculate the radiative exergy flux in each waveband based on the experimental radiation flux, and the total radiative exergy flux is the sum of all fluxes.

5.1.2 The Small Hencken Flat-Flame Burner Experiment

5.1.2.1 Experimental System

In the laboratory of the current study, a Hencken flat-flame burner for diffusion combustion was built based on the design in [5, 6]. The flat-flame burner uses gas fuel combustion to produce flue gas with a specific composition and temperature to support solid fuel combustion. The particle jet is ignited using the high-temperature flue gas produced by gas fuel combustion and the particle heating rate under this experimental condition are similar to that of actual furnace [6]. The detailed description of the Hencken flat-flame burner is contained in Sect. 5.1.2.2. Moreover, Fig. 5.2 shows the experiment system, which mainly includes a Hencken burner, a powder-feeding device, a gas-supplying subsystem, and an optical measurement subsystem.

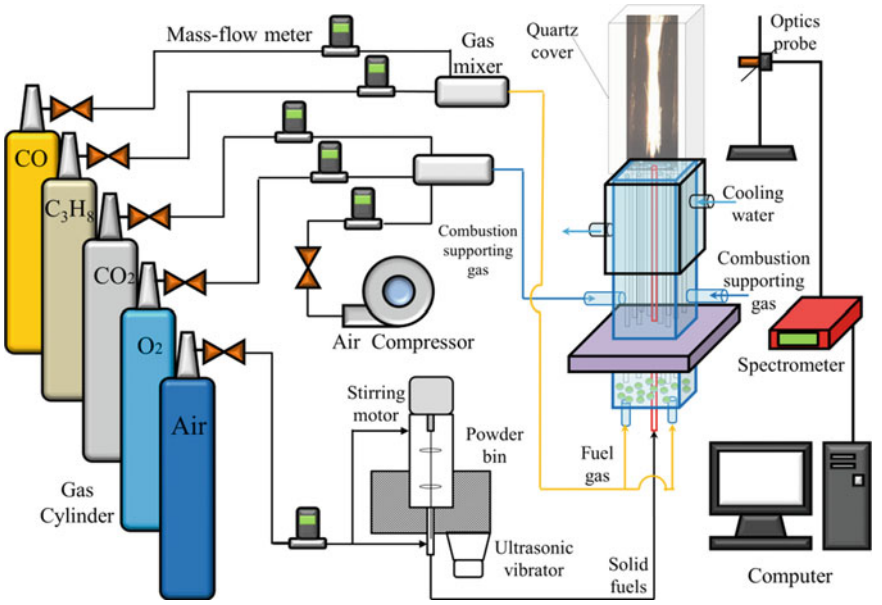

Fig. 5.2 Diagram of the experimental system based on Hencken flat-flame burner

Under the effect of the ultrasonic vibrator and the stirring motor, the pulverized fuel is carried by air from the powder bin through the stainless-steel tube to the central burner outlet, which is surrounded by gas outlets of carbon monoxide/propane evenly. The high-temperature flue gas produced by gas combustion provides required temperature and atmosphere for the combustion of solid fuel.

All experimental gases are controlled by mass-flow meters (Alicat Co.). The fuel gas and combustion-supporting atmosphere are mixed by the gas mixer and then enters the burner. Moreover, the AvaSpec-ULS2048XL spectrometer is used to obtain the radiation spectrum of the target flame with a wavelength range of 200−1160 nm (spectral resolution is 2.4 nm), and the diameter of receiving area is 1 mm for the fiber probe. The spectrometer is calibrated by the standard blackbody furnace signal before this experiment, so it can be used directly to obtain the radiation spectrum. To facilitate spectrum measurement at different heights, the optical fiber probe is connected to a collimator and fixed on the optical bracket, which is fixed on the slide rail. The test platform is also calibrated to maintain its horizontal position, and the experiment is conducted in a dark room to avoid interference from other visible light. Before data collection, the probe position must be adjusted using laser alignment to determine the flame center position. Continuous monitoring is conducted when the flame is stable, and 50 consecutive sets of spectral data are chosen for averaging to obtain the results. To achieve real-time spectral data processing, the probe is linked to the computer via optical fiber. The signals at 7, 10, 14, 17, and 20 cm from the burner outlet are measured in the experiment. Because the measuring points are at

actual height, the measured results can represent the radiation intensity in the same radiation area, which is better for comparing different cases.

5.1.2.2 Description of Small Flat-Flame Burner Facility

The Hencken burner can generate a thin-plane flame (2–3 mm) for gas combustion and is also flexible for adjusting the flue gas composition and temperature. Furthermore, it is more suitable for optical measurement because of the absence of the need for electric or other heating devices.

The cross-sectional size of the self-built Hencken burner is about 55 × 55 mm (Fig. 5.2), and it can form a gas flame plane with a corresponding area. The burner is primarily made of upper and lower chambers. The lower chamber has a height of about 100 mm for fuel gas, while the upper chamber has a height of about 200 mm for combustion-supporting gas. The upper and lower chambers are separated by heat-resistant silica-gel plates. Two holes were noted at the bottom of the lower chamber for the gas introduction. The gas fuel in the experiment is carbon monoxide. The upper space of the gas inlets is filled with color-changing colloidal silica for adjusting and drying the gas flow. In the upper chamber, 652 stainless-steel capillary tubes serve as fuel channels, penetrating the silicone plate into the lower chamber to deliver fuel gas to the burner outlet. Two symmetrically designed holes were noted in the lower part of the upper chamber to input combustion-supporting gas (e.g., air), which enters the upper chamber and flows outside the capillary tubes until merging with the fuel gas at the burner outlet. The water-cooling groove is located on the periphery of the upper chamber, and a thicker powder-feeding tube (outer diameter, 3 mm; inner diameter, 2.5 mm; and total length, about 330 mm) is installed through the entire central section of the burner. A quartz glass tube is placed as a protective cover in the upper space of the burner outlet to prevent the flue gas temperature from dropping too quickly and to suppress the influence of external factors during the experiment.

Furthermore, the Hencken burner powder-feeding device consists primarily of a powder bin, a stepping motor, and an ultrasonic vibrator with a controller. The solid fuel is carried to the inlet of the powder-feeding tube at the bottom of the burner by adjusting the carrier air. A small amount of propane is added with a flow rate of 20 mL/min (SCCM) because the gas fuel CO is difficult to burn consistently at high gas flow rates.

5.1.2.3 Experimental Method and Data Analysis

The hot flue gas produced by gas combustion in the flat-flame burner can provide the temperature and atmosphere for solid fuel combustion. The atmosphere produced by gas combustion is referred to as secondary airflow. The flow rate of each gas entering the burner is reversely deduced based on secondary air conditions to obtain the designed experimental conditions of the secondary airflow (temperature, oxygen ratio, and gas flow rate). The appropriate method is as follows:

Since the main fuel gas in this study is CO and the atmosphere is assumed to be O_2/N_2, the following reaction equation was used to calculate the adiabatic flame temperature

$$aCO + bO_2 + cN_2 = aCO_2 + (b - a/2)O_2 + cN_2 \tag{5.4}$$

where a, b, and c are the flow rates of CO, O_2, and N_2, respectively, in L/min (SLM). According to the reaction in Eq. (5.4), if the flow rates of each reactant are known, the adiabatic flame temperature T_{ad} can be calculated by referring to the specific heat capacity, enthalpy, and temperature of gases. Furthermore, the conservation of material mass before and after the reaction can be demonstrated as follows:

$$(a + b + c)\rho_{T_0} = VS\rho_{T_{ad}} \tag{5.5}$$

where ρ is the density of the mixed gas, in kg/m^3; V is the gas velocity on the burner section, in m/s; S is the effective area of the burner outlet and can be estimated by $S = 0.8D^2$, where $D = 55$ mm and is the side length of the outlet section. Using the ideal state equation $Pm = N\rho RT$ and the conservation equation, the gas velocity can be calculated as follows:

$$V = \frac{(a/2 + b + c)T_{ad}}{ST_0} \tag{5.6}$$

The oxygen ratio in the secondary air atmosphere is

$$Y_{O_2} = \frac{b - a/2}{a/2 + b + c} \times 100\% \tag{5.7}$$

The experimental cases have different secondary airflow requirements (temperature, oxygen ratio, and flow rate), and the theoretical flow rate of each supplying gas can be calculated using Eqs. (5.4)–(5.7). In this study, two secondary air atmospheres, O_2/CO_2 and O_2/N_2, are required; thus, O_2 was mixed with air or CO_2 to adjust the atmosphere (Table 5.2). The flue gas flow rate is set to 1.5 m/s.

This study uses semi-coke made from Datong bituminous coal on a drop tube furnace. The pyrolysis temperature is 1200 °C, and the atmosphere is N_2. The semi-coke with a particle size of 58–96 μm is chosen and dried at 105 °C for 2 h. The particle size range is chosen similarly to that in [5], which is the same as the size of the pulverized solid fuel in an industrial power plant. The proximate and ultimate analysis of the semi-coke from Datong coal is shown in Table 5.3. The amount of solid fuel is primarily determined by the carrier gas flow, stepper motor speed, and vibrator power. In this study, the carrier gas flow, the stepper motor speed, and the ultrasonic vibrator power is set to 0.36 L/min, 60 rpm, and 35 W, respectively, resulting in a calibrated feeding rate of ~ 8.2 g/h. The secondary airflow was adjusted first during the experiment, and powder-feeding started after the gas flame was stable.

Table 5.2 Experimental cases of the flat-flame burner

Case	Setting flue gas temperature (°C)	Setting atmosphere	Air flow rate (L/min)	CO_2 flow rate (L/min)	O_2 flow rate (L/min)	CO flow rate (L/min)
1	1200	21% O_2/N_2	35.78	–	5.01	6.54
2	1400	21% O_2/N_2	29.96	–	5.34	6.98
3	1400	21% O_2/CO_2	–	21.19	12.87	9.45
4	1400	30% O_2/CO_2	–	18.03	16.20	9.13

Table 5.3 Proximate and ultimate analysis of the semi-coke from bituminous coal

Proximate analysis %			Calorific value Q_{net} (MJ/kg)	Ultimate analysis %				
A_{ad}	V_{ad}	FC_{ad}		C_{ad}	H_{ad}	O_{ad}	N_{ad}	$S_{t,ad}$
9.47	5.76	84.77	28.71	85.04	0.19	4.51	0.16	0.63

Note ad air dry basis; Q_{net} net calorific value

The radiation spectrum was collected by spectrometer after the solid fuel flame was stable.

The best method for measuring the temperature of the solid fuel flame is spectroscopy. When compared with contact measurement, this spectroscopy method does not disturb the flame shape, which prevents the experimental results from being influenced. According to the spectral signal directly measured by the spectrometer, the two-color method coupled with the emissivity ratio model developed by the laboratory of the current study is used to calculate the temperature of the semi-coke flame. Temperature measurement is not affected by the measuring distance with this method, and it includes the variation of spectral radiation with wavelength, yielding a more accurate result of the temperature of burning particles. The specific principle can be observed in [7].

This study investigates the flame radiation exergy-based experimental data and the radiation thermodynamics theory, which provides a reference for the energy cascading conversion system of fuel combustion, to characterize the available radiation energy. Spectral radiation exergy can be obtained by multiplying the radiative energy by a radiative exergy-to-energy ratio η_λ as shown in Eqs. (5.1) and (5.2).

The spectrum for particle radiation in solid fuel combustion is continuous and can be approximately regarded as a gray body [8, 9] in the waveband of < 1.1 μm. In the waveband of < 2.25 μm, no significant variation was also noted in the spectral emissivity with temperature [10]. Spectrum continuity and emissivity stability in the long waveband for solid vegetation combustion were also demonstrated in [11]. In a preliminary assessment, the linear extrapolation method is used in [12] to predict the spectral emissivity of the infrared waveband for solid fuel combustion. In this study,

the spectral emissivity is linearly extrapolated to the wavelength of 15 μm based on the measured emissivity trend in the near-infrared spectrum. The proportional distribution of spectral radiative energy and exergy in different wavebands can be obtained after calculating the spectral radiative energy and exergy in the corresponding wide spectral range.

5.2 Experimental Results and Discussion

5.2.1 Tube Furnace Experimental Results

5.2.1.1 Radiation Flux Results

The radiative energy and exergy flux for the two coals in the O_2/CO_2 atmospheres with different oxygen ratios are shown in Fig. 5.3a, b. For the two coals, the radiative energy flux increases from about 2 to 9 W/m^2 with an increase in the oxygen ratio from 21 to 60%; this occurs because the combustion rate increases with the oxygen ratio, releasing more radiative energy. Furthermore, higher local temperatures caused by higher oxygen ratios increase radiation flux. The radiative energy flux of the bituminous coal is greater than that of lignite. The radiative energy flux may be affected by both volatilization and calorific value. Bituminous coal and lignite burn more easily and have higher radiation fluxes because they have higher volatilization. Furthermore, its radiative energy flux is slightly higher than that of lignite because bituminous coal has the highest calorific value. In addition to the radiative energy, Fig. 5.3a, b show that the radiative exergy flux increases from approximately 1.5 to 6 W/m^2 as the oxygen ratio increases from 21 to 60%. The radiative exergy flux of the bituminous coal is greater than the lignite; this trend is similar to that of the radiative energy flux. Since the furnace remains at 800 °C, the results indicate that the trend of the radiative exergy flux as a function of the oxygen ratio is consistent with that of the radiative energy flux when the combustion temperature is constant. A comparison of the exergy-to-energy ratio illustrates that it is stable between 0.61 and 0.63. This indicates that the radiative exergy-to-energy ratio is generally similar at a specific combustion temperature. Theoretically, as the oxygen ratio increases, the proportion of radiative energy in the short-wavelength range increases, and thus the total radiative exergy increases.

Figure 5.3c, d show the radiative energy and exergy flux of two different coals at temperatures ranging from 600 to 1000 °C in a 30% O_2/CO_2 atmosphere. The temperature has a significant impact on the radiation flux. The radiative energy flux of the bituminous coal and lignite increases from approximately 2–14 W/m^2 as the temperature increases from 600 to 800 °C. According to Stefan-Boltzmann's law, the radiative power is generally proportional to the fourth power of the temperature; thus the radiative energy flux increases rapidly with the temperature [13]. The radiation flux of the bituminous coal is similar to that of the lignite. This is due to the use

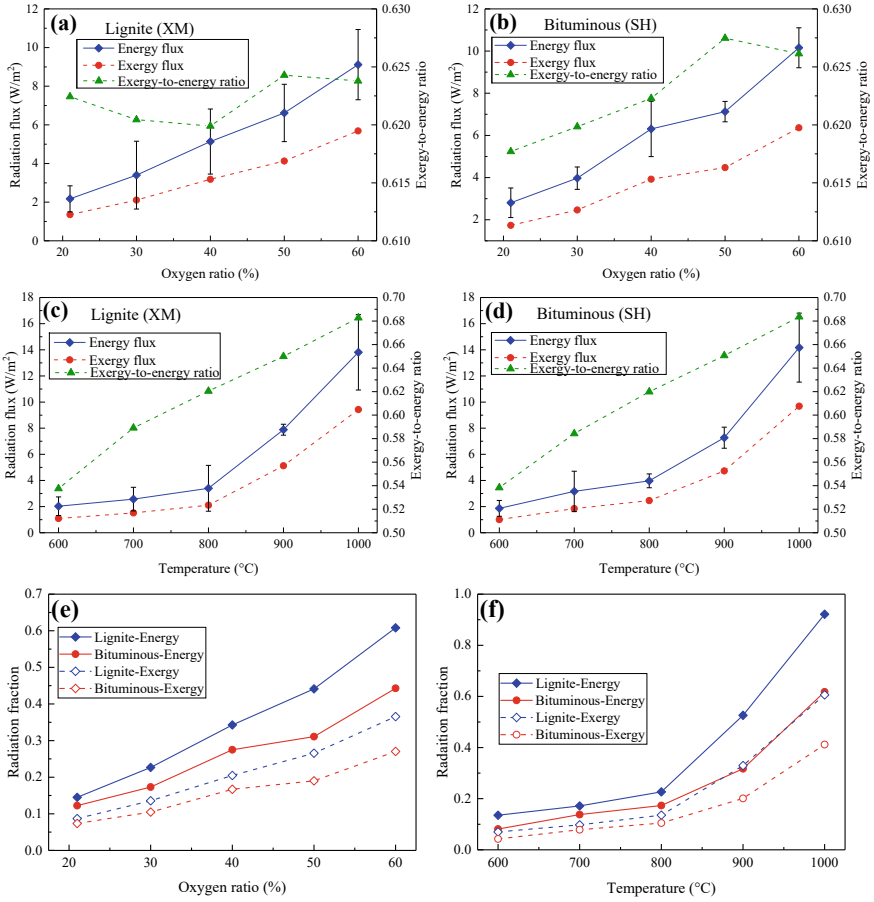

Fig. 5.3 Total radiative energy and exergy flux during oxy-coal combustion for **a** lignite and **b** bituminous coal with different oxygen ratios and **c** lignite and **d** bituminous coal with different temperatures. Radiation fraction and radiative exergy fraction during oxy-coal combustion with **e** different oxygen ratios and **f** different temperatures

of highly volatile bituminous coal, which, like lignite, has a high burning intensity. Thus, their local temperatures are higher, and the radiative energy flux is greater; additionally, the combustion temperature influences the radiation flux significantly. Figure 5.3c, d also show that the radiative exergy flux of the lignite and bituminous coal increases from about 1 to 10 W/m^2 with the increase in temperature from 600 to 1000 °C. The radiative exergy flux follows the same trend as the radiative energy as temperature rises. A comparison of the exergy-to-energy ratio shows that while the magnitudes of the radiative energy and exergy flux differ, the exergy-to-energy ratios of the two coals increase almost linearly from 0.54 to 0.68 with the temperature, and little difference exists between the two coals. This result indicates that the radiative exergy-to-energy ratio is essentially similar at a specific combustion temperature.

Furthermore, the coal ranks have little influence on the exergy-to-energy ratio with the temperature being the primary influencing factor.

The radiation and radiative exergy fractions are also investigated in this study. The radiation fraction is defined as the ratio of the radiation power released during the combustion process to the input power of the fuel, and the radiative exergy fraction is defined as the ratio of the radiative exergy power to the input exergy power of the fuel. Thus, the radiation and radiative exergy fractions can be calculated following the definition, and their variations are then investigated under different conditions. The chemical exergy of coal is calculated using the approximate formula shown below:

$$E_{\text{fuel}} = LHV\left[1.0064 + 0.1519\frac{n(\text{H})}{n(\text{C})} + 0.0616\frac{n(\text{O})}{n(\text{C})} + 0.0429\frac{n(\text{N})}{n(\text{C})}\right] \tag{5.8}$$

where LHV is the low heat value, and $w(C)$, $w(H)$, $w(O)$, and $w(N)$ are the mass fractions of the elements in the coal. The equivalent reaction time is set to 160 s because the tube furnace is fed with coal at one time, and the input powers of different coals are calculated according to the LHV. Assuming that the radiation basically conforms to Lambert's law, it can be supposed that the received radiation flux is consistent in the entire hemisphere with the radius of the distance from the sample to the sensor. Therefore, the output radiation power of fuel combustion can be calculated by multiplying the hemisphere area by the detected radiation heat flux.

Despite the relevant assumptions, it is believed that the estimated results could still reflect the relative variation of the radiation fraction under different conditions, which differs from the radiative power variation shown in Fig. 5.3a–d. Figure 5.3e, f show how the radiation fraction and radiative exergy fraction change with oxygen ratio and temperature during the combustion process. As the oxygen ratio and temperature increased, so did the radiation fraction and radiative exergy fraction. These findings suggest that increasing the oxygen ratio and combustion temperature in the coal combustion process can increase the proportions of radiative energy and exergy to the total energy, which is beneficial to the graded conversion of radiative energy during combustion. Furthermore, the variation characteristics of the radiation and radiative exergy fractions are similar in different atmospheres. The radiative exergy fraction is less than the radiation fraction, indicating that the quality of fuel chemical energy is higher than that of radiative energy, and combustion is an energy-losing process. A more efficient energy cascade conversion system must take chemical energy conversion into account. Furthermore, lignite has been discovered to have higher radiation and radiative exergy fractions than bituminous coal. This indicates that lignite, which burns more easily, emits more radiation during the combustion process. Bituminous coal is commonly used in power plant boilers because lignite has a lower calorific value and anthracite is difficult to burn. Highly volatile solid fuels (e.g., lignite) could be considered for combustion energy cascade conversion systems.

5.2.1.2 Spectral Radiation Results

The spectral radiation results are discussed in this section. The spectral radiation proportion is defined as the ratio of spectral radiation flux in a waveband to total radiation flux. Similarly, the spectral radiative exergy proportion is defined as the ratio of spectral radiative exergy flux in a waveband to the total radiative exergy flux. Thus, they can be computed using the definition. Figure 5.4a, b show how the spectral radiative energy and exergy change with the oxygen ratio during combustion in an O_2/CO_2 atmosphere at 800 °C temperature. The radiative energy ratio is highest in the waveband of 1.125–4.1 μm and increases from about 40 to 50% with the oxygen ratio. Additionally, the radiative energy ratio is approximately 40% in the waveband of 4.1–10 μm, whereas it is about 10% in the spectrum of > 10 μm. The experimental data for radiation of < 1.125 μm are close to zero due to the low energy proportion in this spectrum. Furthermore, fluctuations affect the results. Thus, these data should only be used as a reference.

The participating media influence the spectral radiation distribution. The energy proportion in the far-infrared spectrum of the actual radiation is greater than that of gray-body radiation due to the presence of CO_2 and H_2O in the combustion process [13]. The radiation proportion in the waveband of 1.125–4.1 μm is found to increase

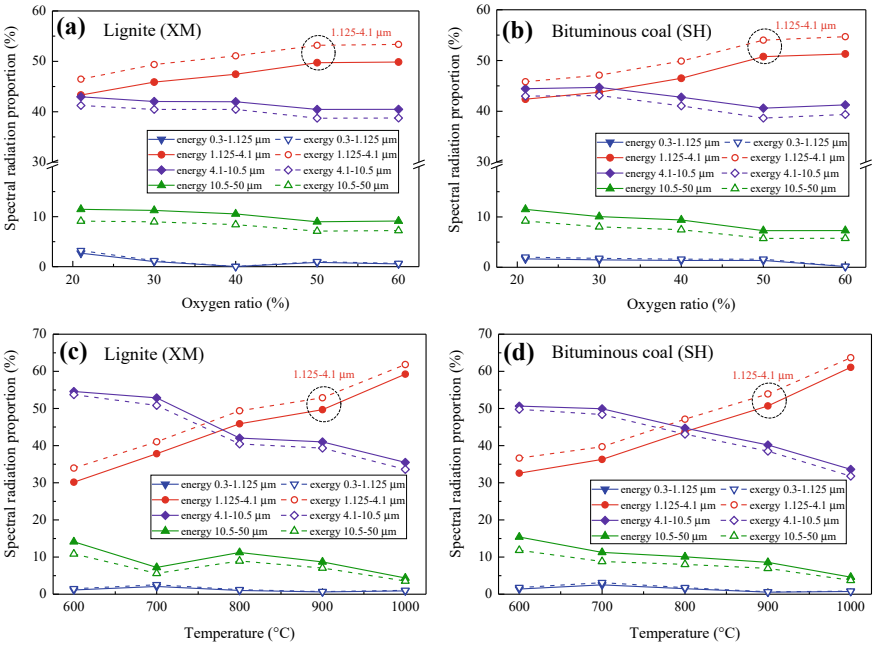

Fig. 5.4 Spectral radiative energy and exergy during oxy-coal combustion versus the oxygen ratio for **a** lignite and **b** bituminous coal versus the temperature for **a** lignite and **b** bituminous coal

with the increase in the oxygen ratio, whereas it decreases in the 4.1–10.5 and 10.5–50 μm wavebands. This occurs because a higher oxygen ratio increases the burning rate and the local combustion temperature, causing the spectral distribution to shift to shorter wavelengths following Wien's displacement law [13]. Furthermore, the CO_2 decrease in the atmosphere caused by an increase in the oxygen ratio reduces the shift to longer wavelengths. Bright flames are observed during the combustion of lignite and bituminous coal. This is attributed to the fact that bituminous coal and lignite burn intensely and have higher burning temperatures [14]; thus, Fig. 5.4a, b reveal higher radiation proportions in the waveband of < 4.1 μm for lignite and bituminous coal. Furthermore, radiation accounted for a greater proportion of the waveband of > 4.1 μm during lignite combustion because lignite contains more moisture than bituminous coal; however, this effect is weak. In addition, Fig. 5.4a, b show that the trend of the radiative exergy flux with increasing oxygen ratio is similar to the trend of the radiative energy flux in various bands. This is primarily because radiative exergy is derived from radiative energy. Moreover, the radiative exergy ratio was also discovered to be greater than the radiative energy ratio in the waveband of < 4.1 μm, but less than the radiative energy ratio in the waveband of > 4.1 μm. This indicates that the exergy-to-energy ratio is greater for shorter-wavelength radiation of < 4.1 μm, implying that shorter wavelengths are more useful.

Figure 5.4c, d depict the spectral radiative energy and exergy flux versus temperature in a 30% O_2/CO_2 atmosphere. In terms of the spectral radiative energy flux characteristics, the radiative energy ratio in the waveband of 1.125–4.1 μm increases from about 30 to 60% with the increase in the temperature from 600 to 1000 °C, whereas that in the waveband of 4.1–10.5 μm decreases from approximately ~50 to 35%. Furthermore, the radiative energy ratio in the spectrum of > 10.5 μm falls from approximately 15 to 5%. The radiation proportion in the waveband of < 1.125 μm should theoretically increase with temperature. This trend, however, is not observed in Fig. 5.4c, d because the energy ratio in this band is small and the experimental fluctuation has a large influence on the results. These findings suggest that temperature is the most important factor influencing the spectral distribution of radiative energy in pulverized coal combustion; this is explained by Wien's displacement law, which states that as temperature rises, spectral radiation shifts to a shorter wavelength [13]. Generally, radiation transfer occurs with participating media in pulverized coal combustion. Because of the presence of soot, CO_2, and H_2O, it cannot be simply regarded as gray-body radiation [13]. Nonetheless, the spectral radiation distribution characteristics still follow the basic law of radiation; thus, in this experiment, the proportion of radiative energy increases in the spectrum range of < 4.1 μm and decreases in the spectrum range of > 4.1 μm. Furthermore, as shown in Fig. 5.4c, d, the different coals do not exhibit different influences on the spectral radiation as temperature increases. Coal combustion is complete at temperatures of > 800 °C [15]; so the spectral radiation characteristics during combustion for the two coals at high temperatures are essentially similar. The trend of the radiative exergy flux with increasing temperature is similar to that of the radiative energy in each waveband. Furthermore, the radiative exergy ratio is greater than the radiative energy ratio in the waveband of < 4.1 μm, while it is lower than the radiative energy ratio in the

waveband of > 4.1 μm; this is consistent with the results in Fig. 5.4a, b. These findings suggest that radiation with short wavelengths of < 4.1 μm has a higher exergy-to-energy ratio and thus has greater practical significance. Thus, increasing the short-wavelength radiative energy ratio in combustion radiation can improve overall radiative exergy, which is important for energy conversion and management.

5.2.2 Small Flat-Flame Burner Experimental Results

5.2.2.1 Temperature and Radiation Flux Results

Table 5.4 displays the temperature measurements made using the improved two-color method based on spectral data. The spectral radiation that peaks near 589 and 769 nm in the flame radiation spectra are primarily caused by the characteristic radiation of the Na and K elements [15]. The waveband affected by characteristic radiation is thus removed when calculating the temperature. The measured temperature is observed to deviate from the design temperature near the burner outlet. At the measuring point of 7 cm, for example, it is 1519.37 and 1602.71 °C in cases 2 and 3, which differ from the design temperature of 1400 °C. This is primarily due to the deviation of secondary airflow from ideal conditions and the temperature increase in the particles caused by the semi-coke combustion. In addition, it may also be related to the signal-to-noise ratio of the data collection and the model-matching degree of the two-color method.

The measured temperature at 20 cm above the burner outlet is similar to the design temperature, indicating that the combustion reaction has a significant impact on the flame temperature. Despite being influenced by the experimental conditions, the temperature results are still representative of the 10- to 14-cm middle section. The temperature of case 2 is similar to that of case 3, close to the setting temperature of 1400 °C, whereas the temperature of case 1 is lower due to the lower setting temperature. Moreover, the temperature in case 4 is higher than that in case 3 by approximately 100 °C, indicating a higher actual temperature for a higher oxygen ratio when the setting temperature is similar.

Figure 5.5 depicts the total radiative energy and exergy along the flame under various experimental conditions. The measurement's spectral range of total radiative energy is 500–1100 nm, covering visible and near-infrared wavebands. Although it

Table 5.4 Measured temperature by the two-color method based on radiation spectrum

Temperature °C	7 cm	10 cm	14 cm	17 cm	20 cm
Case 1	1517.36	1501.52	1425.56	1360.51	1218.18
Case 2	1519.37	1482.20	1463.70	1450.99	1428.38
Case 3	1602.71	1464.27	1450.05	1420.93	1420.25
Case 4	1877.65	1690.17	1597.56	1527.61	1451.74

accounts for a small proportion of the total thermal radiation spectrum, it is extremely useful due to its short-wavelength. This waveband is important for studies because it is suitable for photovoltaic conversion of commercial Si cells. Moreover, Fig. 5.5 shows that the radiative energy intensity under the four cases increases first and then decreases from the burner outlet upwards. A slight fluctuation exists in case 3 as shown in Fig. 5.5c, which is due to measurement error, but it is roughly in line with the overall trend. These findings suggest that the radiation intensity distribution along the flame is related to the combustion reaction intensity, showing a trend of first increasing and then decreasing and presenting a cone-shaped flame shape. Furthermore, the highest radiation intensity is found to be at 17, 10, 17, and 15 cm in cases 1, 2, 3, and 4, respectively. This indicates that ignition occurs first in case 2, second in case 4, and finally in case 1 or 3. The radiation intensity peak appears first in case 2 because it has the highest setting temperature (1400 °C). Furthermore, the diffusion rate of O_2 molecules is faster in the O_2/N_2 atmosphere than in the O_2/CO_2 atmosphere, resulting in a faster oxidation rate of semi-coke and an earlier ignition. Because the ignition occurs late in the O_2/CO_2 atmosphere, the radiation intensity peak in cases 3 and 4 occurs later than in case 2. Furthermore, because the O_2 ratio is higher in case 4, the radiation intensity peak arises earlier than that in case 3; additionally, the radiation intensity peak in case 1 appears later because its design temperature is lower. This analysis shows that the reaction atmosphere, temperature, and oxygen ratio all affect the radiation intensity peak and ignition. The O_2/CO_2 atmosphere retards ignition, whereas high-temperature and high oxygen ratio conditions promote early ignition and cause the radiation intensity to peak earlier.

Furthermore, the highest radiation intensity in case 2 is higher than that in case 1 by about 700 W/m^2, indicating that high-temperature directly increases radiation intensity; whereas the highest radiation intensity in case 4 is higher than that in case 3 by about 350 W/m^2, indicating that increasing oxygen ratio will also increase flame radiation intensity. Furthermore, the peak radiation intensity in case 2 is about 600–950 W/m^2 higher than in cases 3 or 4, indicating that when the parameters (e.g., oxygen ratio or flue gas temperature) are similar under different atmospheres, the radiation intensity in the O_2/CO_2 atmosphere is lower than that in the O_2/N_2 atmosphere. This is primarily due to the lower combustion intensity caused by the slower diffusion of O_2 in the CO_2 and the low local temperature caused by the higher specific heat capacity of CO_2. Furthermore, the gasification of semi-coke and the slow oxidation reaction rate caused by the addition of CO_2 will affect the properties and distribution of combustion potentially increasing medium absorption along the path length and resulting in lower measured radiation intensity.

Finally, Fig. 5.5 shows that the total radiation exergy curve along the flame path length is consistent with the radiation energy curve, and its absolute value is less than the radiation energy. Furthermore, higher radiation intensity results in a greater difference between radiative energy and radiative exergy. Further investigation reveals that the exergy-to-energy ratios of the four cases are all around 82%, where it is higher and lower in cases 4 (82–85%) and case 1 (80–82.5%), respectively. The measured temperature of each point in case 4 is higher while it is lower in case 1. The variation

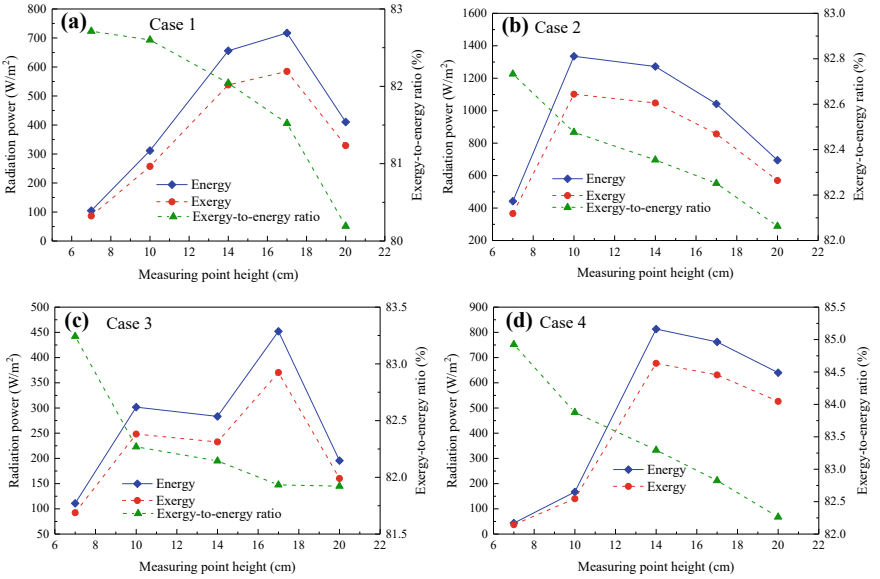

Fig. 5.5 Total radiative energy and radiative exergy along the flame under different cases

curve of the radiation exergy-to-energy ratio under the four cases is similar to the measured temperature. It implies that the radiation temperature is the most important factor influencing radiation exergy, whereas the influence of the spectral waveband is not obvious in Fig. 5.5.

5.2.2.2 Spectral Radiation Results

Particle radiation dominates in solid fuel combustion, and a continuous spectrum was noted [16, 17]. Based on the measured emissivity trend in the near-infrared spectrum, the spectral emissivity is linearly extrapolated to the wavelength of 15 μm. Figure 5.6 show the spectral radiative energy and exergy characteristics in a broad spectrum (cases 2 and 4 are selected). The spectral radiative energy is primarily concentrated in the 1.1–3 μm band at the current flame temperature (~ 1200–1800 °C). The spectral radiation in the wavelength of < 3 μm is useful in actual photovoltaic conversion because the Si cell match the spectral radiation of < 1.1 μm and the III–V semiconductor cells (e.g., InAsSbP) matches the spectral radiation of < 3 μm [18]. High temperatures are advantageous for the utilization of radiative energy in combustion. The spectral radiative energy in the waveband of < 3 μm along the path length is similar to the variation trend in Fig. 5.5 (0.3–1.1 μm) as shown in Fig. 5.6. The spectral radiative energy in the waveband of > 3 μm shows an increasing trend at 17 and 20 cm. The radiation in waveband of > 3 μm accounts for more because the temperatures at 17 and 20 cm are lower. The spectral distributions of the radiation

exergy under different conditions are similar to those of radiative energy because the radiation exergy is calculated from the radiation energy. Figure 5.6e depicts the exergy-to-energy ratio of spectral radiation in cases 2 and 4, demonstrating that the spectral exergy-to-energy ratio is greater for shorter wavelengths in each case which could be between 76 and 85% for the waveband of < 3 μm. The measured temperature influences the difference in the exergy-to-energy ratio at different points. Furthermore, the exergy-to-energy ratio is greater at higher temperatures. These findings suggest that short-wavelength and high-temperature radiation energy are more valuable.

Even when professional fixtures (e.g., optical brackets and moving rails) are used to assist spectrometer measurement, a deviation in the measured radiation value

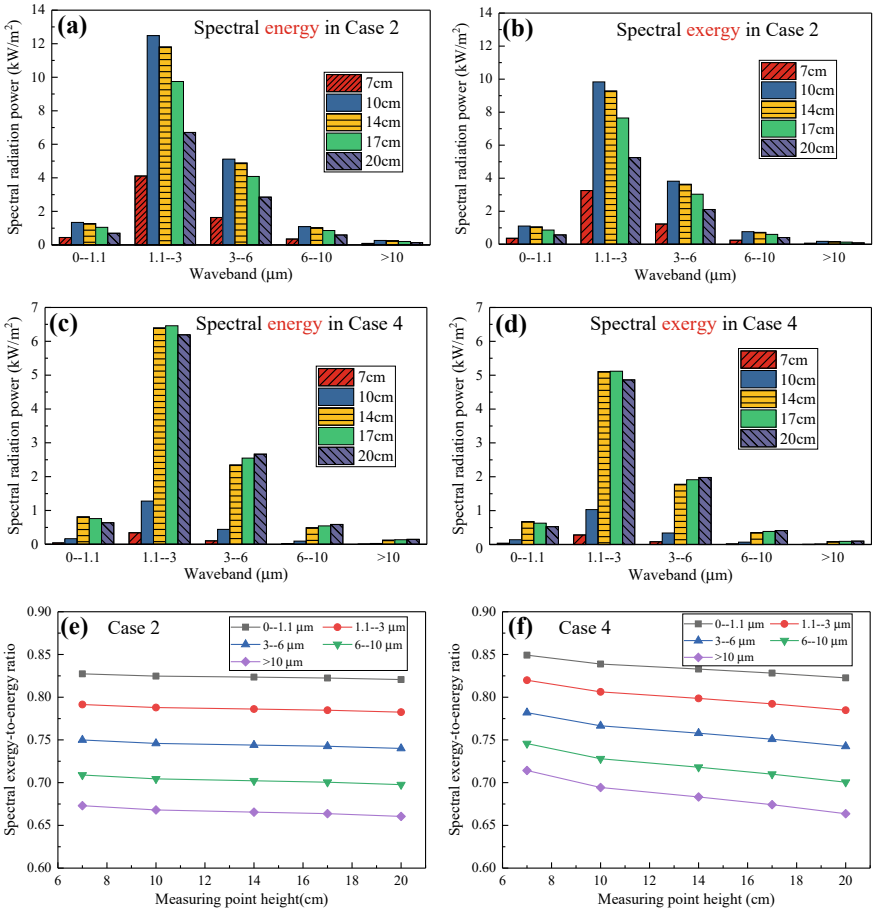

Fig. 5.6 **a**–**d** Spectral radiative energy and exergy distribution and **e** and **f** spectral exergy-to-energy ratio for different cases

under different conditions still exists due to the influence of the measurement environment. The absolute value of the spectral radiative energy in Fig. 5.6 provides only a limited amount of information. The proportion of spectral radiative energy and exergy in various cases is discussed further. The proportion characteristics have more significance for reference than the absolute value (Fig. 5.7). In different cases, the largest proportion can be observed to be in a waveband of 1.1–3 μm. The proportion of spectral radiative energy of < 3 μm wavelength decreases with distance from the burner outlet, whereas the proportion of > 3 μm wavelength increases. The spectral radiation distribution shifts to the long-wavelength direction according to Planck's law because the flame temperature decreases with distance; thus, the proportion of the long-wavelength radiation increases while that of the short-wavelength radiation decreases. Emissivity decreases with temperature in the experiment; this phenomenon is more visible in the measured short-wavelength and theoretically weakens the increasing short-wavelength proportion. Indeed, the results show that increasing the temperature does not affect the short-wavelength proportion of the measuring point. However, the proportion of short-wavelength radiation (< 3 μm) is still greater than that of long-wavelength radiation for a given measuring point spectrum. This means that the effect of temperature on spectral emissivity is insufficient to change the overall trend of spectral distribution with temperature. Furthermore, Fig. 5.7 shows that the proportion of the spectral radiative energy under different cases is relatively stable, and the variation in each waveband is within 5%. Case 4 has a higher proportion of radiative energy in the waveband of 0.5–1.1 μm than the other cases because its measured temperature is higher, and case 2 has a higher proportion of energy in the wavelength of < 3 μm than case 1. These characteristics are especially noticeable at 20 cm, indicating that increasing the combustion temperature may increase the proportion of short-wavelength radiation. Case 4 has a higher proportion of energy in the wavelength of < 3 μm than in case 3, indicating that increasing the oxygen ratio may increase the proportion of short-wavelength radiation. Cases 2 and 3 have very similar spectral energy distribution characteristics, indicating that the oxy-fuel atmosphere has little effect on the spectral radiation proportion under similar temperature conditions. Particle radiation dominates solid fuel combustion in an oxy-fuel atmosphere, while radiation from gases and other media accounts for a smaller proportion [16, 17]. CO_2 gasification and its high specific heat could affect particle combustion, affecting local particle temperature and particle emissivity. Because temperature is the most influential factor influencing combustion radiation, increasing the oxygen ratio to raise the temperature is beneficial for increasing short-wavelength radiation, which is important for radiative energy utilization. The results of radiation exergy proportion are consistent with that of radiative exergy in various cases as shown in Fig. 5.7e, f. Thus, the radiative energy proportion can be approximated by the radiation exergy proportion. The proportion of radiative exergy in the waveband of < 3 μm is slightly higher than that of radiative energy, whereas it is slightly lower in the waveband of > 3 μm. This is because high-frequency radiative energy has a higher equivalent radiation temperature and its radiative exergy is relatively higher.

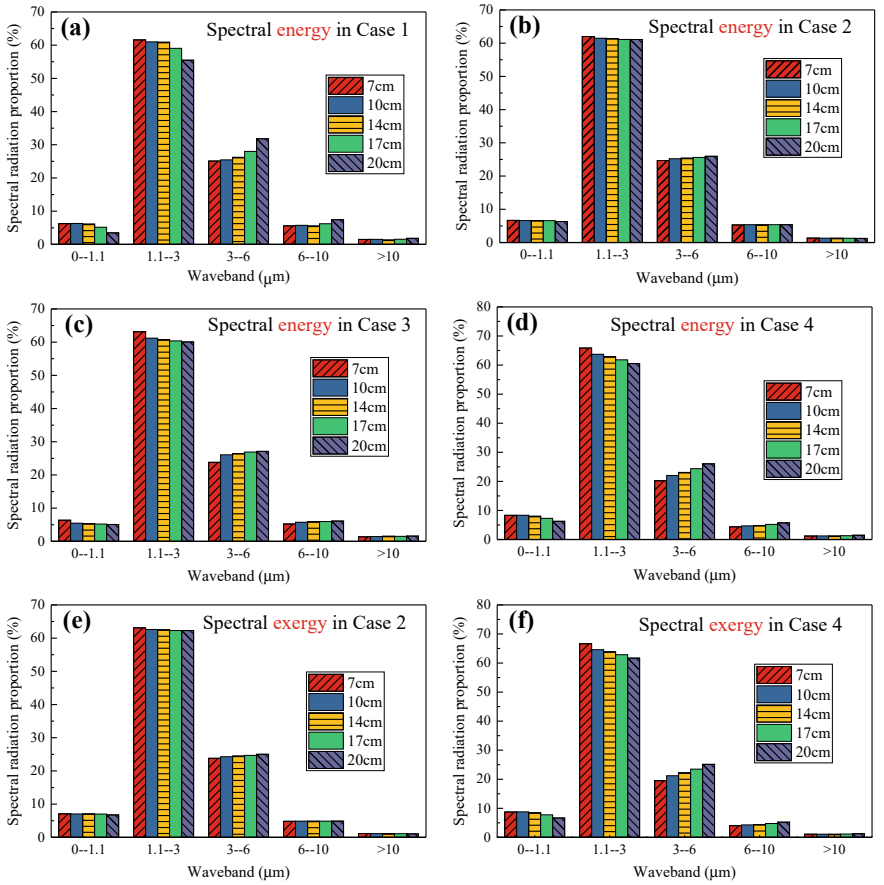

Fig. 5.7 Proportion distribution of radiative energy and radiative exergy under different experimental cases

5.3 Numerical Verification

5.3.1 Design of One-Dimensional Cases

One-dimensional cases are built for media radiation transfer calculation based on the parameters of the tube furnace experiment (e.g., furnace temperature and reaction conditions). The spectral radiative energy characteristics are predicted via one-dimensional cases, and the calculated and experimental results are compared. The length of the quartz tube determines the size of the one-dimensional case, which is set at 60 cm. The thermocouple temperature curve in the furnace has a trapezoidal distribution. The temperature formulas in Table 5.5 are used for the cases to match the temperature distribution in the furnace. The calculated temperature has a

Table 5.5 Temperature curve formulas in cases

Furnace setting temperature (°C)	Formula of temperature curve
600	$T = 690 - 190\cos\left(\frac{2\pi x}{L}\right)$ (K)
700	$T = 765 - 215\cos\left(\frac{2\pi x}{L}\right)$ (K)
800	$T = 865 - 215\cos\left(\frac{2\pi x}{L}\right)$ (K)
900	$T = 940 - 240\cos\left(\frac{2\pi x}{L}\right)$ (K)
1000	$T = 1015 - 265\cos\left(\frac{2\pi x}{L}\right)$ (K)

similar curve bend to the measured temperature. This study is primarily concerned with the spectral radiation proportion; thus, it should ensure that the highest and lowest temperatures of the one-dimensional temperature field are consistent with the measured values and that the designing temperature curve is also as close to the measured value as possible along the entire length. This ensures the model's rationality and calculation precision, allowing the model to be applied to the calculation cases.

The calculation cases are based on bituminous coal (SH) combustion and a 30% O_2/CO_2 atmosphere. The effective reaction time is set to 160 s based on the experimental results. The flue gas atmosphere of the cases is calculated using the parameters of airflow and coal characteristics under the assumption of complete combustion. The calculated H_2O/CO_2 molar ratio is 0.022 and the proportion of triatomic gas is 0.75. The gas radiation properties are described using the WSGG model proposed in Chap. 3. Coal combustion generates a large number of particles and is an important radiation medium; thus, particle radiation is taken into account in the calculation cases. The parameters of the particles during combustion are determined using the results reported in the existing literature and summarized in Table 5.6.

In Table 5.6, absorption coefficient κ and scattering coefficient σ is calculated according to the formulas [17, 19]:

$$\kappa = Q_{\text{abs}} A_{\text{p}} \tag{5.9}$$

$$\sigma = Q_{\text{sca}} A_{\text{p}} \tag{5.10}$$

Table 5.6 Radiative parameters of the particles during combustion

	Coal		Ash	
	Symbol	Value	Symbol	Value
Absorption factor [17]	$Q_{\text{abs,coal}}$	0.9	$Q_{\text{abs, ash}}$	1
Scattering factor [17]	$Q_{\text{sca,coal}}$	1.1	$Q_{\text{sca, ash}}$	1.4
Projected area per volume [19]	$A_{p\text{coal}}$	0.75	$A_{p\text{ash}}$	0.125
Absorption coefficient	κ_{coal}	0.675	κ_{ash}	0.125
Scattering coefficient	σ_{coal}	0.825	σ_{ash}	0.175

For the total particles, $\kappa_{\text{part}} = \kappa_{\text{coal}} + \kappa_{\text{ash}} = 0.8$ and $\sigma_{\text{part}} = \sigma_{\text{coal}} + \sigma_{\text{ash}} = 1$.

The radiation parameters are also highest because the particle concentration is highest at the combustion center. Furthermore, the radiation parameters are zero because the minimum concentration at both ends is zero. Consequently, the radiation parameter curve in the one-dimensional case is expressed by the following equations.

$$\kappa_{\text{part}} = 0.4 - 0.4\cos\left(\frac{2\pi x}{L}\right) \tag{5.11}$$

$$\sigma_{\text{part}} = 0.5 - 0.5\cos\left(\frac{2\pi x}{L}\right) \tag{5.12}$$

Furthermore, the Henyey–Greenstein distribution is chosen as the scattering phase function:

$$\Phi_{\text{HG}}(\phi) = \left(1 - g^2\right)/\left(1 + g^2 - 2g\cos\phi\right)^{3/2} \tag{5.13}$$

where g is set as 0.86 based on a previous study [19]. The radiation characteristics of different temperature conditions in a 30% O_2/CO_2 atmosphere are considered in the case study, and the calculation is similar to that used in Chap. 3. The proportional characteristics of spectral radiative heat flux are investigated here. The radiation spectral proportion is unaffected by the absolute radiation intensity and can be compared to experimental results.

Furthermore, the same analysis methods and parameters used in the flat-flame burner experiment for semi-coke particle parameters are used here. The semi-coke particles radiation parameters are $\kappa_{\text{part}} = 0.8$, $\sigma_{\text{part}} = 1$. The particle concentration is assumed to be the greatest at the center of the flame, so the radiation parameter is greatest, and the concentration at the two walls is the lowest to zero, so the radiation parameter is also zero. Moreover, Eqs. (5.11) and (5.12) continue to represent the radiation parameter distribution curves. The scattering phase function also chooses the Henyey–Greenstein distribution as expressed in Eq. (5.13), with $g = 0.86$.

5.3.2 Numerical Verification Results

First, the comparison of the spectral radiation proportions calculation results in one-dimensional cases with the tube furnace experimental results is discussed. The variations in the predicted spectral radiation proportion and the experimental results versus the temperature under a 30% O_2CO_2 atmosphere are similar, and the calculated results agree well with the experimental results for various cases at different temperatures. The maximum difference between calculated and experimental results is ~ 3% for the case at the temperature of 600 °C, whereas the differences are less with a maximum of ~ 2%, for the three respective cases at temperatures of 700, 800, and 900 °C. Furthermore, the difference is greater for the case with a temperature of

1000 °C, with a maximum difference of about 5%. This could be due to the difficulty of the experimental control at high temperatures as well as the large fluctuations in the reaction after feeding the coal. Figure 5.8a, b depict the typical cases at 700 °C and 1000 °C, respectively. These results indicate that the simulated results are reasonable in the 600–1000 °C temperature range. Furthermore, the corresponding simulated temperature curve has a larger gap with the measured temperature field along the path length when the temperature difference is > 1000 °C. Thus, the theoretical accuracy of the prediction results will be slightly reduced. Thus, the calculation and the experimental results are relatively close to the gray-body radiation spectrum. This also suggests that the radiation spectrum characteristics of combustion media in the presence of particles are similar to gray-body radiation, indicating that particle radiation has the greatest impact in solid fuel combustion [19].

The predictions of the oxyfuel conditions for cases 3 and 4 are better with small errors up to ~ 2% for the numerical verification results of small flat-flame burner experiment results. However, the calculation results for the air-combustion conditions in cases 1 and 2 are poor, with errors of ~ 6%. Figure 5.8c, d depict typical cases 2 and 4. The calculation results also show that the calculated radiative heat flux and radiative source terms under oxy-fuel conditions are several times higher than those under air-combustion conditions, indicating that the oxy-fuel combustion atmosphere has stronger radiative heat transfer. The error generated when analyzing the

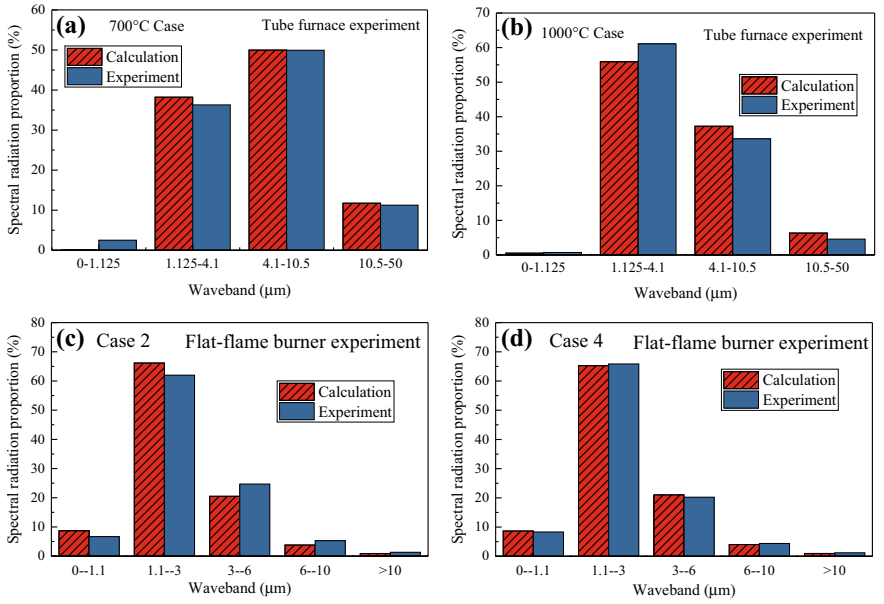

Fig. 5.8 Comparison of the calculation results of the spectral radiation proportion in one-dimensional cases **a** and **b** for tube furnace experiment and **c** and **d** for the small flat-flame burner experiment

radiative energy proportion may be smaller for a higher radiative heat flux. Furthermore, regardless of the oxy-fuel or air-combustion condition, both the calculation and experimental results of the proportional distribution are similar, indicating that particle radiation plays a significant role in the combustion medium. The results show that a one-dimensional numerical calculation can accurately predict the spectral proportion when compared to experimental results. Thus, further studies could adopt numerical simulation to investigate spectral radiative energy characteristics in flame as a reasonable supplementary.

5.4 Summary

This chapter introduced the spectral radiative energy and exergy characteristics in the oxyfuel combustion of solid fuels under different atmospheres in a fixed-bed furnace and small Hencken flat-flame burner from the perspective of energy utilization. The effects of various fuels, temperature, atmosphere, and oxygen ratio are investigated. The following summary can be drawn.

1. In the tube furnace experiment, the radiative energy of coal combustion increases with oxygen ratio and temperature, with temperature having a greater influence. The radiative exergy follows a similar pattern as the radiative energy. Temperature influences the radiative exergy-to-energy ratio more than coal rank and oxygen ratio. The radiative exergy-to-energy ratios of various coals are comparable at a given combustion temperature.

The spectral radiation ratio increases in the waveband of < 4.1 μm as the oxygen ratio and combustion temperature increase, with the temperature being the most influential factor. At temperatures of > 800 °C, the coals have no discernible effect on the spectral radiation distribution. The trends of radiative exergy as temperature and oxygen ratio increase in each waveband are similar to those of the radiative energy. Increased short-wavelength radiation ratio during combustion can improve total radiative exergy, which is advantageous for energy conversion and management.

The radiative exergy fraction is less than the radiation fraction during combustion, indicating that the chemical energy in the fuel is of a higher quality than that of radiative energy. Thus, a more efficient energy cascade conversion system must consider chemical energy conversion. Lignite has a higher radiation fraction and radiative exergy fraction than bituminous coal. Thus, lignite or other highly volatile solid fuels could be used for combustion in photo-thermal energy cascade conversion systems.

2. In a small flat-flame burner experiment, a high designed temperature and a high oxygen ratio could increase the flame radiation intensity. The radiation intensity is lower in the O_2/CO_2 atmosphere. The oxyfuel atmosphere's influence on the radiative spectrum is primarily due to the actual combustion temperature. Additionally, the effects of combustion and gasification reactions on particles and

other products may affect the emission and absorption of the medium along the path length. The total radiation exergy curve along the flame height is similar to that of radiative energy, and its absolute value is less than that of the radiative energy. The radiation exergy-to-energy ratio curve along the path length is similar to that of the measured temperature in different cases. Thus, the temperature is assumed to be the primary factor affecting radiation exergy.

The spectral radiative energy has the highest proportion in the 1.1–3 μm waveband, reaching > 60%. In different cases, the variation of spectral radiation proportion in each waveband is within 5%. The proportion of the short-wavelength energy can be increased by increasing the combustion temperature and oxygen ratio, whereas the O_2/CO_2 atmosphere has little effect on the proportion of spectral radiation. The spectral radiative energy proportion can be used to approximate the spectral radiation exergy. Short-wavelength and high-temperature radiation energy is more important for utilization because the spectral exergy-to-energy ratio could reach between 76 and 85% in the waveband of < 3 μm.

3. The one-dimensional calculation radiation transfer cases built on combustion characteristics can accurately simulate the proportional characteristics of spectral radiation. As a reasonable supplement, further studies could use numerical simulation to investigate spectral radiative energy characteristics in flame.

References

1. Shan S, Zhou Z, Wang Z et al (2019) Radiative energy flux characteristics and model analysis for one-dimensional fixed-bed oxy-coal combustion. J Zhejiang Univ Sci A 20(6):431–446
2. Kirdyashkin A, Orlovskii V, Sosnin E et al (2010) Energy and spectral characteristics of radiation during filtration combustion of natural gas. Combust Explosion Shock Waves 46(5):523–527
3. Bejarano P, Levendis Y (2008) Single-coal-particle combustion in O_2/N_2 and O_2/CO_2 environments. Combust Flame 153(1–2):270–287
4. Zhang Z, Li X, Luo C et al (2018) Investigation on the thermodynamic calculation of a 35 MWth oxy-fuel combustion coal-fired boiler. Int J Greenhouse Gas Control 71:36–45
5. Yuan Y, Li S, Xu Y et al (2017) Experimental and theoretical analyses on ignition and surface temperature of dispersed coal particles in O_2/N_2 and O_2/CO_2 ambients. Fuel 201:93–98
6. Yuan Y, Li S, Li G et al (2014) The transition of heterogeneous–homogeneous ignitions of dispersed coal particle streams. Combust Flame 161(9):2458–2468
7. Shao L, Zhou Z, Chen L et al (2018) Study of an improved two-colour method integrated with the emissivity ratio model and its application to air-and oxy-fuel flames in industrial furnaces. Measurement 123:54–61
8. Sun Y, Lou C, Zhou H (2011) A simple judgment method of gray property of flames based on spectral analysis and the two-color method for measurements of temperatures and emissivity. Proc Combust Inst 33(1):735–741
9. Cai X, Cheng Z, Wang S (2007) Flame measurement and combustion diagnoses with spectrum analysis. AIP Conf Proc Am Inst Phys 914(1):60–66
10. Graeser P, Schiemann M (2020) Investigations on the emissivity of burning coal char particles: influence of particle temperature and composition of reaction atmosphere. Fuel 263:116714

11. Johnston J, Wooster M, Lynham T (2014) Experimental confirmation of the MWIR and LWIR grey body assumption for vegetation fire flame emissivity. Int J Wildland Fire 23(4):463–479
12. Schiemann M, Gronarz T, Graeser P et al (2019) A correlation between char emissivity and temperature. Fuel 256:115889
13. Modest M (2013) Radiative heat transfer, 3rd edn. Elsevier, Amsterdam
14. Moon C, Sung Y, Ahn S et al (2013) Thermochemical and combustion behaviors of coals of different ranks and their blends for pulverized-coal combustion. Appl Thermal Eng 54(1):111–119
15. He Y, Zhu J, Li B et al (2013) In-situ measurement of sodium and potassium release during oxy-fuel combustion of lignite using laser-induced breakdown spectroscopy: effects of O_2 and CO_2 concentration. Energy Fuels 27(2):1123–1130
16. Johansson R, Leckner B, Andersson K et al (2013) Influence of particle and gas radiation in oxy-fuel combustion. Int J Heat Mass Transf 65:143–152
17. Gronarz T, Schulze J, Laemmerhold M et al (2017) Quantification of the influence of parameters determining radiative heat transfer in an oxy-fuel operated boiler. Fuel Process Technol 157:76–89
18. Ferrari C, Melino F, Pinelli M et al (2014) Thermophotovoltaic energy conversion: analytical aspects, prototypes and experiences. Appl Energy 113:1717–1730
19. Kez V, Consalvi J, Liu F et al (2019) Investigation of gas and particle radiation modelling in wet oxy-coal combustion atmospheres. Int J Heat Mass Transf 133:1026–1040

Chapter 6
Outlook

From the perspective of energy cascade utilization, this book points out that the traditional power generation method is limited by the maximum parameters of the thermal power cycle, so it cannot effectively utilize high-temperature combustion energy. Against this, it is proposed the academic idea of photo-thermal energy cascade conversion for fuel combustion. Several thermal radiation theories for fuel combustion are introduced based on radiative energy utilization with the main innovations of these theories are summarized as follows:

1. A radiation engine model is proposed to explain the exergy expression of blackbody radiation using the classical thermodynamic analysis method. The infinite-staged Carnot heat engine model is innovatively created based on the concept of equivalent temperature, and the expression of the monochromatic radiative exergy is deduced. Consequently, a relatively complete theory for evaluating the energy quality of spectral radiation is established. Combining the monochromatic radiation exergy theory with the radiation transfer equation yields the monochromatic radiation transfer equations for radiative entropy and radiative exergy.
2. The WSGG model for gas medium radiation characteristics is improved to accommodate the pressurized combustion conditions. Several parameters suitable for the radiation characteristics of complex combustion conditions are developed based on the improved WSGG model, particularly the WSGG model parameters in the high-pressure range and oxy-fuel combustion conditions. Furthermore, their accuracy and necessity are verified.
3. From the perspective of energy utilization, the radiative energy characteristics and spectral energy distribution characteristics of oxy-fuel combustion are investigated using various furnaces, with special emphasis placed on the spectral radiative exergy characteristics. The findings of the study serve as the foundation for the design and development of a photo-thermal energy cascade conversion system for fuel combustion.

S. Shan et al., *Fundamentals of Thermal Radiation for Energy Utilization in Fuel Combustion*, Advanced Topics in Science and Technology in China 67,
https://doi.org/10.1007/978-981-19-8311-5_6

An initial academic research topic was noted on the theory and application of thermal radiation in fuel combustion based on energy utilization, which inspires academic ideas and scientific theories in related fields, as well as a foundation for subsequent studies. Future studies should focus on the following areas:

1. The combustion flue gas contains CO_2, H_2O, CO, OH, and other complex gas-phase components due to the complex combustion environment and various fuel components. Furthermore, the products contain nitrogen oxide when ammonia fuel combustion is considered. Consequently, relevant experiments and models must be performed to accurately predict the radiation characteristics of flue gas under complex combustion conditions.
2. Particle radiation is dominant in fuel combustion. Thus, the radiation characteristics of oxyfuel combustion under high concentration particle conditions should be investigated. The characteristics of high-temperature particle radiation should be experimentally measured, and a particle radiation calculation model should be developed.
3. The efficient calculation model of spectral radiation should be considered for radiative energy utilization. A WSGG model suitable for the radiation characteristics of multiple wavebands can be developed for gas media, and a database of radiation characteristics of different wavebands can be established for particles.
4. The spectral range tested by the spectrometer in the research on the radiative energy characteristics of combustion is limited due to the limitations of the current test equipment. In the future, instruments with a wider spectrum, particularly those with radiative characteristics in the infrared waveband, should be considered for experiments. The radiative energy characteristics of larger-scale combustion equipment should be considered in the future because the current experiments are on a small scale. For high-power combustion equipment (e.g., boilers), CFD simulation can be used to study the characteristics of combustion radiative energy.
5. Using micro/nanostructured materials, the spectral radiative energy can be adjusted based on the radiation characteristics of the combustion media. Consequently, future studies should focus on the coupling relationship between combustion reaction conditions and thermal radiation regulation of micro/nanostructured materials. A test bench should be built especially for the photovoltaic conversion of combustion flame radiation based on the current measurement experiment for combustion radiation energy. The micro/nanostructured emitter is used to reshape the flame spectrum to improve the photovoltaic conversion efficiency based on fuel combustion.

Appendix

New WSGG model parameters tables

The Appendix presents the new WSGG model parameters tables, which include 7 tables. Here is the introduction for them.

1. These tables list the parameters of new WSGG model for the pressure range of 1–30 bar.
2. Each table represents a molar ratio of H_2O to CO_2 (M), therefore it is suitable for many fuels with different H/C ratio.
3. The temperature range of the new WSGG model is 500–2500 K; the path-length range is 0.001–60 m; and the molar ratio range is 0.125–4.
4. The way to use the parameters of the new WSGG model for the gas mixture with different molar ratios in CFD calculation refers to Table 3.1.
5. In each table, κi represents the absorption coefficient of each gray gas, and it can be obtained through the polynomial of pressure, the polynomial coefficients are $K0$, $K1$ and $K2$. What's more, $c$ij is the temperature-dependent polynomial coefficient for emissivity, and it also can be obtained through the polynomial of pressure, the polynomial coefficients are $C0$, $C1$ and $C2$ (Tables A.1, A.2, A.3, A.4, A.5, A.6 and A.7).

S. Shan et al., *Fundamentals of Thermal Radiation for Energy Utilization in Fuel Combustion*, Advanced Topics in Science and Technology in China 67,
https://doi.org/10.1007/978-981-19-8311-5

Table A.1 $M = 0.125$

P	1–2 (bar)			2–4 (bar)		
κi	$K2$	$K1$	$K0$	$K2$	$K1$	$K0$
$\kappa 1$	− 0.01537788	0.058045024	− 0.002916791	− 0.00649336	0.047022295	− 0.016409414
$\kappa 2$	− 0.19086652	0.673880172	− 0.135713662	− 0.043453103	0.316072576	− 0.009752138
$\kappa 3$	− 1.518124622	5.507075299	− 0.051576318	− 0.180656432	1.264334888	3.084031743
$\kappa 4$	− 25.110022	95.6684858	58.8762886	− 2.018915	9.6257067	138.5974188
$c$ij	$C2$	$C1$	$C0$	$C2$	$C1$	$C0$
$c14$	− 1.16510214	3.850902068	− 1.735122558	− 0.07001639	0.205781883	1.174774809
$c13$	3.598783466	− 12.06334535	5.080530622	0.206051067	− 0.560529153	− 4.354172175
$c12$	− 3.838701366	13.08073904	− 5.125955165	− 0.239832289	0.725548162	5.188950281
$c11$	1.610416686	− 5.480776293	1.946001892	0.125094118	− 0.432411362	− 2.209437695
$c10$	− 0.236332058	0.715405465	0.096914706	− 0.023356756	0.060906654	0.554011119
$c24$	0.751288724	− 1.97829635	0.090652566	0.120040011	− 0.233857594	− 0.873230094
$c23$	− 2.528108612	6.781313752	− 0.421925566	− 0.382807164	0.658108502	3.243279142
$c22$	2.96997366	− 8.173162126	0.670769141	0.454887836	− 0.837193064	− 3.940825688
$c21$	− 1.349620506	3.833825305	− 0.549515246	− 0.230434414	0.569007029	1.503376939
$c20$	0.170544532	− 0.465564342	0.331541421	0.040754736	− 0.147913329	0.215398579
$c$ij	$C2$	$C1$	$C0$	$C2$	$C1$	$C0$
$c34$	− 0.368991106	0.678222711	0.000438325	0.001005701	− 0.400017837	0.676932193
$c33$	1.235267546	− 2.345866871	0.168094452	− 0.006525718	1.389840662	− 2.336147559
$c32$	− 1.472281114	2.937262245	− 0.430572378	− 0.005265644	− 1.59128352	2.758457272
$c31$	0.693716082	− 1.503885041	0.196174575	0.021290043	0.624967625	− 1.371826598
$c30$	− 0.07809705	0.218316101	0.160581745	− 0.007809409	− 0.033701983	0.383467346

(continued)

Table A.1 (continued)

P	1–2 (bar)			2–4 (bar)		
$c44$	0.141855152	− 0.3070343	0.030544636	− 0.021071918	0.240938875	− 0.413693435
$c43$	− 0.418354656	0.864169528	0.062856954	0.069749441	− 0.818123564	1.47502675
$c42$	0.42953348	− 0.805992798	− 0.271420584	− 0.080276321	0.99247061	− 1.829108199
$c41$	− 0.17523491	0.243555643	0.175139552	0.03780826	− 0.523861946	0.85780205
$c40$	0.022830086	0.013976331	0.021091998	− 0.006776357	0.121468098	− 0.075465765
P	4–6 (bar)			6–10 (bar)		
κi	$K2$	$K1$	$K0$	$K2$	$K1$	$K0$
$\kappa 1$	− 0.000480755	0.004357269	0.05804901	8.02281E−05	− 0.00255355	0.079318545
$\kappa 2$	− 0.001187873	0.017275237	0.509193538	0.000760164	− 0.00602093	0.578841226
$\kappa 3$	0.006232793	− 0.061247201	5.396132511	0.00377874	− 0.027338952	5.281028913
$\kappa 4$	0.20729775	− 5.58856695	163.8351094	0.168145613	− 3.335851725	151.728295
$c$ij	$C2$	$C1$	$C0$	$C2$	$C1$	$C0$
$c14$	0.011259254	− 0.275644811	1.800071297	0.028401936	− 0.455626465	2.262824648
$c13$	− 0.033069238	0.851228024	− 6.175275997	− 0.086984569	1.41745442	− 7.631682442
$c12$	0.032287923	− 0.90863385	7.371754937	0.092172604	− 1.540539555	9.007340648
$c11$	− 0.015566474	0.433637372	− 3.423063169	− 0.03928366	0.682367383	− 4.061624548
$c10$	0.006010849	− 0.123189112	0.820512509	0.006578909	− 0.12540609	0.813364226
$c24$	− 0.055223567	0.94472443	− 2.783340948	− 0.036044369	0.666482305	− 1.80433932
$c23$	0.185444271	− 3.189273463	9.540784048	0.117078266	− 2.223457898	6.207066814
$c22$	− 0.215481705	3.747513782	− 11.55374041	− 0.132546241	2.600137314	− 7.655158297
$c21$	0.097413259	− 1.699985396	5.333783871	0.058104907	− 1.166169427	3.545988702
$c20$	− 0.014353135	0.236059021	− 0.438764885	− 0.007772699	0.149857847	− 0.158453552

(continued)

Table A.1 (continued)

P	4–6 (bar)			6–10 (bar)		
$c$ij	$C2$	$C1$	$C0$	$C2$	$C1$	$C0$
$c34$	0.065396995	−0.881653541	1.573214305	0.016608526	−0.281230989	−0.272936123
$c33$	−0.217960295	2.977820712	−5.305114527	−0.056983673	0.995411958	0.794179602
$c32$	0.253555231	−3.542008127	6.4202217	0.069416849	−1.27042582	−0.580290408
$c31$	−0.114794456	1.657856207	−3.326028952	−0.033342346	0.649356055	−0.207304003
$c30$	0.013708964	−0.20287323	0.715858382	0.004027828	−0.081953822	0.338862809
$c44$	−0.025128035	0.283259619	−0.518078533	−0.003487329	0.031651568	0.212504372
$c43$	0.081848772	−0.944684676	1.787681908	0.013013248	−0.139482451	−0.565452608
$c42$	−0.094138402	1.132371585	−2.166918793	−0.017788242	0.23294359	0.481043402
$c41$	0.04491686	−0.59016151	1.009262706	0.010713886	−0.183488592	−0.199467735
$c40$	−0.008028682	0.131668981	−0.096232097	−0.002731048	0.067606151	0.097430074

P	10–20 (bar)			20–30 (bar)		
κi	$K2$	$K1$	$K0$	$K2$	$K1$	$K0$
$\kappa1$	−0.000125091	0.004341045	0.030904496	9.17268E−06	−0.000167793	0.06737584
$\kappa2$	−0.001683645	0.068346069	0.07955212	−0.000225568	0.017448805	0.514266322
$\kappa3$	−0.007249495	0.288744696	3.223015944	−0.000991486	0.066467332	5.16535961
$\kappa4$	0.012512386	0.33528269	130.5802735	−0.004987146	1.02501529	123.7854343
$c$ij	$C2$	$C1$	$C0$	$C2$	$C1$	$C0$
$c14$	−0.001088357	0.04449743	0.210614989	−0.001121325	0.06876591	−0.261567379
$c13$	0.003529165	−0.134192958	−1.166582095	0.003275513	−0.191563109	0.082281565
$c12$	−0.003550459	0.116982682	2.004424551	−0.003125212	0.168831633	0.797346905
$c11$	0.00100271	−0.019798291	−1.068604819	0.00106428	−0.049671106	−0.495776323
$c10$	1.92965E−05	−0.006348844	0.278752982	−5.94421E−05	0.000426584	0.174739886

(continued)

Table A.1 (continued)

P	10–20 (bar)			20–30 (bar)		
$c24$	−0.006635309	0.183549936	0.084078404	0.000997163	−0.090314624	2.50838062
$c23$	0.02251814	−0.645049794	−0.121001585	−0.002316524	0.240614324	−7.900418475
$c22$	−0.027368901	0.819987443	−0.371393606	0.001511372	−0.205890328	8.594052674
$c21$	0.013385715	−0.412515573	0.481369377	−0.000341438	0.073466608	−3.747412931
$c20$	−0.002037539	0.058588297	0.180725966	9.41016E−05	−0.016426886	0.828373494
$c$ij	$C2$	$C1$	$C0$	$C2$	$C1$	$C0$
$c34$	0.007120625	−0.136939272	−0.767063216	−0.001617986	0.17827464	−3.57589716
$c33$	−0.024345211	0.486646536	2.61798768	0.004081577	−0.527982974	11.53986279
$c32$	0.029911359	−0.639036467	−2.943634875	−0.00330475	0.538821729	−13.21435518
$c31$	−0.014969792	0.35076298	0.941371354	0.000848391	−0.209126227	5.811882354
$c30$	0.00243684	−0.062783163	0.306255004	−3.91602E−05	0.024770429	−0.454416622
$c44$	−0.001209687	−0.012322809	0.424483866	0.000972025	−0.102594274	1.357228718
$c43$	0.004167377	0.035936598	−1.435055924	−0.002483319	0.303763694	−4.131319522
$c42$	−0.005520728	−0.015739528	1.741123173	0.002083603	−0.313680131	4.658203015
$c41$	0.003277925	−0.027855502	−1.012202532	−0.000461543	0.116162353	−2.396772654
$c40$	−0.000793641	0.024997829	0.329772614	−0.00012914	−0.000781901	0.579566894

Table A.2 $M = 0.25$

P	1–2 (bar)			2–4 (bar)		
κi	$K2$	$K1$	$K0$	$K2$	$K1$	$K0$
$\kappa 1$	0.000260142	0.021098919	0.019706494	0.002762583	− 0.021398633	0.094691834
$\kappa 2$	− 0.03946414	0.260162628	0.134943042	0.007245418	− 0.036425582	0.541281231
$\kappa 3$	− 0.674316562	3.165876589	1.413980514	− 0.042760927	0.4049708	4.409569551
$\kappa 4$	− 17.8958798	70.8101863	65.7415113	− 0.8279821	2.2604134	134.5694663
$c$ij	$C2$	$C1$	$C0$	$C2$	$C1$	$C0$
$c14$	− 1.897774928	6.064331778	− 3.502486507	− 0.279318898	1.722102397	− 1.291851864
$c13$	5.789198448	− 18.60904741	10.19417822	0.879544036	− 5.405497313	3.425695684
$c12$	− 6.08096326	19.73553983	− 10.11829757	− 0.983711289	6.006012522	− 3.048250836
$c11$	2.49708555	− 8.170297445	3.899847524	0.439114875	− 2.619579555	1.030294444
$c10$	− 0.31347121	0.982415313	− 0.132956716	− 0.053577211	0.266382293	0.259533327
$c24$	1.048111372	− 3.000066738	1.043304609	0.110650161	− 0.210870104	− 0.785243815
$c23$	− 3.319609574	9.505174945	− 3.015865679	− 0.305555613	0.193374029	3.551520309
$c22$	3.724120102	− 10.73988929	3.032319635	0.302325313	0.283485595	− 5.327250985
$c21$	− 1.713947402	5.058396691	− 1.454377193	− 0.135506458	− 0.223506615	2.795665643
$c20$	0.24179049	− 0.736339825	0.506498954	0.015578492	0.066327827	− 0.193988355
$c$ij	$C2$	$C1$	$C0$	$C2$	$C1$	$C0$
$c34$	− 0.440464244	1.046090132	− 0.476552175	0.032276052	− 0.545105537	0.814877979
$c33$	1.464744372	− 3.450386434	1.646393482	− 0.133869834	2.060895535	− 2.981713633
$c32$	− 1.753974736	4.112109282	− 2.01758806	0.185201191	− 2.744070267	3.938067331
$c31$	0.896329718	− 2.157159381	0.920954421	− 0.089842892	1.406221941	− 2.261117783
$c30$	− 0.168009114	0.473998229	0.005833325	0.003983177	− 0.146880622	0.559621864

(continued)

Table A.2 (continued)

P	1–2 (bar)			2–4 (bar)		
$c44$	0.153686442	− 0.398951841	0.144768416	− 0.021981186	0.194861248	− 0.34018725
$c43$	− 0.453429074	1.111209221	− 0.285192791	0.078681094	− 0.706959668	1.222704318
$c42$	0.456645598	− 0.974084861	0.080216019	− 0.102716163	0.957039157	− 1.544584976
$c41$	− 0.180339844	0.234747134	0.038677374	0.058506227	− 0.597830999	0.748449356
$c40$	0.021283994	0.043755125	0.033917659	− 0.012850749	0.164804626	− 0.071642372
P	4–6 (bar)			6–10 (bar)		
κi	$K2$	$K1$	$K0$	$K2$	$K1$	$K0$
$\kappa 1$	0.000272114	− 0.003982422	0.0648745	− 0.000321852	0.009847405	0.003278311
$\kappa 2$	0.000302027	0.013514571	0.452614869	0.00415852	− 0.014894995	0.484238505
$\kappa 3$	− 0.010150446	0.157551313	4.877479809	0.025578953	− 0.26158087	6.106014537
$\kappa 4$	0.51556255	− 7.37985395	151.6338213	0.30306025	− 4.65663585	142.9445955
$c$ij	$C2$	$C1$	$C0$	$C2$	$C1$	$C0$
$c14$	0.036076735	− 0.510188909	2.590983232	− 0.011655662	0.229752409	− 0.130298384
$c13$	− 0.108096779	1.570180146	− 8.674761112	0.02125929	− 0.429179805	− 1.335419893
$c12$	0.114034125	− 1.737030073	10.35999292	− 0.003994051	0.083400904	3.686421361
$c11$	− 0.050688663	0.824022206	− 4.907255998	− 0.00651155	0.144310452	− 2.419361536
$c10$	0.010566089	− 0.175760157	1.001810339	0.002804703	− 0.061545308	0.595931123
$c24$	− 0.0610616	0.921247168	− 2.566324727	0.010156265	− 0.083751634	0.899824936
$c23$	0.203398413	− 3.127513191	8.691804773	− 0.017398909	− 0.034010007	− 1.920510739
$c22$	− 0.241882504	3.801892279	− 10.69355266	0.001575588	0.422754715	0.816781429
$c21$	0.113706719	− 1.823426973	5.207936249	0.006395753	− 0.352937325	0.24819314
$c20$	− 0.017119701	0.267017652	− 0.473576583	− 0.000365146	0.040612556	0.281690031

(continued)

Table A.2 (continued)

P	4–6 (bar)			6–10 (bar)		
$c$ij	$C2$	$C1$	$C0$	$C2$	$C1$	$C0$
$c34$	0.044992603	− 0.56995653	0.710817135	− 0.011623499	0.167250148	− 1.674243273
$c33$	− 0.153786889	1.976911377	− 2.327104121	0.031171985	− 0.409478302	5.332714522
$c32$	0.189674527	− 2.499612539	2.888663037	− 0.026788164	0.26703162	− 5.918545035
$c31$	− 0.095073311	1.304896567	− 1.772129583	0.007231877	0.008693203	2.322103836
$c30$	0.013187169	− 0.191332479	0.590165414	− 0.00116912	− 0.012519052	0.034111259
$c44$	− 0.011740914	0.100392878	− 0.126158122	0.003716837	− 0.09861323	0.511399484
$c43$	0.041321025	− 0.368389933	0.466186472	− 0.0105463	0.294449631	− 1.64362723
$c42$	− 0.054047123	0.522541079	− 0.585297294	0.009388058	− 0.2817258	1.956637452
$c41$	0.031818923	− 0.362264864	0.23318168	− 0.001237792	0.053671084	− 1.072392265
$c40$	− 0.007702265	0.119628134	0.026687852	− 0.001671755	0.044269319	0.261742394
P	10–20 (bar)			20–30 (bar)		
κi	$K2$	$K1$	$K0$	$K2$	$K1$	$K0$
$\kappa1$	− 2.49958E−05	0.001418175	0.057884953	− 5.12195E−05	0.00278336	0.041070755
$\kappa2$	− 0.001317627	0.052177218	0.361131132	− 0.001039505	0.047576588	0.341894754
$\kappa3$	− 0.002404661	0.08011011	5.487466178	− 0.000714791	0.03041448	5.805430716
$\kappa4$	0.024558908	0.33670318	120.8613394	− 0.009449128	1.63703672	108.457883
$c$ij	$C2$	$C1$	$C0$	$C2$	$C1$	$C0$
$c14$	− 0.000907456	0.018544647	0.906958579	− 0.002328164	0.087532455	0.095485681
$c13$	0.00196506	− 0.012272983	− 3.575065054	0.006696466	− 0.232354374	− 1.065999992
$c12$	− 0.000723435	− 0.061805532	4.811424145	− 0.006760405	0.206749448	1.855112595
$c11$	− 0.000737483	0.077299836	− 2.326662017	0.002735037	− 0.070274884	− 0.764175695

(continued)

Table A.2 (continued)

P	10–20 (bar)			20–30 (bar)		
$c10$	0.00040256	−0.024453117	0.465223537	−0.000364744	0.006908949	0.144903909
$c24$	−0.002978478	0.100830809	0.367474828	0.003100054	−0.183014773	3.612973652
$c23$	0.011851962	−0.405065622	−1.135041672	−0.008803162	0.529909467	−11.57249382
$c22$	−0.016551444	0.571982849	1.137203301	0.008684268	−0.537360192	13.22977935
$c21$	0.008852184	−0.303239869	−0.494424585	−0.003587363	0.231664717	−6.216697403
$c20$	−0.001332861	0.03840012	0.400585894	0.000592499	−0.043090286	1.260250042
$c$ij	$C2$	$C1$	$C0$	$C2$	$C1$	$C0$
$c34$	−0.002867315	0.134644692	−2.223807053	−0.003163743	0.214719205	−3.706726049
$c33$	0.005296042	−0.346744886	7.292974644	0.00935987	−0.681426482	12.36107518
$c32$	−0.000645763	0.267052354	−8.532992502	−0.010136041	0.792064934	−15.23713272
$c31$	−0.00232512	−0.053016598	3.894901531	0.004663705	−0.381402554	7.667090737
$c30$	0.000748898	−0.003105552	−0.251825546	−0.000719668	0.060652777	−0.93956577
$c44$	0.005583987	−0.199204644	1.330598684	0.00103023	−0.057919443	0.326397232
$c43$	−0.015544385	0.596238774	−4.161710142	−0.003301908	0.209636249	−1.326650302
$c42$	0.014286316	−0.610345727	4.753010915	0.004159883	−0.292388494	2.444439431
$c41$	−0.00466845	0.231579897	−2.508414561	−0.00215353	0.159990859	−2.082602037
$c40$	8.90769E−05	−0.007236503	0.600717422	0.000257493	−0.016896903	0.726559018

Table A.3 $M = 0.5$

P	1–2 (bar)			2–4 (bar)		
κi	$K2$	$K1$	$K0$	$K2$	$K1$	$K0$
$\kappa 1$	− 0.012077942	0.051217731	0.012658646	0.000143851	− 0.002695068	0.071597073
$\kappa 2$	0.035767828	− 0.026409718	0.455118129	0.00588544	− 0.009961336	0.541750918
$\kappa 3$	− 0.072214562	1.000638423	3.564692907	− 0.073505899	0.685452618	4.200229864
$\kappa 4$	− 11.1204224	46.3513798	72.1390752	− 0.57769135	2.52883435	117.6132419
$c$ij	$C2$	$C1$	$C0$	$C2$	$C1$	$C0$
$c14$	0.072101852	0.212168628	0.495745413	− 0.182453255	1.261179223	− 0.584055349
$c13$	− 0.176938776	− 0.98665964	− 1.867044609	0.549802055	− 3.730649005	0.713970797
$c12$	0.003702676	1.900306802	2.168912647	− 0.57323726	3.747861938	0.781562119
$c11$	0.14536603	− 1.359462281	− 0.86300561	0.231008968	− 1.391559555	− 1.141382811
$c10$	− 0.01815193	0.123133755	0.485979023	− 0.019020051	0.056660904	0.622397208
$c24$	− 0.266118058	1.102518249	− 1.796530149	0.051842024	− 0.066981477	− 0.729371022
$c23$	0.788141928	− 3.43698822	6.067914554	− 0.086526568	− 0.560959005	3.814530105
$c22$	− 0.682800412	3.381831676	− 7.149705326	− 0.013752304	1.738476516	− 6.539187441
$c21$	0.11894581	− 0.969533483	3.146113604	0.062342885	− 1.343570303	4.120598945
$c20$	0.031983916	− 0.011078278	− 0.121262161	− 0.021980506	0.302981546	− 0.533524122
$c$ij	$C2$	$C1$	$C0$	$C2$	$C1$	$C0$
c34	0.36129516	− 1.618862614	1.453941704	0.060266775	− 0.517855151	0.456040321
c33	− 1.193967318	5.464112511	− 4.841806424	− 0.244844036	2.146710819	− 2.003496167
c32	1.347066788	− 6.476488234	5.750086165	0.362130214	− 3.244253663	3.225363322
c31	− 0.549202024	2.94954013	− 2.894957554	− 0.217452853	2.007261478	− 2.337396937
c30	0.016263632	− 0.223430408	0.568381602	0.035072757	− 0.341890379	0.730065047

(continued)

Table A.3 (continued)

P	1–2 (bar)			2–4 (bar)		
c44	− 0.038176376	0.192668602	− 0.290474834	− 0.019022957	0.094740985	− 0.171233276
c43	0.165956106	− 0.813482201	1.099037011	0.076640575	− 0.427675415	0.684685563
c42	− 0.252024918	1.276439675	− 1.477501611	− 0.117686769	0.748586139	− 0.959147135
c41	0.157947936	− 0.898993938	0.77471381	0.081313359	− 0.613202206	0.509668654
c40	− 0.03501642	0.258271372	− 0.09428591	− 0.021050591	0.20765052	− 0.048907522

P	4–6 (bar)			6–10 (bar)		
κi	$K2$	$K1$	$K0$	$K2$	$K1$	$K0$
$\kappa 1$	0.000397181	− 0.004409217	0.074400389	5.33191E−05	− 4.20723E−05	0.060576533
$\kappa 2$	− 0.001865998	0.045938145	0.44217599	− 0.00242865	0.052585224	0.422548988
$\kappa 3$	− 0.028656295	0.328082628	4.912116166	− 0.004414892	0.032020864	5.81579623
$\kappa 4$	0.3809067	− 4.4592859	130.2281541	0.174125725	− 1.95866445	122.6685405
$c$ij	$C2$	$C1$	$C0$	$C2$	$C1$	$C0$
$c14$	0.019591928	− 0.265010089	2.287978977	0.004919592	− 0.175657808	2.280069366
$c13$	− 0.061848435	0.924484768	− 8.120156455	− 0.0197488	0.672908402	− 8.126285122
$c12$	0.073633703	− 1.223525872	10.31717796	0.029937763	− 0.960229649	10.31045446
$c11$	− 0.040131678	0.719844354	− 5.248748127	− 0.019384347	0.579997563	− 5.156571303
$c10$	0.009829313	− 0.174414635	1.085109552	0.004499026	− 0.125215362	0.981804228
$c24$	− 0.032449834	0.631704295	− 2.175444392	− 0.035691288	0.751370504	− 2.776749308
$c23$	0.124014896	− 2.354068402	7.618304285	0.121341329	− 2.555663966	8.924126078
$c22$	− 0.171137343	3.167611044	− 9.737564919	− 0.150480646	3.159642079	− 10.43339224
$c21$	0.094110618	− 1.704408402	5.055667613	0.077695963	− 1.6105904	5.083687178
$c20$	− 0.01673199	0.283847066	− 0.540962452	− 0.013345557	0.258730739	− 0.512176081

(continued)

Table A.3 (continued)

P	4–6 (bar)			6–10 (bar)		
$c$ij	$C2$	$C1$	$C0$	$C2$	$C1$	$C0$
c34	0.008573392	−0.178994695	−0.072307385	0.026887254	−0.446343797	0.872488201
c33	−0.044725821	0.782856492	0.250029695	−0.091087218	1.481354351	−2.271947155
c32	0.08030118	−1.265334252	−0.181049788	0.114019003	−1.821228055	1.940471414
c31	−0.056675991	0.856068461	−0.305054657	−0.06192193	0.986987577	−0.901715531
c30	0.0113222	−0.171520267	0.428593507	0.011905007	−0.189665729	0.516485215
c44	0.000496379	−0.04302132	0.067506568	−0.003042491	0.007625321	−0.108973964
c43	0.003377236	0.100756959	−0.256830499	0.010407049	−0.005586987	0.128159882
c42	−0.01463254	−0.009010189	0.422370503	−0.014380332	0.007641631	0.313380119
c41	0.017625493	−0.137727147	−0.373225726	0.010472635	−0.058327526	−0.592120552
c40	−0.007098197	0.102289412	0.1492986	−0.003786068	0.063007497	0.265753461

P	10–20 (bar)			20–30 (bar)		
κi	$K2$	$K1$	$K0$	$K2$	$K1$	$K0$
$\kappa 1$	−0.000154714	0.005953598	0.021423143	−9.07636E−06	0.000738998	0.067460095
$\kappa 2$	−0.001068267	0.032501215	0.487350858	0.000176	−0.012489443	0.889457096
$\kappa 3$	0.002436474	−0.079309611	6.243964451	0.00102276	−0.018699699	5.597251625
$\kappa 4$	0.011847972	1.38047986	105.5048727	−0.014557454	2.36441129	96.3884145
$c$ij	$C2$	$C1$	$C0$	$C2$	$C1$	$C0$
$c14$	−0.003742753	0.067247136	0.717254487	0.000360608	−0.050310614	1.427064935
$c13$	0.009693172	−0.124891953	−3.092478768	−0.00137968	0.184171066	−4.844598452
$c12$	−0.00769628	0.011129425	4.360267975	0.002010475	−0.24479111	5.595976783
$c11$	0.001677319	0.06414347	−2.104196946	−0.001164654	0.126063734	−2.20581289

(continued)

Table A.3 (continued)

P	10–20 (bar)			20–30 (bar)		
$c10$	7.25994E−05	−0.021891474	0.391208022	0.000228333	−0.021420696	0.319499012
$c24$	0.002076483	−0.007923042	1.039409101	−0.000860365	0.049535938	1.064968585
$c23$	−0.002751003	−0.091690145	−3.30637897	0.002423661	−0.124877515	−4.712497206
$c22$	−0.002284887	0.261897785	3.724474882	−0.002115575	0.080698975	7.280725976
$c21$	0.003600216	−0.18821585	−1.730483647	0.000488161	0.008603459	−4.422047783
$c20$	−0.000428204	0.015295754	0.630438523	0.000142958	−0.019041553	1.088719793
$c$ij	$C2$	$C1$	$C0$	$C2$	$C1$	$C0$
c34	−0.014044984	0.350889691	−3.006622885	0.00127182	−0.034159866	−1.432353479
c33	0.039783334	−1.018218045	9.636721619	−0.002688274	0.001626895	6.228465747
c32	−0.037455841	1.000523135	−11.12955614	0.000927798	0.163735479	−9.747258712
c31	0.013746173	−0.387873668	5.28008664	0.000659721	−0.160549845	5.968191016
c30	−0.00183258	0.055416851	−0.560581933	−0.00030421	0.038516541	−0.833923567
c44	0.012596403	−0.318020533	1.583595155	−0.000738291	0.029275188	−0.028441657
c43	−0.037630727	0.972268084	−4.846613208	0.001604324	−0.039441919	−0.306433404
c42	0.038445776	−1.031237201	5.419557614	−0.000695819	−0.039847238	1.248396584
c41	−0.015684523	0.437460358	−2.934283646	−0.000195234	0.0594897	−1.570586132
c40	0.001793206	−0.041923633	0.757137341	−1.87122E−05	−0.00421159	0.727663829

Table A.4 $M = 0.75$

P	1–2 (bar)			2–4 (bar)		
κi	$K2$	$K1$	$K0$	$K2$	$K1$	$K0$
$\kappa 1$	− 0.014676706	0.057219031	0.010379033	0.00062775	− 0.005547543	0.074694357
$\kappa 2$	0.044231636	− 0.057168886	0.489107698	0.002865826	0.016561939	0.507109291
$\kappa 3$	− 0.061263582	0.997952669	3.610363064	− 0.102597952	0.881421592	4.008762698
$\kappa 4$	− 16.27600622	58.56955557	55.84487414	1.38961895	− 6.07626245	114.4740095
$c$ij	$C2$	$C1$	$C0$	$C2$	$C1$	$C0$
$c14$	− 0.134374948	1.075074122	− 0.203617617	− 0.19555829	1.318724949	− 0.446185906
$c13$	0.549739892	− 3.877877616	0.363828107	0.629837277	− 4.127972131	0.5436276
$c12$	− 0.902386508	5.291493432	− 0.263309992	− 0.713045896	4.463101086	0.636112252
$c11$	0.624832278	− 3.033539275	0.232752765	0.32280397	− 1.86631316	− 0.893586233
$c10$	− 0.1035341	0.403962948	0.305476265	− 0.038453289	0.161353888	0.53037114
$c24$	− 0.113642934	0.478719625	− 1.227911341	0.099437573	− 0.33624188	− 0.450310356
$c23$	0.3120071	− 1.600413924	4.403336192	− 0.26587031	0.46842419	2.577169601
$c22$	− 0.153635668	1.565443186	− 5.571011018	0.22028786	0.394544575	− 4.724907908
$c21$	− 0.145377536	− 0.227243568	2.620464287	− 0.061408541	− 0.647179572	3.124460312
$c20$	0.090238864	− 0.152360084	− 0.054834548	− 0.00023561	0.182432509	− 0.362521839
$c$ij	$C2$	$C1$	$C0$	$C2$	$C1$	$C0$
c34	0.402032766	− 1.650060295	1.370769812	0.025516366	− 0.263976027	0.104666877
c33	− 1.353282952	5.722641236	− 4.670575543	− 0.124590002	1.245893332	− 0.631851535
c32	1.568086648	− 7.044800566	5.731355735	0.221635964	− 2.162567726	1.352692792
c31	− 0.667177822	3.393261605	− 3.025640916	− 0.156622084	1.529461017	− 1.340262695
c30	0.028107606	− 0.307608799	0.626689288	0.028737777	− 0.294316751	0.597584509

(continued)

Table A.4 (continued)

P	1–2 (bar)			2–4 (bar)		
c44	−0.072742674	0.233278803	−0.28964452	−0.007749321	−0.002196468	−0.078667393
c43	0.28364328	−0.982148764	1.110638138	0.039843189	−0.093576464	0.308693902
c42	−0.39387718	1.531563576	−1.503327308	−0.07883744	0.361320216	−0.422999548
c41	0.229499034	−1.073240047	0.792391643	0.068336597	−0.454271925	0.199105148
c40	−0.047254642	0.304635067	−0.099452743	−0.021124787	0.198489767	0.008318436
P	4–6 (bar)			6–10 (bar)		
κi	$K2$	$K1$	$K0$	$K2$	$K1$	$K0$
$\kappa 1$	−0.003443947	0.038902986	−0.037960613	−0.000538632	0.009844493	0.031799005
$\kappa 2$	−0.033859347	0.41665052	−0.505642281	−0.01208437	0.209707356	−0.047882442
$\kappa 3$	−0.166645989	1.890247779	0.998226542	−0.026535328	0.361340696	5.127685238
$\kappa 4$	0.13146615	−0.29048485	111.4613439	0.074447313	0.284628175	110.0633439
$c$ij	$C2$	$C1$	$C0$	$C2$	$C1$	$C0$
$c14$	0.032913547	−0.478950722	3.088967402	−0.019987898	0.266398045	0.521326805
$c13$	−0.096295294	1.516140858	−10.41470324	0.055120299	−0.640322051	−2.926887103
$c12$	0.107382318	−1.836812637	12.70891572	−0.051760042	0.452402646	4.702748964
$c11$	−0.058641784	1.03730788	−6.404938329	0.016803376	−0.040298405	−2.655326358
$c10$	0.010307842	−0.19631606	1.180872848	−0.000899667	−0.032722403	0.602781218
$c24$	0.004881252	0.268764138	−1.357433308	−0.006123281	0.30594416	−1.184350252
$c23$	−0.000611471	−1.13821429	4.759582107	0.038646356	−1.330167409	4.49801904
$c22$	−0.032098422	1.81956389	−6.386804662	−0.069473201	1.978644304	−5.995795069
$c21$	0.043466713	−1.238470683	3.811620702	0.04645599	−1.16399738	3.257166924
$c20$	−0.013975873	0.269908619	−0.492582065	−0.010164551	0.215866278	−0.305535608

(continued)

Table A.4 (continued)

P	4–6 (bar)			6–10 (bar)		
$c$ij	$C2$	$C1$	$C0$	$C2$	$C1$	$C0$
c34	−0.044426239	0.366853394	−1.299569133	0.016887715	−0.357731324	0.840636822
c33	0.098278334	−0.681199401	3.510626021	−0.070553342	1.36946698	−2.71543192
c32	−0.040998777	−0.034630162	−2.956901614	0.102824342	−1.861373156	2.825924075
c31	−0.027856712	0.573022923	0.425243733	−0.061592247	1.063931472	−1.305728307
c30	0.017420967	−0.243799642	0.576585033	0.01350625	−0.224909043	0.604171239
c44	0.014146133	−0.178802548	0.277429679	−0.002450877	0.025448854	−0.350586403
c43	−0.030824237	0.443660667	−0.709575812	0.01026671	−0.081689917	0.963253606
c42	0.008786455	−0.252335805	0.629642222	−0.015863455	0.100686506	−0.601094911
c41	0.016358647	−0.113169415	−0.333657692	0.011665602	−0.093772887	−0.281087243
c40	−0.008256228	0.110594683	0.154001828	−0.003995814	0.066057268	0.267851441
P	10–20 (bar)			20–30 (bar)		
κi	$K2$	$K1$	$K0$	$K2$	$K1$	$K0$
$\kappa 1$	−2.8331E−06	0.000564298	0.07102111	4.2926E−05	−0.001580959	0.095622584
$\kappa 2$	0.001942331	−0.073806691	1.384587938	0.00176858	−0.081342694	1.604808182
$\kappa 3$	0.012392946	−0.407899129	8.927256113	0.004676879	−0.161285777	7.081416023
$\kappa 4$	0.018036914	1.47273743	103.8232912	−0.009041962	2.35504697	97.0086508
$c$ij	$C2$	$C1$	$C0$	$C2$	$C1$	$C0$
$c14$	0.005049134	−0.234075495	3.022358992	0.003134377	−0.180284291	2.712437936
$c13$	−0.017500697	0.81105287	−10.17853674	−0.010506594	0.608471757	−8.924555694
$c12$	0.021960458	−1.011823899	11.97296449	0.012391884	−0.720998255	9.983880961
$c11$	−0.011378759	0.512774788	−5.367844811	−0.005673377	0.328577306	−3.966048071

(continued)

Table A.4 (continued)

P	10–20 (bar)			20–30 (bar)		
$c10$	0.002057426	− 0.089419883	0.874046664	0.000879817	− 0.049801447	0.55272176
$c24$	− 0.005687279	0.253203147	− 0.700540262	− 0.0029138	0.156637239	0.121386364
$c23$	0.020889532	− 0.875872017	1.730747567	0.00768008	− 0.396911659	− 2.564 678859
$c22$	− 0.027286805	1.070007257	− 1.128064219	− 0.006530444	0.304373703	5.882062259
$c21$	0.014261393	− 0.51751916	0.011844366	0.001822904	− 0.055029814	− 4.262546992
$c20$	− 0.001696097	0.051266625	0.493615512	4.62904E−05	− 0.014639635	1.114785748
$c$ij	$C2$	$C1$	$C0$	$C2$	$C1$	$C0$
c34	0.000312437	− 0.080090742	− 0.278241209	0.001911608	− 0.058698357	− 1.345757265
c33	− 0.00335052	0.268947269	1.569482919	− 0.00340132	0.019901936	6.570709643
c32	0.008310177	− 0.342917703	− 2.907214	0.000237325	0.211991548	− 10.77625801
c31	− 0.006758912	0.1972682	1.877570937	0.001429062	− 0.206428601	6.676317627
c30	0.001152231	− 0.025453145	− 0.15498585	− 0.000474059	0.048357572	− 0.980684342
c44	0.001902201	− 0.002068572	− 0.510719862	− 0.001678396	0.056560342	− 0.251059634
c43	− 0.004887969	− 0.001705488	1.678877245	0.004439425	− 0.126070794	0.435225569
c42	0.0026503	0.035508712	− 1.800692423	− 0.003610392	0.051899155	0.375775583
c41	0.000808356	− 0.050836043	0.375268919	0.001014392	0.022292152	− 1.169709457
c40	− 0.000981876	0.03939189	0.233111394	− 0.000220865	0.001627853	0.683987634

Table A.5 $M = 1$

P	1–2 (bar)			2–4 (bar)		
κi	$K2$	$K1$	$K0$	$K2$	$K1$	$K0$
$\kappa 1$	− 0.023790214	0.081448825	− 0.002443296	0.000864595	− 0.00648264	0.074800399
$\kappa 2$	− 0.098932084	0.366457306	0.21847772	0.000731319	0.035172062	0.482394599
$\kappa 3$	− 0.410099882	2.057737171	2.944584676	− 0.117809229	0.973859027	3.943178351
$\kappa 4$	− 9.89783392	42.34449532	59.57355714	− 0.83068445	6.92563965	94.1426706
$c$ij	$C2$	$C1$	$C0$	$C2$	$C1$	$C0$
$c14$	0.146388406	0.370016121	0.217756312	− 0.133781409	0.91945684	0.239554131
$c13$	− 0.083120074	− 2.421659879	− 0.443538656	0.473798549	− 3.083571614	− 1.347389678
$c12$	− 0.485981366	4.521505523	0.085494128	− 0.589052013	3.567226694	2.406334374
$c11$	0.55684035	− 3.031216099	0.281589319	0.291446386	− 1.589363583	− 1.540539857
$c10$	− 0.132370278	0.519086447	0.218241077	− 0.037742568	0.142323742	0.593255647
$c24$	0.21711866	− 0.580025964	− 0.454280171	0.079427312	− 0.189851541	− 0.683863625
$c23$	− 0.9647052	2.383235586	1.516783791	− 0.24753457	0.277513938	2.859544568
$c22$	1.529733352	− 3.54582877	− 1.920137248	0.254529042	0.287916284	− 4.486810116
$c21$	− 1.00260602	2.293561238	0.881870488	− 0.104030225	− 0.453293838	2.78127746
$c20$	0.226845976	− 0.539168934	0.192609708	0.010886816	0.128406199	− 0.278703918
$c$ij	$C2$	$C1$	$C0$	$C2$	$C1$	$C0$
c34	− 0.320809314	0.556659211	− 0.147289776	0.002172357	− 0.104710652	− 0.116476734
c33	0.958765864	− 1.300978382	0.194782685	− 0.020973842	0.541639001	0.428506742
c32	− 1.036536552	0.796693448	0.246518783	0.071137741	− 1.143489416	− 0.303812661
c31	0.507634118	− 0.076728817	− 0.576484461	− 0.072739954	0.971597734	− 0.351641276
c30	− 0.1158029	0.096535014	0.348535756	0.014396399	− 0.205640983	0.432090554

(continued)

Table A.5 (continued)

P	1–2 (bar)			2–4 (bar)		
c44	0.070811472	− 0.218817618	0.004914189	0.005102343	− 0.096639488	0.023394446
c43	− 0.152556946	0.392254183	0.200578808	− 0.005923639	0.248867375	− 0.099180804
c42	0.072046946	0.067666065	− 0.499320111	− 0.022920105	− 0.068803075	0.153486373
c41	0.03046821	− 0.460064381	0.34012591	0.041850991	− 0.24367071	− 0.138192556
c40	− 0.02140395	0.232963461	− 0.036096688	− 0.017440017	0.16999617	0.073982161
P	4–6 (bar)			6–10 (bar)		
κi	$K2$	$K1$	$K0$	$K2$	$K1$	$K0$
$\kappa 1$	0.000238154	− 0.001346511	0.064278933	0.000773065	− 0.009479518	0.09382017
$\kappa 2$	− 0.005234965	0.07968439	0.399805821	0.001988691	− 0.019542808	0.735117387
$\kappa 3$	− 0.034487099	0.324420911	5.207776735	0.013275033	− 0.267582809	7.040362339
$\kappa 4$	0.15579985	− 0.33681325	107.4087334	0.104081775	0.38447265	104.9428687
$c$ij	$C2$	$C1$	$C0$	$C2$	$C1$	$C0$
$c14$	− 0.080977915	0.663774627	0.417427083	0.049990866	− 0.906581194	5.124685923
$c13$	0.231843366	− 1.733723964	− 2.87549735	− 0.154447539	2.878295743	− 16.641143
$c12$	− 0.218180015	1.335731611	5.398362732	0.170901473	− 3.291830418	19.15680136
$c11$	0.072282242	− 0.216939069	− 3.523611609	− 0.079918311	1.586894975	− 8.867395968
$c10$	− 0.004105258	− 0.06473366	0.883288285	0.013536688	− 0.273914405	1.503262732
$c24$	0.042091283	− 0.048378398	− 0.652379727	− 0.064589175	1.218702322	− 4.414367589
$c23$	− 0.093730746	− 0.381772087	3.035827478	0.203092676	− 3.889011426	13.39362032
$c22$	0.045712076	1.22385872	− 4.88950841	− 0.226120229	4.402233589	− 14.17379461
$c21$	0.01111101	− 0.982024242	3.053939322	0.102785744	− 2.028810925	6.034368984
$c20$	− 0.006969352	0.201711195	− 0.286225214	− 0.015244214	0.290579401	− 0.521539409

(continued)

Table A.5 (continued)

P	4–6 (bar)			6–10 (bar)		
$c$ij	$C2$	$C1$	$C0$	$C2$	$C1$	$C0$
c34	−0.047927145	0.366917729	−1.201398232	0.012209955	−0.294232916	0.600570065
c33	0.125436003	−0.892203379	3.821318754	−0.030012775	0.763656649	−0.517685409
c32	−0.097831366	0.549222591	−4.371154983	0.022614324	−0.629803549	−1.633042971
c31	0.016662866	0.071226063	1.819400304	−0.005968403	0.199350888	1.865377023
c30	0.002813026	−0.075236234	0.095805526	0.000230625	−0.016812407	−0.161771009
c44	0.019972758	−0.228112784	0.311360984	0.020367111	−0.292116777	0.681188246
c43	−0.057986934	0.710584548	−1.113036776	−0.070648248	1.056976776	−2.735582834
c42	0.053172885	−0.733281052	1.593910447	0.08747822	−1.374184225	4.204337395
c41	−0.011874617	0.213461066	−1.107109932	−0.043536602	0.707455132	−2.93124288
c40	−0.003625715	0.0549717	0.313051215	0.005826392	−0.078500879	0.773610849

P	10–20 (bar)			20–30 (bar)		
κi	$K2$	$K1$	$K0$	$K2$	$K1$	$K0$
$\kappa 1$	−5.56771E−05	0.002310565	0.058793577	1.5392E−07	0.000319963	0.076273201
$\kappa 2$	−0.000519208	0.009334063	0.697138555	0.000223124	−0.012305972	0.833006573
$\kappa 3$	0.003023592	−0.07551552	6.144833522	0.000169144	0.046913711	4.838028
$\kappa 4$	−0.013640226	2.74666855	93.0931098	−0.025541464	3.20089478	88.7690804
$c$ij	$C2$	$C1$	$C0$	$C2$	$C1$	$C0$
$c14$	0.004955115	−0.233379193	2.896240981	0.000580094	−0.06604851	1.299635767
$c13$	−0.016184009	0.773432495	−9.41886355	−0.002224971	0.237919989	−4.292228618
$c12$	0.01942333	−0.930068047	10.68699196	0.003038252	−0.300492814	4.649518347
$c11$	−0.009857563	0.459708327	−4.601604253	−0.001574029	0.142363049	−1.568112201

(continued)

Table A.5 (continued)

P	10–20 (bar)			20–30 (bar)		
$c10$	0.001707404	− 0.076623656	0.713283564	0.000262172	− 0.0213696	0.186295292
$c24$	− 0.01084288	0.431888009	− 1.920853879	− 0.000534682	0.015631432	2.280998461
$c23$	0.036580348	− 1.410836646	5.263105328	0.001127219	0.000416312	− 8.780702192
$c22$	− 0.044154326	1.630650863	− 4.65455767	− 0.000463029	− 0.07846768	12.05129407
$c21$	0.021836235	− 0.760185961	1.443070224	− 0.000321149	0.089921418	− 6.696123616
$c20$	− 0.003223401	0.099731241	0.184860821	0.000237772	− 0.030370395	1.402424647
$c$ij	$C2$	$C1$	$C0$	$C2$	$C1$	$C0$
c34	0.007876178	− 0.29930899	1.084708436	8.7634E−05	0.065146121	− 3.088976014
c33	− 0.025937234	0.923443247	− 2.523105561	0.001050728	− 0.306099011	11.272555
c32	0.032202397	− 1.031080724	1.420921519	− 0.003209309	0.500359866	− 15.04320798
c31	− 0.017106779	0.488835188	0.084371554	0.00254401	− 0.315023451	8.301229018
c30	0.003039747	− 0.079184308	0.18103585	− 0.000582152	0.062023547	− 1.194361692
c44	− 0.000114039	0.027984724	− 0.471711776	− 0.00037681	− 0.012370531	0.440501738
c43	− 0.000106282	− 0.056040028	1.340388609	0.000648867	0.075558773	− 1.593647249
c42	− 0.001044729	0.052839093	− 1.213600829	0.000278281	− 0.156220228	2.438381437
c41	0.001765722	− 0.036375504	− 0.023168927	− 0.000703969	0.114872766	− 2.060257637
c40	− 0.000961803	0.030963588	0.357785611	0.000106364	− 0.015763113	0.865052989

Table A.6 $M = 2$

P	1–2 (bar)			2–4 (bar)		
κi	$K2$	$K1$	$K0$	$K2$	$K1$	$K0$
$\kappa 1$	0.004183992	− 0.010373304	0.068147347	0.001049754	− 0.006308614	0.072554919
$\kappa 2$	0.101532064	− 0.24119527	0.650404666	− 0.003164009	0.06265385	0.461490718
$\kappa 3$	0.28644159	− 0.021764799	4.391868256	− 0.136045831	1.04745419	3.943379962
$\kappa 4$	8.0948341	− 15.57011057	75.08422843	− 0.512054615	5.649844395	67.07187336
$c$ij	$C2$	$C1$	$C0$	$C2$	$C1$	$C0$
$c14$	− 1.243515114	4.952590649	− 3.230723556	− 0.16596521	1.125891931	0.112474264
$c13$	4.024870484	− 16.03976646	9.80373301	0.547003288	− 3.494118478	− 1.376094169
$c12$	− 4.646282902	18.38733328	− 10.31072653	− 0.619241648	3.61377363	3.128227747
$c11$	2.213411654	− 8.583966607	4.398299147	0.27025991	− 1.344376897	− 2.308273297
$c10$	− 0.312189098	1.141064195	− 0.251363117	− 0.028771924	0.064988686	0.767119204
$c24$	1.022651866	− 3.552667663	2.072909162	0.041428824	0.103572986	− 1.314679965
$c23$	− 3.034288688	10.26320718	− 5.451248065	− 0.082650091	− 0.944047166	5.156706239
$c22$	3.092021234	− 9.902423135	4.144747873	0.00323339	2.096348852	− 7.497644722
$c21$	− 1.283581888	3.74565114	− 0.781372714	0.055065157	− 1.583956059	4.523253504
$c20$	0.170701212	− 0.428002848	0.172432498	− 0.021821394	0.357434561	− 0.628351897
$c$ij	$C2$	$C1$	$C0$	$C2$	$C1$	$C0$
c34	− 0.169652676	0.491749416	− 0.359970633	0.141233332	− 1.156649576	1.693283319
c33	0.442677898	− 0.933503277	0.796605744	− 0.479159192	3.994202978	− 5.371458409
c32	− 0.280246772	− 0.272482378	− 0.053479685	0.610477647	− 5.191630272	6.221918426
c31	− 0.028079824	1.103029518	− 0.868840988	− 0.342844492	3.002659825	− 3.409042933
c30	0.003524402	− 0.235812241	0.513453948	0.062865637	− 0.579002806	0.962470141

(continued)

Table A.6 (continued)

P	1–2 (bar)			2–4 (bar)		
c44	− 0.091987818	0.273735321	− 0.45756688	− 0.095294195	0.686830899	− 1.270532531
c43	0.22100344	− 0.746942528	1.371797813	0.310391434	− 2.237985249	3.996331278
c42	− 0.185834346	0.871602241	− 1.444010654	− 0.377593742	2.741791606	− 4.417351799
c41	0.104545042	− 0.713569443	0.632332312	0.209376196	− 1.586168718	1.958206249
c40	− 0.050658366	0.339474539	− 0.102051908	− 0.045555111	0.404294299	− 0.252104451
P	4–6 (bar)			6–10 (bar)		
κi	$K2$	$K1$	$K0$	$K2$	$K1$	$K0$
κ1	0.003229656	− 0.027415647	0.122104619	− 0.000129145	0.00344049	0.057884645
κ2	0.009640626	− 0.061216963	0.752099816	− 0.002559335	0.035605164	0.610365626
κ3	0.012599525	− 0.154471002	6.372755034	0.010755696	− 0.234382942	6.918604503
κ4	0.162621135	0.551197145	76.67165036	0.024912611	1.913612077	73.45466762
$c$ij	$C2$	$C1$	$C0$	$C2$	$C1$	$C0$
c14	0.02669609	− 0.441609632	3.299899722	− 0.01422528	0.005744987	2.088941304
c13	− 0.117315195	1.863738417	− 12.17842603	0.032213453	0.257625943	− 7.924782496
c12	0.17056835	− 2.695273977	15.72745821	− 0.019433268	− 0.651505371	10.30490483
c11	− 0.100463191	1.589277096	− 8.111319659	4.64254E−05	0.484419147	− 5.100518141
c10	0.021670644	− 0.335037148	1.560141458	0.00156096	− 0.107475564	0.918720567
c24	− 0.056369945	0.964141807	− 3.192174961	− 0.00235737	0.329601947	− 1.329388501
c23	0.214602924	− 3.566095004	10.88884936	0.017885091	− 1.244044355	4.038387442
c22	− 0.287728588	4.694839548	− 13.23621587	− 0.033364931	1.636750238	− 4.044771639
c21	0.15548982	− 2.513976583	6.636540992	0.021027002	− 0.840593775	1.436905595
c20	− 0.028218215	0.433015093	− 0.828324889	− 0.002806725	0.10511875	0.224239553
$c$ij	$C2$	$C1$	$C0$	$C2$	$C1$	$C0$

(continued)

Table A.6 (continued)

P	4–6 (bar)			6–10 (bar)		
c34	0.032544213	−0.37615633	0.310336239	−0.017045536	0.240182897	−1.602468165
c33	−0.138362465	1.563266795	−1.100461299	0.05712493	−0.887834189	6.568598385
c32	0.214377966	−2.387283764	1.342127302	−0.069085463	1.20605937	−10.01324806
c31	−0.144522636	1.616689565	−1.038311585	0.034705464	−0.676222494	6.26694919
c30	0.033221284	−0.379034873	0.636908053	− 0.00613553	0.132671745	−1.016486384
c44	−0.036416871	0.2284234	−0.378939715	0.01769543	−0.348211345	1.132825919
c43	0.1368212	−0.907812765	1.452765098	−0.061672751	1.253366932	−4.368530854
c42	−0.190462497	1.346845869	−1.831668777	0.077428247	−1.640951928	6.451051206
c41	0.119726628	−0.946690511	0.834686499	−0.039401526	0.874140442	−4.361685669
c40	−0.030447881	0.304147717	−0.093233799	0.005271656	−0.114538519	1.132980309
P	10–20 (bar)			20–30 (bar)		
κi	$K2$	$K1$	$K0$	$K2$	$K1$	$K0$
$\kappa 1$	−0.000010079	0.001001522	0.070367699	2.57969E−05	−0.000357954	0.083206865
$\kappa 2$	0.000828472	−0.026928953	0.896926105	−0.000395133	0.030226761	0.243253987
$\kappa 3$	0.003537674	−0.049388345	5.790460822	−0.003070793	0.241284234	2.620395694
$\kappa 4$	−0.50529203	20.3083014	−57.47176148	−0.040760788	4.1546312	79.7891458
$c$ij	$C2$	$C1$	$C0$	$C2$	$C1$	$C0$
$c14$	0.005272638	−0.24209429	2.617542346	0.000628086	−0.058704422	0.807565716
$c13$	−0.017368005	0.80555887	−8.445966029	−0.002341971	0.208471598	−2.514634025
$c12$	0.020354739	−0.948268855	9.29373891	0.003089189	−0.259682365	2.428229084
$c11$	−0.009697269	0.444470067	−3.726657912	−0.001567579	0.121946735	−0.528067406
$c10$	0.001544399	−0.068614479	0.531765809	0.000249194	−0.017662988	0.030818074

(continued)

Table A.6 (continued)

P	10–20 (bar)			20–30 (bar)		
$c24$	−0.024801485	0.851982883	−4.308786366	−0.001195783	0.049113904	2.306312502
$c23$	0.076612665	−2.605336006	11.77854649	0.003354906	−0.111085754	−8.80335485
$c22$	−0.082157704	2.742478323	−10.22277525	−0.002851596	0.042432626	12.05569561
$c21$	0.035044699	−1.129153506	2.920733202	0.00055274	0.043720175	−6.739957044
$c20$	−0.004637515	0.13657211	0.092784945	9.48019E−05	−0.021833527	1.367970879
$c$ij	$C2$	$C1$	$C0$	$C2$	$C1$	$C0$
c34	0.033698663	−1.069654245	6.421483327	−0.013745414	0.677485429	−9.543679249
c33	−0.10310669	3.228997716	−18.57655868	0.046287167	−2.31102843	32.46642159
c32	0.109869763	−3.343633889	17.58816186	−0.056933413	2.882857193	−40.22038919
c31	−0.046910789	1.361134376	−5.944994268	0.029860015	−1.53083095	21.18599073
c30	0.006589173	−0.178609938	0.823860199	−0.005497989	0.281494005	−3.543353951
c44	−0.014619884	0.458520277	−3.702958887	0.014217524	−0.672233015	7.377143959
c43	0.044681395	−1.395777107	11.48749491	−0.047277637	2.246992034	−24.58427511
c42	−0.047743582	1.455667037	−11.99795553	0.057150227	−2.735096147	29.85978468
c41	0.020489745	−0.594428938	4.334881025	−0.029348693	1.415510895	−15.92854058
c40	−0.003256268	0.095838635	−0.117998837	0.005248798	−0.250182773	3.400402971

Table A.7 $M = 4$

P	1–2			2–4		
κi	$K2$	$K1$	$K0$	$K2$	$K1$	$K0$
$\kappa 1$	− 0.0118807	0.046532356	0.018045543	0.000754349	− 0.003475325	0.06752071
$\kappa 2$	0.016125356	0.065470566	0.394837816	− 0.007466612	0.086330646	0.447485527
$\kappa 3$	− 1.416839776	5.792356922	− 0.383808258	− 0.141469638	1.048119719	4.003185597
$\kappa 4$	− 26.39996476	100.6233201	− 27.1921835	− 0.89447472	9.80541848	52.42165954
$c$ij	$C2$	$C1$	$C0$	$C2$	$C1$	$C0$
$c14$	− 0.361394306	1.899480863	− 0.579049571	− 0.220416154	1.497825229	− 0.339650914
$c13$	1.292774778	− 6.574744127	1.54464316	0.701108077	− 4.520110356	− 0.197957579
$c12$	− 1.650468142	7.991516215	− 1.18528327	− 0.76368654	4.53672888	2.177164989
$c11$	0.879092358	− 3.947963937	0.293455506	0.321411648	− 1.647388273	− 2.076972979
$c10$	− 0.124607614	0.494250895	0.321309732	− 0.035814185	0.103367952	0.747901899
$c24$	− 0.106869686	0.281809353	− 1.101283986	0.103422307	− 0.327830563	− 0.723172126
$c23$	0.275276188	− 0.954798952	3.744270311	− 0.263075707	0.316857359	3.354365269
$c22$	− 0.208410976	1.271623902	− 4.888539825	0.17996892	0.856379971	− 5.611571547
$c21$	0.01913329	− 0.671570019	2.749736151	− 0.011633992	− 1.123019209	3.775703659
$c20$	0.006765944	0.125801296	− 0.269812754	− 0.012641271	0.296651647	− 0.533884597
$c$ij	$C2$	$C1$	$C0$	$C2$	$C1$	$C0$
c34	1.212447928	− 4.276503486	3.59044676	0.114052604	− 0.785317125	1.001655337
c33	− 3.896163398	13.94028924	− 11.31184997	− 0.408054214	2.885346145	− 3.15440051
c32	4.371944412	− 16.10193081	12.47918026	0.554057703	− 4.05684856	3.660562599
c31	− 1.930912478	7.533934773	− 5.708099259	− 0.331516476	2.555029124	− 2.147871972
c30	0.2068702	− 0.928642764	0.985055123	0.065144754	− 0.535438972	0.765549326

(continued)

Table A.7 (continued)

P	1–2			2–4		
c44	− 0.784929254	2.720486059	− 2.501760427	− 0.108405251	0.598221992	− 0.963328305
c43	2.556968686	− 8.898774607	8.040241285	0.35775723	− 1.975339157	2.990216208
c42	− 2.894585214	10.20784647	− 8.858495322	− 0.438738228	2.466137438	− 3.198465199
c41	1.28056023	− 4.719207655	3.645660877	0.243131241	− 1.472251605	1.301464732
c40	− 0.14439866	0.660321266	− 0.28544653	− 0.053115547	0.399375039	− 0.128686529
P	4–6			6–10		
κi	$K2$	$K1$	$K0$	$K2$	$K1$	$K0$
$\kappa 1$	− 0.003265611	0.037797356	− 0.033250666	− 0.000144913	0.003537295	0.059964575
$\kappa 2$	− 0.020436351	0.228427482	0.086614007	− 0.00042186	− 0.000765906	0.741252683
$\kappa 3$	− 0.028247323	0.248233515	5.391173361	0.010914711	− 0.195798405	6.645531657
$\kappa 4$	2.93997374	− 23.14126432	122.8572154	− 1.485981212	30.50830082	− 39.7057972
$c$ij	$C2$	$C1$	$C0$	$C2$	$C1$	$C0$
$c14$	− 0.040760102	0.190893147	2.013580586	0.009597319	− 0.435121011	3.956798381
$c13$	0.142201688	− 0.576849448	− 7.028498975	− 0.036979384	1.548329084	− 13.32905159
$c12$	− 0.15332886	0.345800183	9.175156901	0.051062233	− 1.978043925	15.76014222
$c11$	0.052264801	0.16145289	− 5.005988089	− 0.029089483	1.036115868	− 7.325211727
$c10$	− 0.002378417	− 0.110455601	1.068223823	0.005641115	− 0.1846925	1.224942086
$c24$	0.079797092	− 0.310373219	− 0.414998056	0.004580986	0.289056045	− 1.303793839
$c23$	− 0.236426636	0.672362246	1.505960585	− 0.001780621	− 1.137403168	3.917296544
$c22$	0.21519024	− 0.044620267	− 2.571111715	− 0.015724164	1.562949116	− 3.903609475
$c21$	− 0.055723216	− 0.524788692	2.088209175	0.015978139	− 0.841070728	1.404652596
$c20$	0.000578303	0.161103676	− 0.203205881	− 0.002274263	0.107988089	0.218180008

(continued)

Table A.7 (continued)

P	4–6			6–10		
$c$ij	$C2$	$C1$	$C0$	$C2$	$C1$	$C0$
c34	−0.247844436	2.212440393	−5.199022105	0.04636861	−0.967692998	3.290108588
c33	0.767702487	−6.864673228	17.03356977	−0.141955253	2.919302005	−8.922602992
c32	−0.809252079	7.235065311	−19.69413637	0.14372131	−2.875353251	6.661333007
c31	0.324373757	−2.86080294	9.021212572	−0.05590704	1.06201304	−0.825574646
c30	−0.035001371	0.289501774	−0.931875674	0.005443042	−0.092167763	−0.097857296
c44	0.213259707	−2.11383471	4.738259175	−0.064635018	1.125850147	−4.695639852
c43	−0.674425216	6.750228428	− 15.397135	0.193769558	−3.351933535	13.96082495
c42	0.739963608	−7.51674315	17.87382777	−0.192651718	3.260708406	−13.21672981
c41	−0.317528974	3.279010757	−8.73302127	0.073696341	−1.191072373	4.003366167
c40	0.037574547	−0.368903937	1.493387883	−0.009459122	0.156264934	0.035586732
P	10–20			20–30		
κi	$K2$	$K1$	$K0$	$K2$	$K1$	$K0$
$\kappa 1$	1.01394E−05	0.000877851	0.071053809	−3.64156E−06	0.000820106	0.077721091
$\kappa 2$	−0.000590661	0.027619376	0.474279951	7.37434E−05	−0.001613542	0.793176487
$\kappa 3$	−0.001743561	0.148155372	4.471821161	−0.001467175	0.135440616	4.615561915
$\kappa 4$	−0.065420364	5.11472346	72.1738916	−0.042483958	4.20738563	81.1460858
$c$ij	$C2$	$C1$	$C0$	$C2$	$C1$	$C0$
$c14$	0.005297004	−0.243641147	2.472031235	0.000460831	−0.060524058	0.744158733
$c13$	−0.017040291	0.796799144	−7.807661507	−0.001741585	0.208541059	−2.161982325
$c12$	0.019188977	−0.91216275	8.288656062	0.002219581	−0.244188605	1.716931614
$c11$	−0.00853956	0.408490204	−3.103947432	−0.000950699	0.099194376	0.046425012

(continued)

Table A.7 (continued)

P	10–20			20–30		
$c10$	0.001204454	−0.057915966	0.400842813	0.000105691	−0.01103283	−0.097314763
$c24$	−0.016265965	0.595438003	−2.282918347	−0.001020671	0.039793367	2.731857021
$c23$	0.05049473	−1.823487097	5.550600684	0.003046364	−0.083401006	−10.27177454
$c22$	−0.054023713	1.905988933	−3.50405273	−0.002930636	0.016877704	13.84094089
$c21$	0.022793244	−0.769051793	0.002952828	0.000865876	0.050524984	− 7.6176355
$c20$	−0.002974381	0.089761073	0.470461936	1.65209E−05	−0.023265053	1.53462368
$c$ij	$C2$	$C1$	$C0$	$C2$	$C1$	$C0$
c34	0.011967722	−0.349782154	0.551088909	0.034432204	−1.81267679	20.82318902
c33	−0.036795007	1.023484596	−0.480453541	−0.101140796	5.278545817	−59.8433625
c32	0.038272791	−0.964080047	−1.906547168	0.10447045	−5.37954988	59.92378613
c31	−0.01569717	0.325605081	2.517517992	−0.045417664	2.298152732	−25.04523761
c30	0.002225962	−0.035462855	−0.343198437	0.007080608	−0.354159452	4.088875107
c44	−0.001873681	0.008060279	0.206125135	−0.033878253	1.819215925	−23.21515909
c43	0.005754275	−0.006235992	−0.694622258	0.099761984	−5.348286015	68.54329471
c42	−0.005251633	−0.064277431	1.293120049	−0.103536768	5.530199727	−71.28236945
c41	0.001583626	0.081398342	−1.510069473	0.04534832	−2.407115612	30.75433215
c40	−0.000434679	−0.004452238	0.74031416	−0.007205345	0.384067637	−4.32181707